A Thesis Submitted for the Degree of PhD at the University of Warwick

Permanent WRAP URL:

Copyright and reuse:

warwick.ac.uk/lib-publications

Investigating the Structure and Composition of Macromolecules using Electrospray Deposition Coupled with Scanning Tunnelling Microscopy

Daniel A. Warr

A thesis submitted in partial fulfilment of the requirements for the degree of

Doctor of Philosophy in Chemistry

Department of Chemistry

University of Warwick

September 2018

Table of Contents

List of figures

List of tables

Acknowledgements

I would not have come anywhere near completing this thesis if it were not for the help of a huge number of people. Science in the 21st century is an innately team based exercise and I have been lucky to work on one of the best teams around.

Firstly, my huge thanks, gratitude and appreciation has to go to Giovanni. I have been in the group for 5 years now and I have loved every moment of it. I want to thank you for all the help and encouragement I have had along the way.

To James, Harry, Phil, and Jon. Thank you all for being such great lab mates and for making the basement lab such a fun place to work. A special thanks must go to Luis, who has put up with my sarcasm and British humour for 5 years and has dealt with it always with a smile. Thank you for when times were good and thank you for when times were bad, I couldn't have completed this work without you and I will always be thankful for the help you gave me. I also want to thank Josh and Tom who both worked with me whilst I did my PhD and were great fun to work with in the lab as well as getting some great results.

Declarations

This thesis has been submitted to the University of Warwick in partial fulfilment of the requirements for the degree of Doctor of Philosophy in Chemistry. All work which has been presented here is my own, except where has been stated explicitly otherwise. This work has been performed under the supervision of Professor Giovanni Costantini between September 2014 and April 2018. No work in this thesis has previously been submitted to any institution for a higher degree. Collaborators work has been detailed explicitly in the results sections of this thesis.

Some of the work presented in this thesis has been and will be published in the following articles:

D. A. Warr, L. M. A. Perdigão, H. Pinfold, J. Blohm, D. Stringer, A. Leventis, H. Bronstein, A. Troisi, G. Costantini, Sequencing conjugated polymers by eye. *Sci. Adv.,* **4,** eaas9543 (2018).

D. A. Warr, T. Moriarty, L. M. A. Perdigão, A. Leventis, D. Stringer, C. Jellet, I. McCulloch, H. Bronstein, G. Costantini, Predicting and visualising the alkane interdigitation angle of conjugated polymers, *in preparation.*

A. Leventis, D. A. Warr, J. Tully, L. M. A. Perdigão, G. Costantini, J. Nelson, H. Bronstein, Title to be determined, *in preparation.*

D. A. Warr, L. M. A. Perdigão, J. Blohm, H. Pinfold, A. W. Colburn, M. Barrow, G. Costantini, A high flux ion deposition instrument for nanoscale imaging studies of thermally labile molecules, *in preparation.*

Daniel A. Warr

Abstract

Macromolecules are complex, large and often thermally labile molecules with a wide range of properties and potential applications. More specifically, conjugated polymers are a subset of macromolecules with interesting electronic properties which have been utilised in organic electronic devices and show several advantages over the more commonly used inorganic alternatives. Despite the importance of these molecules to a range of fields there has been very few publications which investigate the chemical composition, and local packing of conjugated polymer assemblies with the ultimate spatial resolution of ultra-high vacuum scanning tunnelling microscopy. The reason for this is due to the incompatibility of current surface preparation techniques with conjugated polymers. In this thesis, we have used electrospray deposition in combination with scanning tunnelling microscopy in order to deposit intact conjugated polymers on atomically clean single crystal surfaces held under vacuum. Firstly, we have developed an instrument which is capable of depositing thermally labile or otherwise fragile molecules onto a sample held under high or ultra-high vacuum. Not only this, but the instrument is also capable of controlling the landing energy and mass composition of molecules within the beam. Further, by using a commercially available electrospray deposition system, we have investigated the monomer sequence, chain length and local packing of a number of conjugated polymer materials. We show that there are unexpected defects in both the monomer composition and chain length of these polymers. We also show that the local packing of a number of conjugated polymers with linear alkyl side chains can be directly visualised for the first time and directly compared to results obtained for 3D thin films of the same materials.

List of abbreviations

1D	One dimensional
2D	Two dimensional
3D	Three dimensional
A	Acceptor
BSA	Bovine serum albumin
CRM	Charge residue model
D	Donor
DAC	Digital to analogue converter
DC	Direct current
DOS	Density of states
DPP	Diketopyrrolopyrrole
ESD	Electrospray deposition
ESI	Electrospray ionisation
FT-ICR	Fourier transform ion cyclotron resonance
HOMO	Highest occupied molecular orbital
HV	High vacuum
IEM	Ion ejection model
LUMO	Lowest unoccupied molecular orbital
m/z	Mass to charge ratio
MALDI	Matrix assisted laser desorption ionisation
MBD	Molecular beam deposition
Mn	Number average molecular weight
Mw	Weight average molecular weight

ncAFM	Non-contact atomic force microscopy
NiOEP	Nickel octaethyl porphyrin
NMR	Nuclear magnetic resonance
OMBD	Organic molecular beam deposition
P3HT	Poly(3-hexylthiophene-2,5-diyl)
PCB	Printed circuit board
PEG	Poly ethylene glycol
RF	Radio frequency
RhB	Rhodamine B
SEC	Size exclusion chromatography
SEISMIC	Super electrospray ionisation source made in Coventry
STM	Scanning tunnelling microscopy
TOF	Time of flight
UHV	Ultra-high vacuum
XRD	X-ray diffraction

1 Introduction

1.1 General Introduction

The advance of modern nanoscale technologies relies on being able to create and manipulate compounds into larger functional architectures and investigate the structure and the assembly of individual functional adsorbed molecules with sub-nm resolution. This is an essential and still missing step in the development of a molecular scale foundation of many contemporary research fields. In order to achieve these goals, ultra-high resolution scanning probe microscopy techniques will need to play an important role. However, these require that complex molecular units are deposited onto well-defined substrates under perfectly controlled conditions and that analysis is completed *in-situ*. Of particular interest are organic molecules, both synthetic and natural. Modern synthetic chemistry is able to concoct almost any imaginable compound and offers a huge play-set for the functionalisation of surfaces. For this reason, adsorption of organic molecules onto substrates followed by self-assembly is a leading candidate as a tool to create such devices. To be able to utilise the power of nanotechnology the assemblies and molecules must be able to interact with the broader world, to this end a substrate is not only required but an essential step in realising potential applications. This can be seen in a range of fields: thin film coatings[1,2]; heterogeneous catalysis[3], and organic electronics[4,5] to name but a few. The almost limitless range of functions possessed by organic compounds can be harnessed through attachment to a surface, thereby functionalising the surface itself. Consequently, fundamental to this is the molecule-surface interaction and a well-defined deposition technique which can remove any ambiguity in what has landed on a surface.

If one wishes to achieve a precise, reproducible, easily controlled, and well defined deposition the most appropriate technique is molecular beam deposition (MBD). With this technique one can, with minimal effort, easily and reproducibly create a well-defined coverage of a surface whilst keeping an atomically clean environment to avoid cross contamination of the sample. Thermal sublimation in ultra-high vacuum is the strategy of choice for small and heat-resistant molecules but high molecular weight molecules with multiple functionalities are often not compatible with this process since they typically fragment at higher temperatures[6–8]. Once molecules reach a certain size the energy needed to disrupt the intermolecular forces exceeds the energy

required to break internal molecular bonds and molecular fragments are deposited rather than intact molecules. This leads to a 'glass ceiling' which limits the experimentalist's toolbox of molecules that can be chosen for studies on a clean surface. For example, the use of particularly interesting molecular subunits in polymer chains in OPV[9], or even more so the limit on chain length of polythiophenes[10] commonly used in photovoltaic devices, where the authors explicitly state that longer molecules could not be studied due to 'decomposition at high temperatures'. Placing limits on novel structures that can be investigated only serves to restrict the device performance and creates a road block in the pursuit of high performance OPVs and many other technologies that are heavily influenced by molecule-surface interactions. Another interesting example of this is the Feringa motor where only an extremely small percentage of the molecule was intact upon deposition[11]. For this specific case this poses a problem as further evolutions of this molecule cannot be studied. Any further functionalisation will inevitably increase the overall molecular weight of the molecule which will only cause further problems for thermal sublimation and a greater number of fragmented molecules. All of these examples point towards the need for a different vacuum compatible technology that is able to transfer intact molecules that are thermally fragile into the gas phase and to make a beam out of them. Fortunately, such a technique exists and was developed by the mass spectrometry community to overcome a very similar problem[12] and has been developed for the surface science community by several research groups over recent years[13–20]. The identification and investigation of the self-assembly properties of molecules too large to be sublimed is the underlying theme of this thesis. We have developed a new apparatus for the deposition of thermally labile or otherwise fragile molecules and have used existing commercial apparatus to study conjugated polymers, a subset of macromolecules which are too high in molecular weight to survive conventional thermal sublimation.

1.2 Molecular identification

Modern chemistry has a huge range of tools available to identify the synthetic product which the organic chemist can concoct. They range from nuclear magnetic resonance (NMR)[21] of both protons and carbon nuclei, to mass-spectrometry (MS)[22], gas chromatography (GC)[23], infrared spectroscopy (IR)[24], X-ray crystallography[25] and many more which are too numerous to list fully here. For the most part a combination of these techniques can identify the vast majority of synthesised products. However, a

fundamental commonality between all of these techniques is the inherent averaging of the technique. That is, in all of these methods an ensemble of molecules is used and analysed, the results of which are typically an averaging of the properties of all of the molecules present. In the case of a completely pure sample this is not problematic and even with mixtures of products the structures can often be deduced from a deconvolution of the information given. However, for the ever more complex synthesis of larger and more varied molecules the ambiguity which may arise from averaging is a problem. For example, if a conjugated polymer were to incorporate a mistake in the ordering of monomer units it would be not be easily detected by any of the techniques listed above and as such investigations have attempted to find alternative ways of identifying mistakes in the sequence through indirect means[26]. To this end, the development of alternative means of investigating the chemical structure of molecules has been pursued. This is not a new idea. Indeed, Richard Feynman in his talk 'There's plenty of room at the bottom'[27] in 1960 envisaged a type of chemical identification where 'you just look at the thing! You will see the order of bases in the chain; you will see the structure of the microsome'. Feynman, envisaged this type of analysis to be completed by electron microscopes and although there have been significant achievements in this direction[28] it is through scanning probe microscopy (SPM) that this vision has been most directly achieved.

A
STM
3Å
0Å 1.54Å

B
AFM
−1.2Hz 1.9Hz

C
$C_{26}H_{14}$
Reactant 1

D
5Å

E
-2Hz
5Å
-7Hz
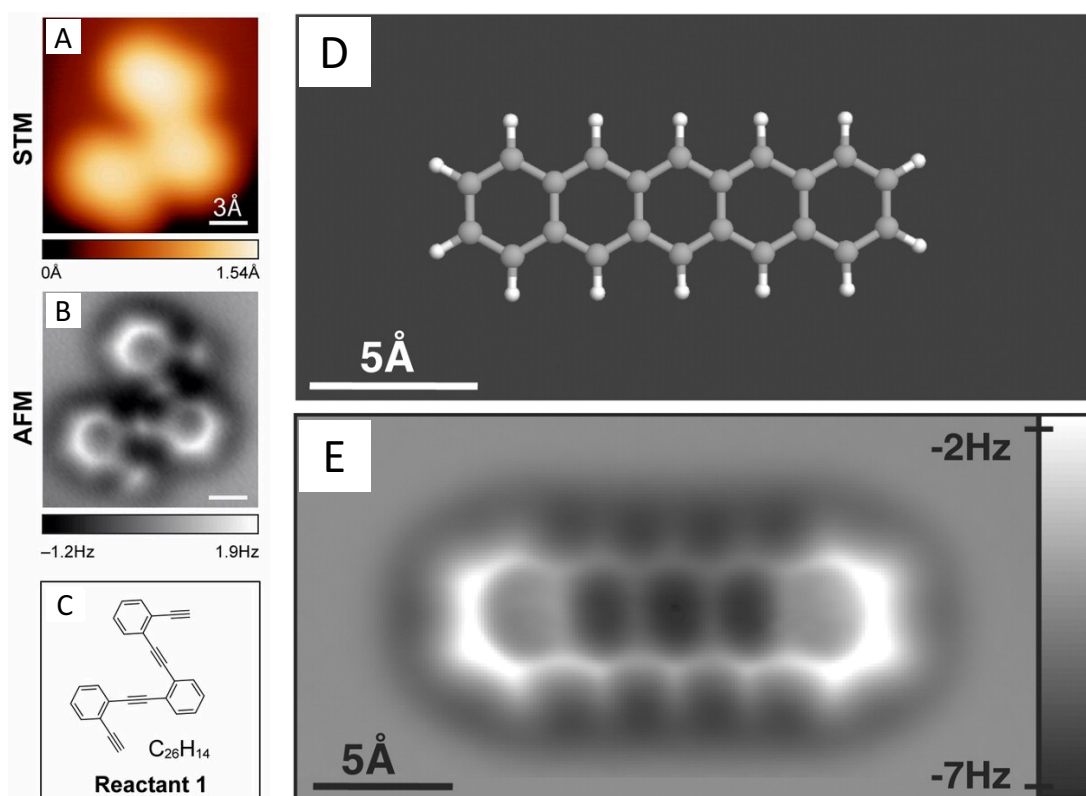
Figure 1.1 Overview of examples of SPM being used to identify the chemical structure of a molecule. Panels A, B and C are adapted from work by Crommie and co-workers[29] and panels D and E are adapted from work by Gross and co-workers[30].

Many researchers are using SPM as a tool to not only study the self-assembly of molecules on surfaces but to also probe the specific chemical structure of these molecules. A prime example of this is work by Gross and co-workers[30–33], Crommie and co-workers[29,34–37], and others[38–41] (some examples can be seen in Figure 1.1). Even if molecular identification was not the main aim of these works, in all of these investigations SPM techniques (STM, non-contact atomic force microscopy (ncAFM), and conventional AFM) are used to image the chemical structure of a number of species. In certain instances[33], the molecules studied were unidentifiable by conventional chemical techniques for a range of reasons, yet through high resolution imaging techniques the structures can be identified through simply looking at the molecules which are present. A true realisation of Richard Feynman's vision. So far, this work has been limited to the types of molecules which are compatible with current surface preparation techniques. That is, any molecule which is too large to thermally sublime cannot be prepared in the ultra-high vacuum environments required for the high resolution imaging to occur. In some instances, this is avoided by imaging the molecule of interest at ambient conditions, however this can offer suffer from sample

contamination and the difficulties associated with working at the solid liquid interface. Further, in general, the resolution of images obtained at ambient conditions are often lower in resolution than those obtained under ideal UHV and low temperature conditions. As stated previously, an area which may benefit from this type of research could is polymers, and more specifically conjugated polymers. For this to happen the combination of a surface preparation technique which is compatible with vacuum and also large thermally labile molecules is needed.

1.3 Depositing molecules on a surface in ultra-high vacuum

Using a combination of scanning probe microscopy and surfaces prepared in UHV as a way to probe molecular structure can be a useful tool in addition to conventional chemistry techniques however, in order for the technique to be expanded to a wider range of molecules new surface preparation techniques need to be explored. A key advantage of using UHV environments to study molecules is the lack of contaminant molecules. This makes it possible to study the interaction between a molecule and a surface or, through decoupling[42], simply the molecule itself. This lends itself well to complementary theoretical studies where the clean environment can be readily modelled. It is therefore important that the surface is prepared in a clean manner, maintaining the lack of contaminants.

There are a number of surface science preparation techniques which have been well established over a number of years[6]. The most commonly used is molecular beam deposition (MBD), or in the case of organic molecules OMBD[43]. The typical apparatus is rather simple and consists of a crucible and a heating element (Figure 1.2). The sample of interest is placed inside the crucible and heated using the heating element. Under the UHV conditions, the molecule will sublime and form a molecular beam, when directed towards a surface the gaseous molecules condense and form coverages from sub-monolayer up to thin films dependent on a number of factors (time, temperature, chamber geometry). MBD has been used countless times for preparation of molecules or metals on surfaces and produced reproducible controllable coverages. The technique is compatible with a wide range of molecules but has some severe limitations, especially when considering the field of macromolecules. As stated previously, MBD is incompatible with: larger molecular weight, thermally labile, reactive or otherwise fragile molecules. The inherent thermal energy input into a

molecule to transform it from a solid powder or crystal into a gaseous beam is often high enough to overcome an energy barrier for an undesirable side pathway.
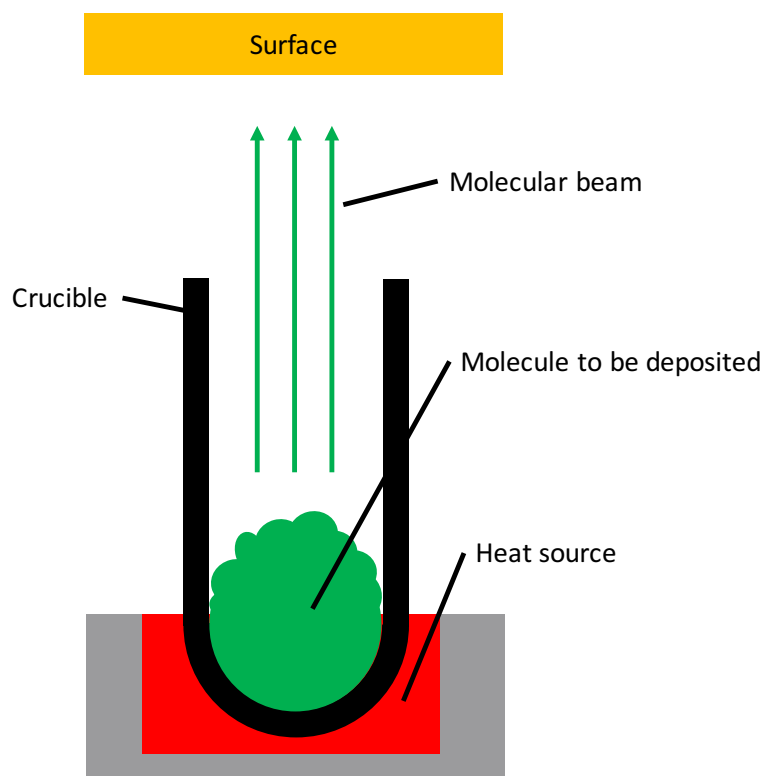
Figure 1.2 Schematic showing the OMBD experimental setup.

Several alternatives exist which do not have the same thermal sublimation limit. One of the simplest of these is rapid heating deposition[44,45]. In this experiment the molecule to be deposited is placed on a filament, or other heat conductive material. The filament is then placed within close proximity of the surface and a high current is applied (2-10 A) for a fraction of a second (on the order of hundreds of milliseconds) (Figure 1.3). In this way a very high temperature is reached in a short period of time. The theory behind this method is that as the activation energies of fragmentation and sublimation are likely to be different and thus by reaching the higher temperature required to sublime the molecules in a shorter time period, at least some molecules will arrive at the surface intact. Although this technique is useful in depositing some molecular species intact to a surface there are numerous pitfalls. Firstly, only some of the molecules will arrive intact to the surface and it can be extremely difficult to tell whether molecules which have arrived at the surface are intact or not, especially in the instance where the absolute structure of the original species is unknown. Secondly, due to the rapid nature of the deposition, only low coverages can be achieved. This

may be suitable for imaging individual molecules but can be limiting if one wishes to study the self-assembly of the molecules.
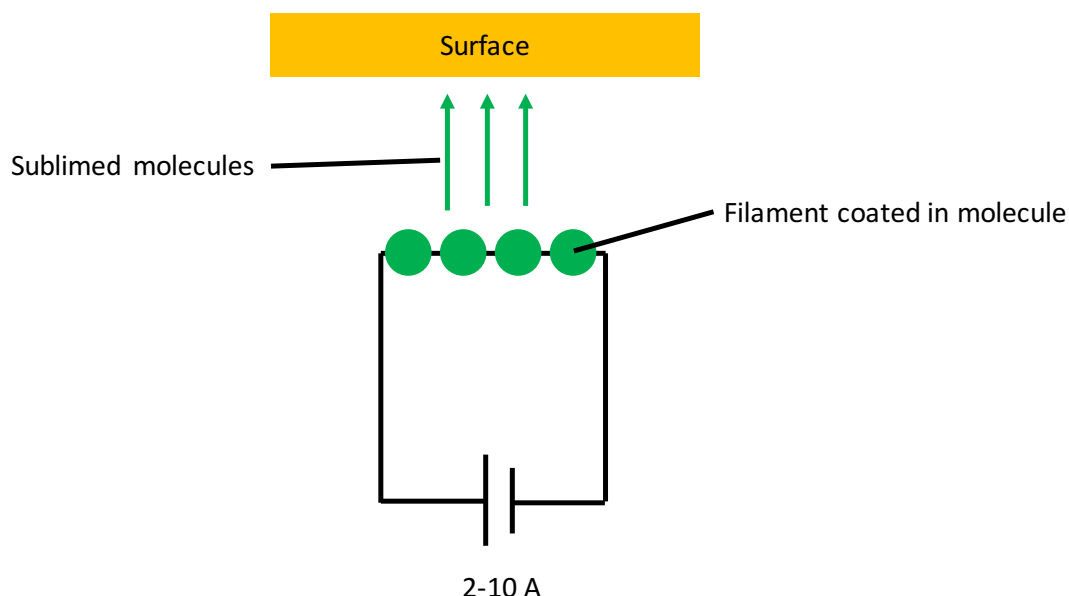
Figure 1.3 Schematic showing the rapid heating experimental setup.

Another alternative is the pulse injection or pulse valve technique which has been used to study a range of molecules including DNA[46] and organic polymers[47,48]. In this method, molecules are dissolved in a suitable solvent and placed inside a container attached to the vacuum chamber where the surface is held under UHV. An orifice (approximately 0.05 mm diameter) with a fast action valve separates the solution containing vessel from the vacuum chamber. The molecule is deposited by opening the valve and releasing the solution for a few milliseconds, exposing the surface to the solution (Figure 1.4). This technique, unlike both thermal sublimation and rapid heating, does not involve any application of heat to the sample and therefore avoids the risk of thermal fragmentation to the molecule. However, surface coverage can again be very difficult and is not easily controlled through changing concentration or pulse times. Further, contamination of the surface by solvent molecules is an obvious issue and is an almost unavoidable consequence of the methodology. Despite this, numerous research articles have demonstrated the ability of this technique to deliver intact macromolecules to a surface.
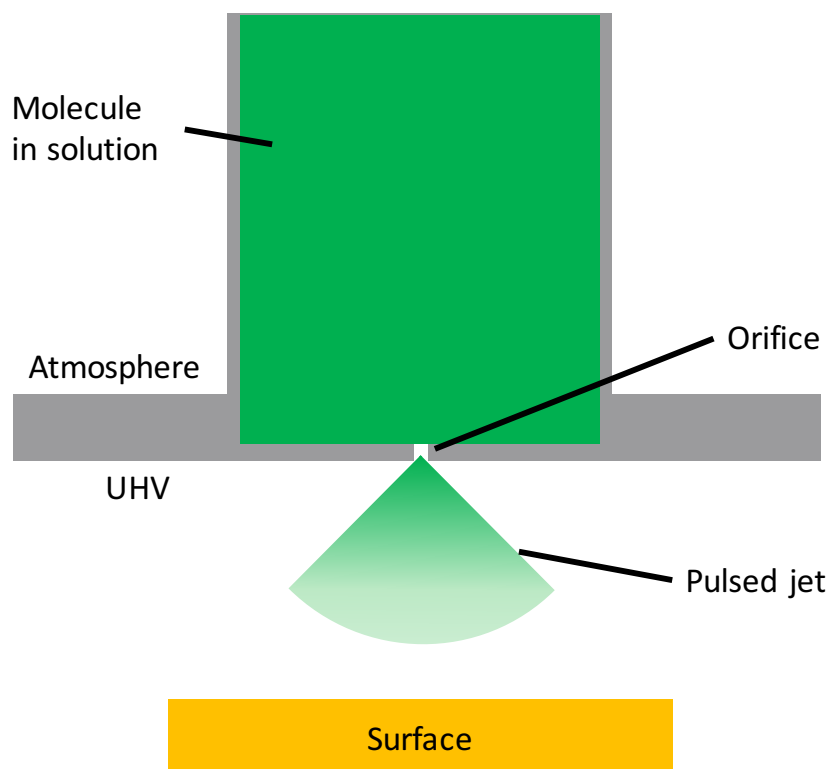
Figure 1.4 Schematic showing the pulsed jet experimental setup.

The final alternative to thermal sublimation which shall be discussed here is electrospray deposition[13–16]. Electrospray deposition is the combination of an electrospray ionisation source and a differentially pumped system which bridges the pressure differential between where a sample is held and the electrospray is formed. There are a few existing designs for this type of system[13–16] which all share the common features mentioned above but differ in their specific designs. The simplest electrospray deposition system is the commercially available Molecular Spray system[49], where an electrospray ionisation source is coupled to several differentially pumped chambers which are in turn separated from the preparation chamber by a gate valve. The more sophisticated systems from Rauschenbach and co-workers[14], Laskin and co-workers[15] and Berndt and co-workers[16] incorporate ion guiding elements in order to control and shape the beam as well as incorporating the capability of obtaining mass spectra of molecules in the ion beam. An example of the more sophisticated type of setup can be seen in Figure 1.5, this system is from Berndt and co-workers[16] and incorporates many of the ion guiding elements mentioned (which are discussed in further detail in section 2.2)

.
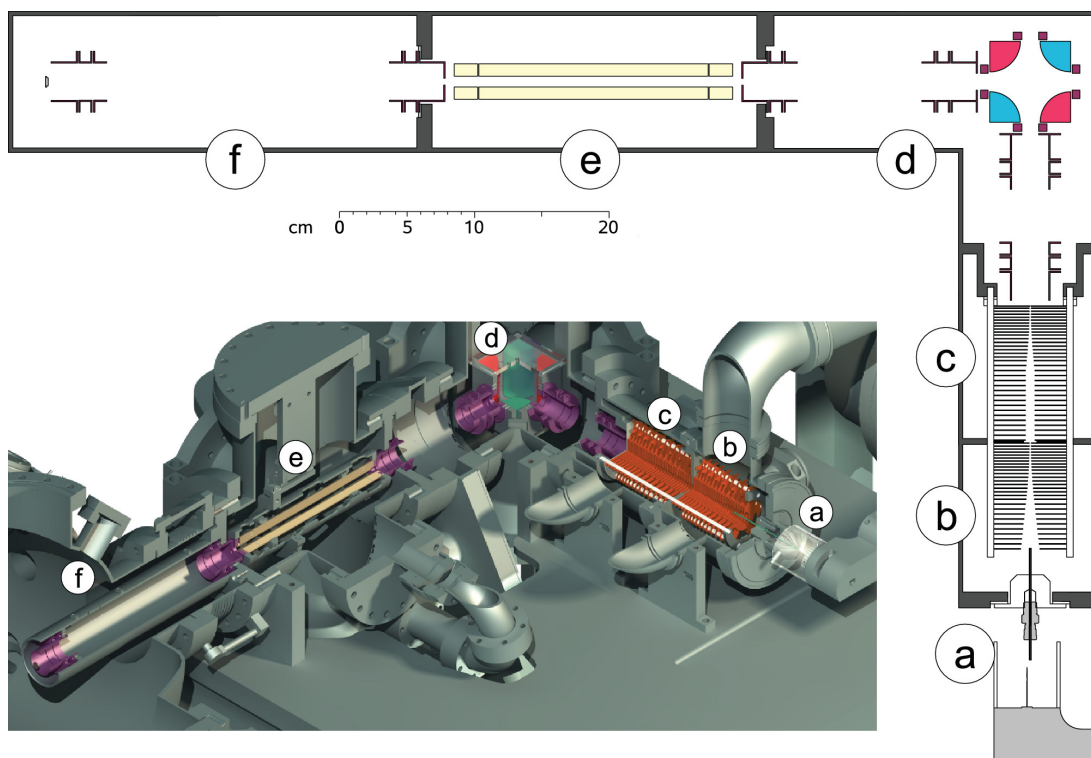
Figure 1.5 Overview of the electrospray deposition system developed by Berndt and co-workers[16].The elements contained within this instrument are as follows: (a) ambient pressure electrospray ion source; [(b) and (c)] two stage radio frequency ion funnel for high ion transmission in the viscous flow regime ($p1 \approx 0.8$ mbar , $p2 \approx 3.5 \times 10-2$ mbar); (d) electrostatic quadrupole deflector for separation of charged particles and energy filtering ($p3 \approx 1 \times 10-5$ mbar); (e) quadrupole mass filter ($p3 \approx 1 \times 10-7$ mbar); (f) ion deposition ($p5 \approx 1 \times 10-9$ mbar).

All of these systems have been used to successfully deposit and image a range of macromolecules from porphyrin nanorings[17] to molecular magents[50], proteins[51], peptides[52] and more[16,53,54]. One advantage of using electrospray deposition is that any molecule that is soluble and can be formed into an electrospray is compatible, meaning a wide variety of molecules can be studied (as evidenced by the references given). Further, as there is no heat applied to the solution the risk of fragmentation is minimal meaning reactive and thermally labile molecules can be studied. On top of this, by including ion optics one is able to control and direct the beam in order to deposit the molecule of interest with either a higher or lower landing energy than is available to other deposition techniques which opens up the possibility of a range of experiments[55,56]. Finally, as the electrospray ionisation process creates charged particles, it affords the opportunity to analyse the beam composition before deposition in order to verify whether the molecule is arriving in the state which is intended. The technique obviously comes with its flaws which include the difficulty in controlling

molecular coverage, the incompatibility of some molecules to the electrospray process and the somewhat cumbersome equipment (in the case of the more sophisticated systems). However, despite this the technique has shown remarkable success as demonstrated by the examples given.

1.4 Overview of this thesis

In this thesis the combination of electrospray deposition, and STM are explored for the purpose of gaining an insigt into the complex self-assembly of macromolecules and specifically conjuagted polymers. We also believe futher insights into their structure and self-assembly on surfaces will aid in the advance of their use in key tecnhologies. We have chosen to use the Molecular Spray system for this purpose due to its ease of use and compatibility with the widest array of molecular species. Particular interest was given to conjugated polymers due to the current lack of published data in this field and the numerous oppurtunities for study opened up by the combination of techniques demonstrated herein. We have also developed a new instrument which combines electrospray deposition and STM with the capability of obtaining mass spectra of the ion beam and controlling the landing energy of molecular species. This new instrument gives our lab the capability to proceed with a number of experiments that are not currently possibe with existing commerical apparatus.

Chapter 3 describes the design of SEISMIC, a complex instrument capable of depositing thermally labile molecules onto a surface held at UHV. The design principle of high transmission, adaptability and compactness are demonstrated throughout.

Chapter 4 shows the resulting performance of the homebuilt ion optics and components which comprise SEISMIC. The first results for the instrument are shown and some first analysis is shown. A number of molecular test systems are studied and promising results are given.

Chapter 5 is the first example in this thesis of the use of the Molecular Spray system being used in combination with an STM in order to study a conjugated polymer system. A typical diketopyrrolopyrrole polymer is deposited and the self-assembly is studied. The polymer is sequenced for the first time by direct visualisation of the backbone at sub-monomeric resolution.

Chapter 6 gives an investigation into the synthetic growth of conjugated polymer chains by studying the oligomers and corresponding polymer. By comparing the different stages of the polymer synthesis insights can be gained into the growth mechanism and the occurrence of side-reactions and synthetic by products.

Chapter 7 demonstrates an investigation into the local packing of conjugated polymer side chains and investigates the relationship between the monomer composition and angle of the interdigitated alkyl side chains.

Finally, chapter 8 provides a summary and outlook for the work in this thesis.

2 Background and theory

2.1 Electrospray ionisation (ESI)

2.1.1 Introduction

Electrospray ionisation is a technique used to generate charged intact gas phase molecules by means of applying a high voltage to the molecule of interest which has been dissolved in a suitable solvent. Electrospray ionisation has been known to exist since Lord Rayleigh's theoretical calculation of the Rayleigh limit[57], the maximum charge a liquid droplet can hold before surface tension can no longer hold the droplet together and jet expulsions result, this is the fundamental process involved in electrospray ionisation. Experimentally, the technique has been used since as early as 1914 and was developed by Zeleny over several years[58,59]. The use of electrospray ionisation as a technique to produce a beam of macroions was first demonstrated by Dole and co-workers[60]. The technique as we know it today, as used for mass spectrometry was developed by John Fenn in the 1980s[61,62] for which he was awarded the Nobel Prize in Chemistry in 2002 (shared with Koichi Tanaka and Kurt Wütricht)[63]. In the context of this thesis electrospray ionisation is being used to generate intact gas phase ions which represent an appropriate sampling of the original dissolved compound. We are utilising the soft ionisation technique in order to overcome the traditional limitations of vacuum surface preparation.

2.1.2 Basic principle of operation

A schematic showing the general setup of an electrospray ionisation source is shown in Figure 2.1. It depicts the main components of an electrospray ionisation source: solution injection; high voltage; emitter needle; and entrance capillary. In this figure we also see the steps through which the gas phase ions are formed.
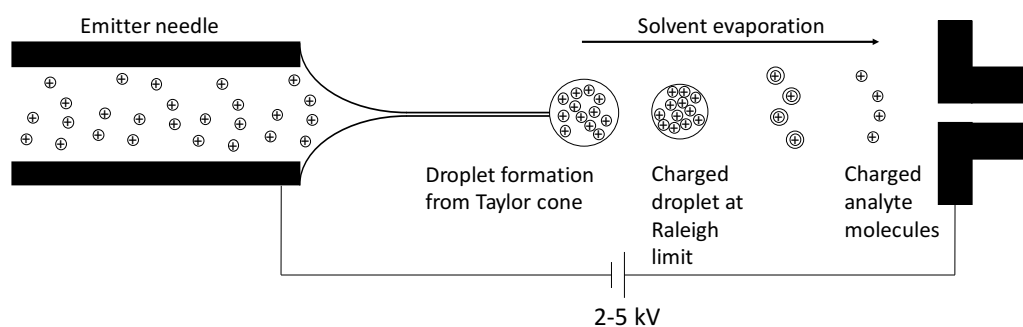
Figure 2.1 Schematic showing the electrospray ionisation process.

There are 3 main stages to the production of gas phase ions by electrospray ionisation: generation of charged droplets at the electrospray emitter; desolvation of the initially formed droplets to produce small highly charged droplets; and the production of gas phase ions from the highly charged droplets.

Stage 1, the generation of charged droplets at the electrospray emitter, is conducted as follows. The analyte of interest is dissolved in a suitable solvent (typically a polar, volatile solvent) and is placed into a syringe. The solution is pumped through a metal emitter with a diameter on the order of 0.1 mm and a high voltage (2-5 kV) is applied between the solution and the capillary (which is the reference ground electrode). The emitter is made of an electrically conducting material from which the aerosol is emitted. There are 2 main forces acting on the jet as it emerges from the emitter. Surface tension of the liquid acting to keep the droplet intact; and electrostatic repulsion between the like charges in the solution acting to pull the liquid apart. If one balances these forces the formation of a Taylor cone[64] is observed. At the tip of the Taylor cone where the field strength is highest droplets are released containing the charged particles. It was shown by Smith[65] that the droplets produced are close to the Rayleigh charge limit. The second stage, reduction in droplet size is due purely to neutral solvent evaporation. The charge of the droplet remains the same while the charge density of the droplet increases. The solvent evaporation is often aided through the use of heated neutral curtain gases.

There are currently 2 main hypotheses which attempt to describe the mechanism by which charged particles are generated from the droplets of solvent and analyte which are depicted in Figure 2.2. Dole and co-workers[60] proposed the charged residue model (CRM) and a more robust mechanism was proposed by Röllgen[66,67]. The CRM model states that droplets which have been produced undergo successive evaporation and fission cycles. That is, as the volatile solvent evaporates the charge density of the droplet increases until fission occurs resulting in smaller droplets but with a lower charge density. This cycle continues until droplets with either 1 or fewer charged molecules remain. The remaining solvent evaporates leaving ionised gas phase molecules. The ion ejection model (IEM) was proposed by Iribarne and Thomson[68,69] in 1976. This hypothesis states that as droplets reduce in size through evaporation of solvent, direct ejection of ions becomes more likely than coulomb fission. There is

some evidence which suggests that the CRM is more applicable to smaller molecules and the IEM to larger molecules[70–72].
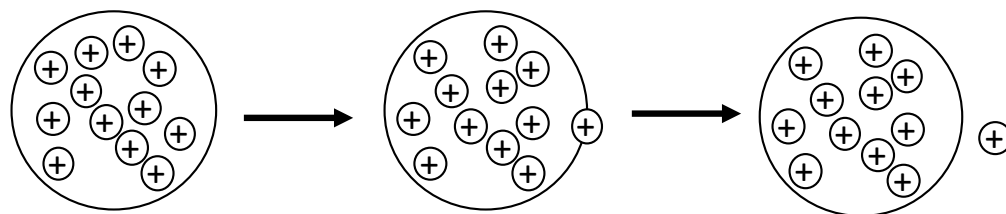
(A) Ion evaporation model (IEM)
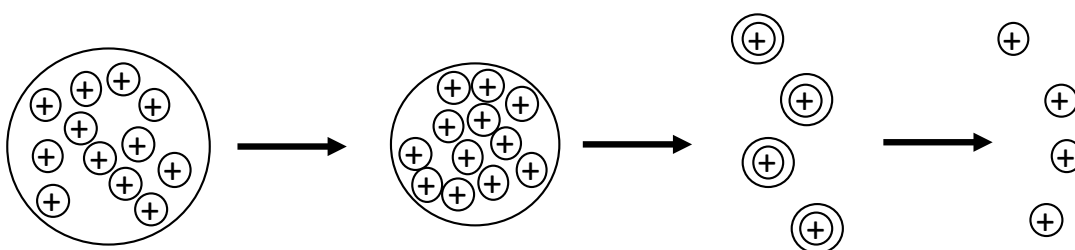
(B) Charge residue model (CRM)

Figure 2.2 Schematic of the two main models of ion formation from an electrospray droplet.

In electrospray ionisation the ions which are observed are composed of the molecular species, M, with the addition of a proton, H^+, or some other cation (such as Na^+) to give the species $[M+H]^+$ or $[M+Na]^+$ when completed in the positive mode (which is the only mode used in this thesis). In the case of the negative mode a hydrogen nucleus is removed from the molecular species resulting in a negatively charged ion, $[M-H]^-$. For larger macromolecules which can sustain multiple charges on the same molecule, multiple charge states exist whereby either additional protons or cations are added or removed from the molecule.

2.2 Ion optics and ion guides

2.2.1 Introduction

Having created a beam of ions through an ionisation process (such as ESI) if one wishes to control and manipulate their path through an instrument, ion optics can be used. Ion optics[73,74] are a range of devices which can be used to shape, focus, collimate, and direct a beam based on the ions interactions with the electric fields of the ion

optics. Devices range from simple DC voltage electrodes through to radio-frequency (RF) devices which can act to transport ion beams efficiently through an instrument. In this section we will look at the two main ion optic elements which have been used in this thesis, electrostatic lenses and multipole ion guides.

2.2.2 Electrostatic lenses

Electrostatic lenses are devices which are used to focus an ion beam. They typically consist of a specific geometry of ring electrodes to which static DC voltages are applied. In this work we have focussed on einzel lenses and these shall be the only such type discussed here. Einzel lenses consist of three cylindrical electrodes placed in a row[75,76]. As a consequence of their geometry and the voltage which has been applied, an inhomogeneous electric field is created inside the cylinder region (as seen in Figure 2.3) which is used to focus ions to a focal point which is determined by the voltage applied to the electrostatic lenses. As can be seen in Figure 2.3, typically the first and last electrode of the three electrode geometry are held at 0 V (relative to the rest of the system).
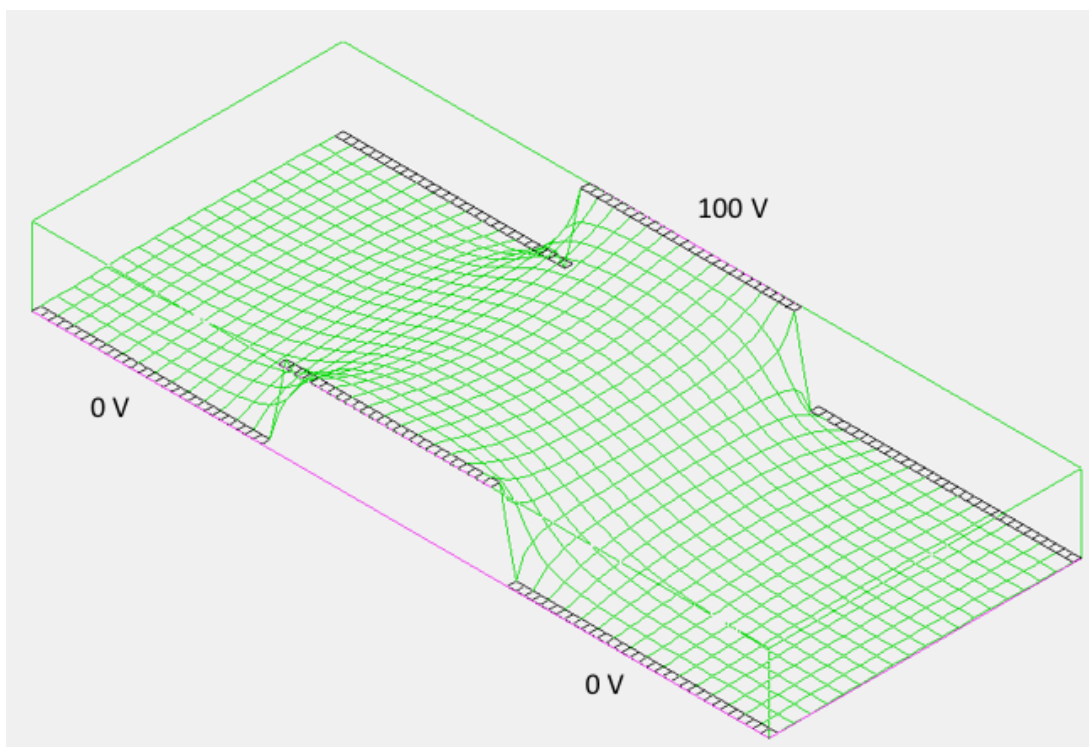
Figure 2.3 Electrostatic potential energy landscape for a central cross section of an einzel lens.

As ions enter the device their path is influenced by the electric field. The critical section of the electrostatic lens are the transitions from the first lens to the second and

17

the transition from the second to the third. As ions leave the first electrode and pass into the second they reach an electric field where they are slowed axially and pushed outwards radially. Once ions enter the second electrode the axial deceleration decreases and they are pushed inwards radially. As ions leave the second electrode they are accelerated axially and continue to move inward radially due to their momentum. Finally, as ions transition from the second to the third electrode the axial acceleration increases and a weak and short outward radial force is applied. As ions are moving slower through the second electrode (where inward radially forces are applied) the overall effect on the ion beam is that it is compressed radially (this process is depicted in Figure 2.4).
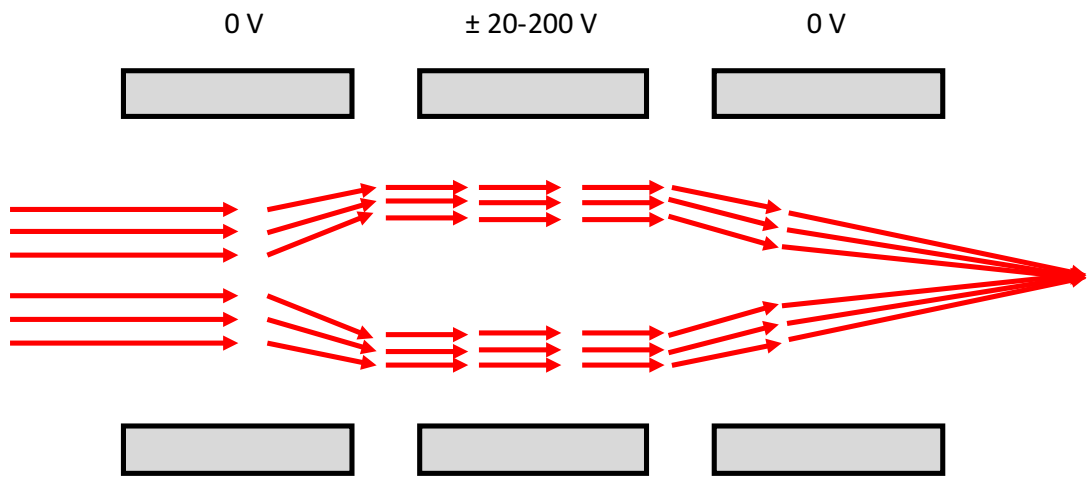
Figure 2.4 Depiction of the path of ions passing through an electrostatic lens consisting of three ring electrodes.

The strength of focussing is determined by the voltage applied to the central electrode as this determines the gradient of the electric field inside the second electrode where inward radial forces are applied. This can be seen in several SIMION simulations for a bunch of ions (m/z = 100, kinetic energy = 200 eV) in Figure 2.5 where we see that an increasing voltage on the central electrode results in a focal point which is closer to the einzel lens assembly.
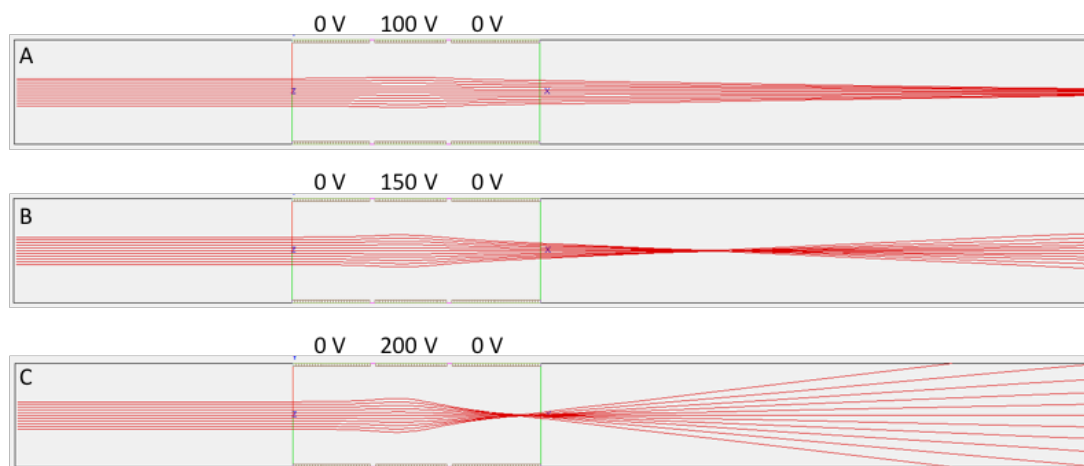
Figure 2.5 SIMION simulations for an einzel lens showing the lens voltage effect on focal length. Ions are simulated from a parallel source with a single axial kinetic energy value of 50 eV.

Since electrostatic lenses rely on the balance between an ions axial and radial kinetic energy and the voltage applied to the lens they do not work well for ion beams where there is a large spread in kinetic energy. It is therefore most useful to use electrostatic lenses in areas of the instrument where the spread of kinetic energies is minimal or where focussing of a beam is unavoidable. For ion beams with a wider range of kinetic energies different transport optics can be used, which will be explored in the next section.

2.2.3 *Multipole ion guides*

Mulitpole ion guides[77] consist of an even number of cylindrical rods aligned parallel and placed in a circular geometry, an example of which (the hexapole) can be seen in Figure 2.6. Multipole ion guides are used to transport ions of a wide mass range from one side of an instrument to another and can operate in a wide range of vacuum regimes.

$$U_+ = V_{DC} + V_{RF}\sin(\omega t)$$

$$U_- = V_{DC} - V_{RF}\sin(\omega t)$$
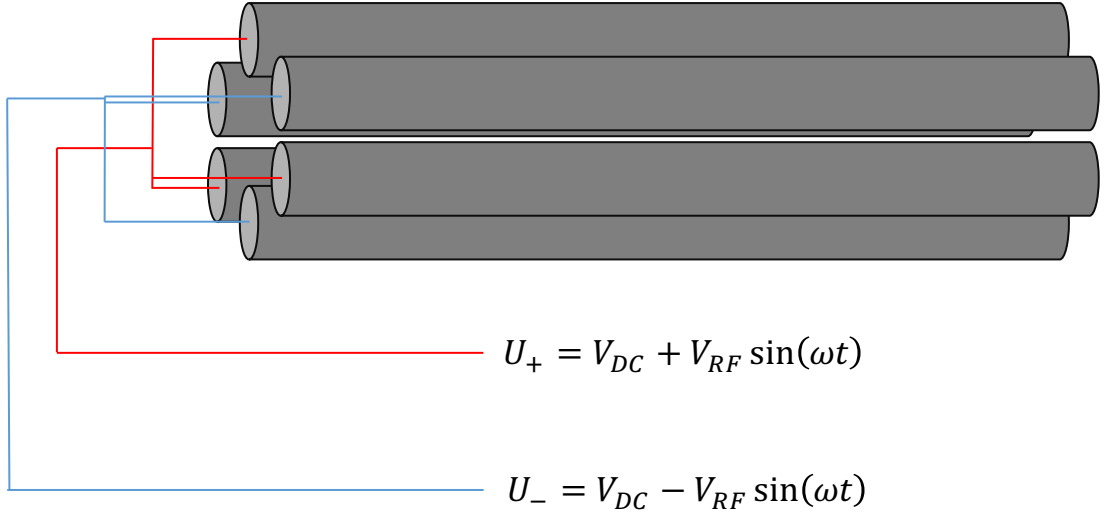
Figure 2.6 Schematic showing the arrangement of rods in a multipole (specifically a hexapole in this case) and the formula for the application of voltages to each of the rods.

The rods have both a DC and RF potential applied to them where adjacent rods have an out of phase RF potential applied. The formula for the application of the potential to the rods in a multipole is as follows

$$U_+ = V_{DC} + V_{RF}\sin(\omega t)$$

Equation 2.1

$$U_- = V_{DC} - V_{RF}\sin(\omega t)$$

Equation 2.2

Where U_+ and U_- are the overall voltages applied to the adjacent rods which is composed of the DC voltage, V_{DC}, and the RF voltage, V_{RF}. The RF voltages varies with time, t, at a frequency ω. For the transport of a wide range of masses a single V_{DC} and V_{RF} value combination is chosen. Mass selection can be achieved using a particular type of multipole ion guide as will be discussed in section 2.3.2.

If the electric field were static no transport would occur as ions would simply be repelled by like charged rods and attracted to those of the opposite charge. The device works as these voltages oscillate with the RF potential creating an oscillation in the ions movement within the multipole device. The time averaged motion of the ions can be approximated using an effective static potential (U_{eff})[77] which is related to the

distance from the centre of the multipole (r) and the number of poles in the multipole device (N) through the following relationship

$$U_{eff} \propto r^{(2N-2)}$$

Equation 2.3

Modelling this potential for a number of different multipoles gives the potential landscapes seen in Figure 2.7 (r_0 is the radial distance from the centre of the device to the inner edge of a rod). We note that for higher order multipoles (those with more rods) the potential is much flatter in the centre and rises more steeply at the edges. This wide flat region which increases with rod number is an important consideration in our designs. In this region where ions are not directly under the influence of the electric field ions are free to move unperturbed and will fill this region of the multipole when being transported. This corresponds to a larger beam diameter upon exiting the device which can be problematic for further focussing through small apertures (such as those at differentially pumped limits). However, as the higher order multipoles give better transmission[77] through the device itself a balance must be chosen between these two factors.
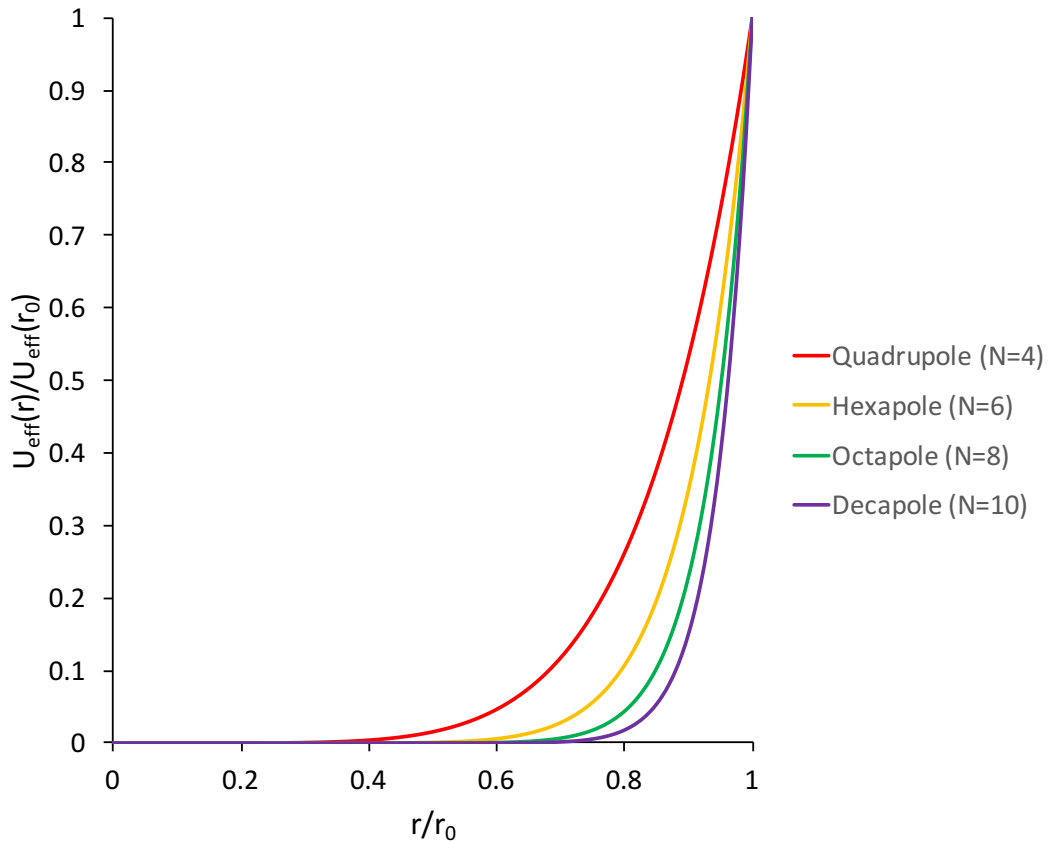
Figure 2.7 Graph showing the dependency of the effective potential on the distance from the centre of the multipole for multipoles of different number of rods (N) using Equation 2.3.

Multipole ion guides are particularly useful at transporting ions from one section of an instrument to another with minimal losses due to the well confined potential which extends for the entire length of the device.

2.2.4   SIMION simulations of ion optics

SIMION is a software package which can be used to predict the paths of ions under the influence of electric fields[78]. SIMION has been used in several instances in this thesis in order to determine the best geometry or size of a component and the expected values of voltages. The theory which governs the predictions SIMION makes are based on the interactions between the charged particles and the electric fields generated by the components built within the software.

The force on a charged particle in an electric field is

$$\vec{F} = q\vec{E}$$

Equation 2.4

Where $\vec{F}$ is the force applied to the particle with charge q in an electric field $\vec{E}$. From this equation we can calculate the force on the particle knowing the electric field strength. In regions where $\nabla \times \vec{E} = 0$, the electric field can be expressed as a gradient of a scalar field, which is defined to be the electric potential *V(x,y,z)*.

$$\vec{E} = -\nabla V$$

Equation 2.5

Where ∇ is the differential operator, the sum of the derivative in *x*, *y* and *z* spatial co-ordinates of the potential V from which the electric field originates. In regions without charge

$$\nabla \vec{E} = 0 \iff \nabla \cdot \nabla V = \nabla^2 V = \frac{d^2V}{dx^2} + \frac{dV}{dy^2} + \frac{dV}{dz^2} = 0$$

Equation 2.6

which can be used to generate a value for *V* in free space with known boundary conditions. In SIMION the system is split into a series of smaller parts. For each of

these parts (corresponding to device electrodes) the potential is fixed and at the boundary the zero Neuman boundary condition is applied. All other potentials are created by averaging the potential of the surrounding potentials. This calculation is completed iteratively until it converges. Having calculated the potential at every point in the assembly we can generate an electric field and in turn the force on an ion at any given time. Finally, using

$$\vec{F} = m\vec{a} = m\frac{d\vec{v}}{dt} = m\frac{d^2\vec{s}}{dt^2}$$

Equation 2.7

Where m is the mass of the ion, a is the acceleration, *v* the velocity, *s* the position and *dt* the time interval, SIMION can predict the position and path of each ion at a specified time interval. From these formulae it is possible to build potential arrays within SIMION, from which the path of an ion can be predicted. Scripts can be written in order to fly groups of ions with differing m/z, kinetic energy, kinetic energy spread and starting positions.

2.3 Mass Spectrometry

2.3.1 Introduction

Mass spectrometry is the separation and detection of molecular species based on their mass to charge ratio (m/z). Mass spectrometry instruments typically consist of three main components: an ionisation source; a mass filtering device; and a detection mechanism. The ionisation source has been described in the previous section and here we will focus on the mass filtering device. There are many different types of mass filtering device which include: sector instruments; time of flight (TOF); ion traps; Fourier transform ion cyclotron resonance (FT-ICR); and quadrupole mass filters. The mechanisms by which these filtering devices work are diverse and complex. We will focus only on the type used in the instrumentation in this thesis, the quadrupole mass filter.

2.3.2 Basic principle of operation

The quadrupole mass filter is a type of multipole ion guide as described in section 2.2.3. The radio-frequency (RF) device consists of four cylindrical rods set in the geometry shown in Figure 2.8. The mass filtering is achieved by utilising radio-frequency (RF) voltages along with DC voltages to create an electric field where ions

of a particular m/z have a stable trajectory and are allowed to pass through, whereas those of a different m/z have an unstable trajectory and are not allowed to pass (this can be seen schematically in Figure 2.8). Its operation differs from that of a multipole ion guide as the voltages are set such that only a single m/z value has a stable trajectory within the device. A basic overview of the operation is given here and a more complete overview of the principles which govern the mass selection can be found in the references given[77,79,80].

——————→ Path of stable ion (transmitted)

——————→ Path of unstable ion (filtered out)
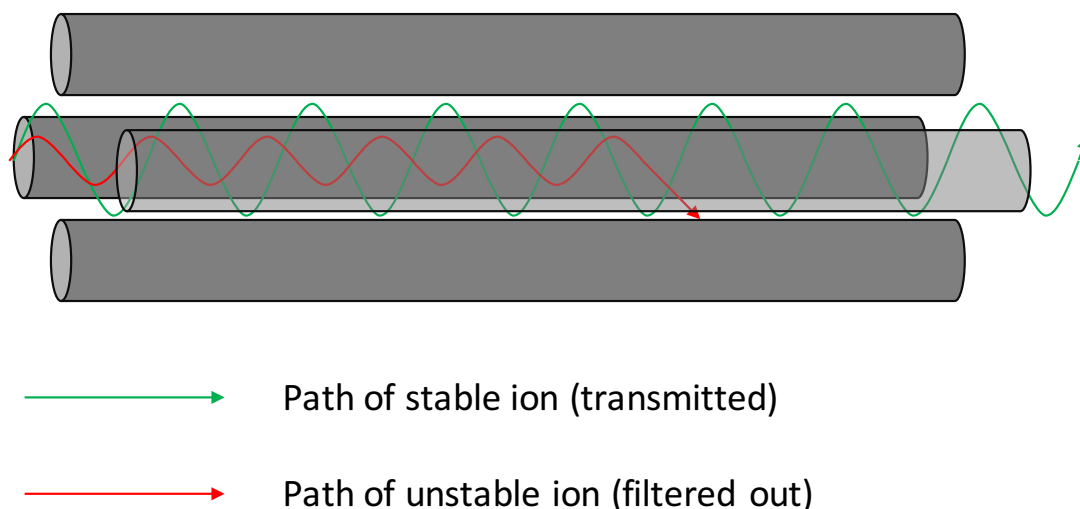
Figure 2.8 Schematic of a quadrupole mass-filter showing the path of stable and non-stable ions.

In a typical experiment used to collect a mass spectrum of a sample, a beam of ions (of varying m/z values) is directed into the mass filtering quadrupole. As the beam travels through the quadrupole the ions' path is influenced by the electric field generated by the quadrupole rods. Both an RF voltage and a DC voltage are applied to each of the rods, where opposite pairs of rods have out of phase RF voltages. The path of each ion can either be stable (the ion travels through the length of the quadrupole) or unstable (the ion is ejected before the end of the quadrupole) which depends on the m/z value and the specific value of the RF voltage and DC voltage applied. The range of RF and DC voltages for which each m/z value is stable can be seen in stability diagrams[77,80] which can be calculated through Mathieu equations[81] and verified with ion simulations. The ion must be stable along both the x and y axis of the mass spectrometer (with the z axis being the one along which ions travel). It is the overlap in these stability regions which defines the voltages which can be applied to the rods in order to transmit ions of a particular m/z value. An example of these

stability overlap regions is given in Figure 2.9. A mass scan is conducted by changing the RF voltage and DC voltage along a pre-calculated path where at each point along the path only a single m/z value is stable within the quadrupole (again this can be seen in Figure 2.9), which is represented by where the scan line passes within the stability region. The difference in operation between a multipole ion guide used for transport and one used for mass filtering is in the specific application of DC voltages to the rods.
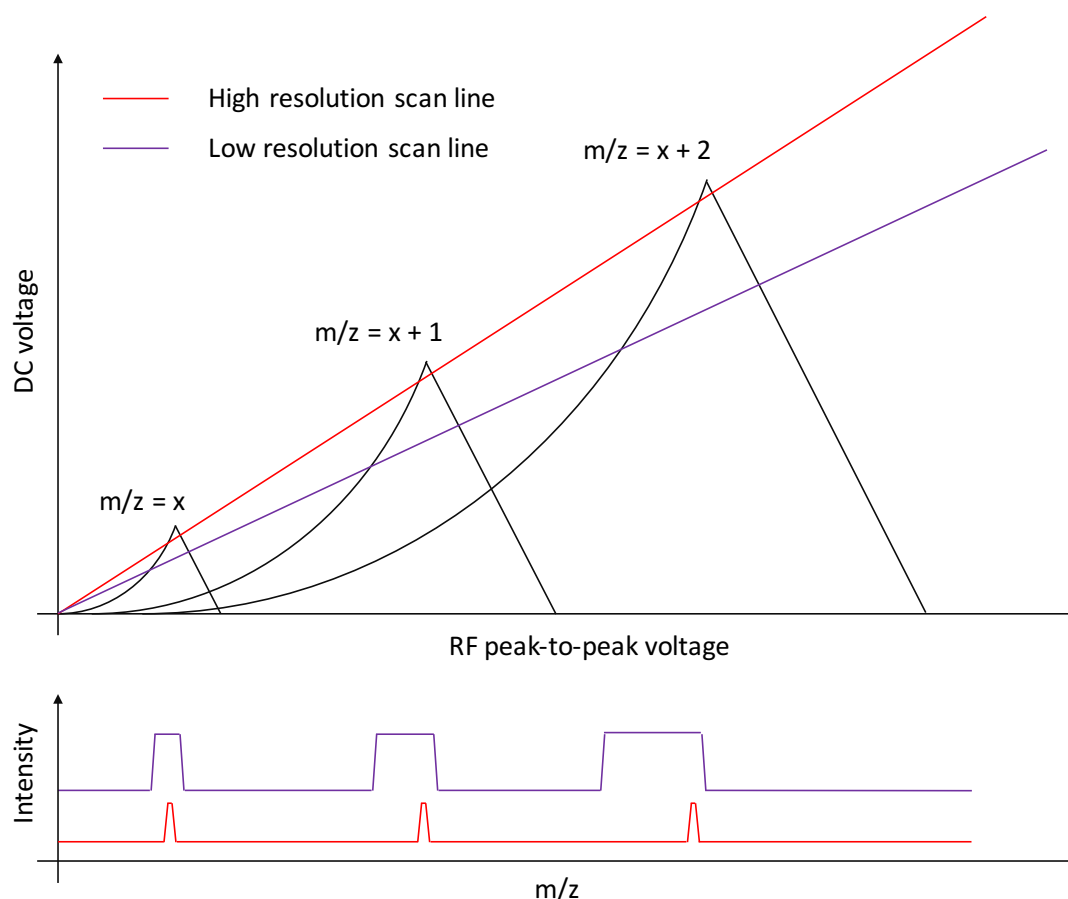
Figure 2.9 Graph demonstrating the effect of varying the RF:DC voltage ratio to change the resolution of a quadrupole mass filter and the corresponding expected mass spectra. The intensity offset between mass spectra is arbitrary in order to make the difference clearer.

By varying the ratio of RF voltage to DC voltage (the gradient of the line seen in Figure 2.9) it is possible to change the filtering power of the quadrupole mass-filter (as has been depicted in Figure 2.9). One can also completely eliminate the DC voltage from the applied signal, in such instances the quadrupole can be used as a high pass filter with minimal mass discrimination (such as is the case with a typical multipole ion guide used solely for transport of an unfiltered ion beam). Lowering the resolving power of the mass filtering (moving from the red line to the purple line in Figure 2.9)

also increases the total transmitted current of each ion so there are advantages to doing this if one is concerned about overall ion counts in the instrument.

In the context of this work, the mass filtering quadrupole has been used in two modes. Firstly, as a mass-filtering device to analyse the composition of ion beams. Secondly, as a high pass filter where it acts as an ion guide to transmit ions from one section of the instrument to the next.

2.4 Scanning Tunelling Microscopy

2.4.1 Introduction

The scanning tunnelling microscope (STM) has made possible the routine analysis of surfaces with sub-nanomeric resolution. Since the first demonstration of the application of quantum tunnelling to image surfaces by Binnig and Rohrer in 1982[82,83] STM has had a wide ranging and sustained impact on the field of surface science. The STM has a number of further interesting analytical capabilities which will not be discussed here but can be found in the references given[84,85]. In this section the basic theory and principle of operation will be discussed to the extent the instrument has been used in this work.
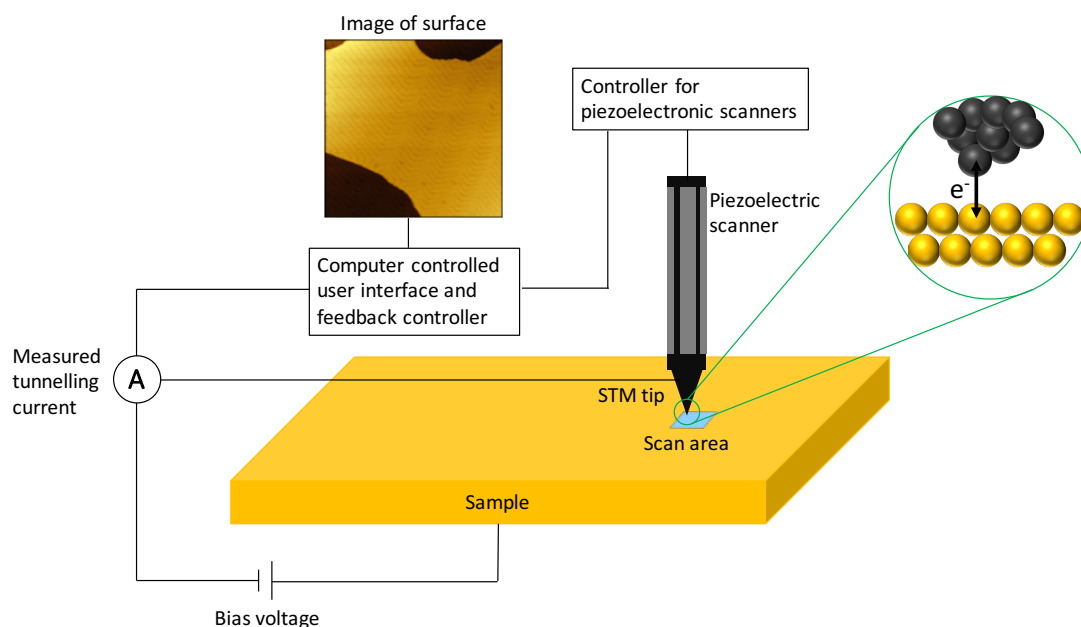
Figure 2.10 Schematic of a scanning tunnelling microscope.

2.4.2 Basic principle of operation

The STM consists of several parts which are common to every variant of machine. They are: the STM tip, an electrically conductive sample, a piezoelectronic scanner, a computer interface and feedback mechanism control (a typical set up can be seen in Figure 2.10). In an STM experiment, the STM tip is approached to within a few Angstroms of the sample. The wavefunctions associated with the tip and sample decay exponentially into the vacuum gap between. At this critical separation of a few Angstroms an overlap between the wavefunctions of the tip and sample can occur. This overlap enables electrons to quantum mechanically tunnel across the vacuum gap. The decay of the wavefunction into the vacuum gap can be constructed from the solution of the Schrödinger equation for a particle with a rectangular barrier of height Φ, which in the case of the STM is the work function of the tip or sample.

$$\Psi = \Psi_0 e^{-2\frac{\sqrt{2m(\Phi-\epsilon)}}{\hbar}d}$$

Equation 2.8

Where Ψ_0 is the wavefunction of the tip or sample before passing through the barrier, *m* is the mass of an electron and *d* is the distance across which the wavefunction has decayed (for example the distance between tip and sample).

With no voltage bias applied between the tip and sample, electrons flow evenly in both directions (from tip to sample and from sample to tip). After an equilibration between the Fermi levels of the tip and the sample, this results in no net current. When a negative bias is applied to the sample the probability of electrons flowing from the sample to the tip becomes more favourable and an overall current is seen. The same is true of a positive sample bias however the flow of electrons is in the opposite direction. These three scenarios have been shown in Figure 2.11
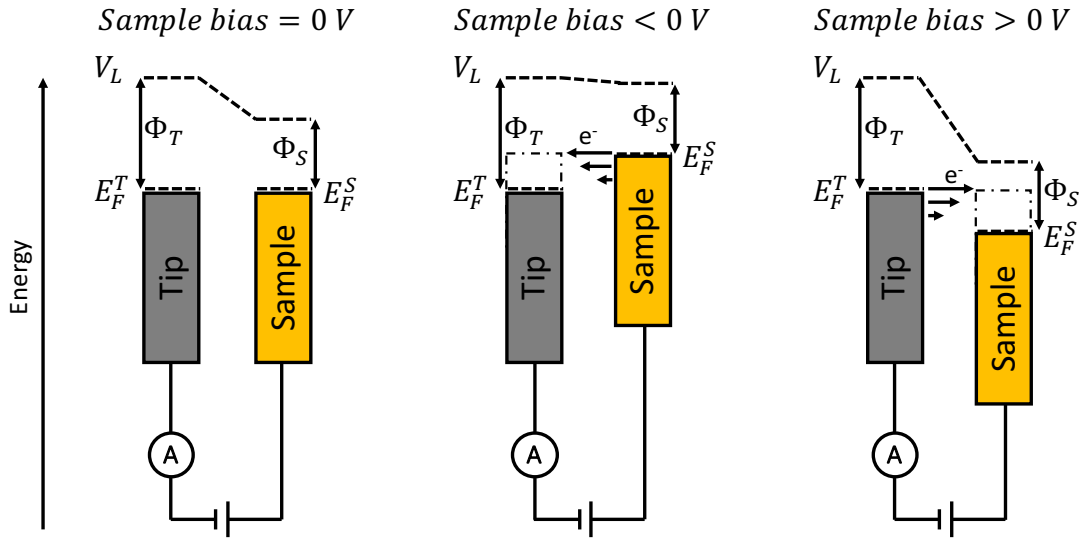
Figure 2.11 Energy level diagrams of an STM tip-sample junction showing three different scenarios based on the sample bias voltage.

The total current which flows between tip and sample can be given by the following equation which has been derived by Tersoff and Hamann[86] using Fermi's golden rule to calculate the transition probability of electrons per unit time.

$$I = \frac{4\pi e}{\hbar} \int_{-\infty}^{\infty} \left[f_T\left(E_F^T - eU + \epsilon\right) - f_S\left(E_F^S + \epsilon\right) \right] \cdot \rho_T\left(E_F^T - eU + \epsilon\right) \rho_S\left(E_F^S + \epsilon\right) |M_{TS}|^2 d\epsilon$$

Equation 2.9

Where $\hbar$ is the reduced Planck constant, e is the charge on an electron, $f_T(E)$ and $f_S(E)$ are the contributions from the Fermi-Dirac distribution at energy E for the tip and sample respectively which corresponds to the population of energy states at a given temperature, U is the bias applied across the tunnel junction between tip and sample, $\rho_T(E)$ and $\rho_S(E)$ are the density of states (DOS) for the tip and sample respectively, M_{TS} is the matrix which describes the wavefunction overlap between the tip and sample.

This equation can be simplified considerably for practical purposes. Firstly, since typically the bias voltage is on the order of ±1-2 V the contributions of tunnelling from thermally excited electrons are negligible and therefore the contribution of the Fermi-Dirac distribution can be ignored. The second simplification which can be made is to the tunnelling matrix. Since solving the tunnelling matrix requires an explicit knowledge of the exact wavefunction associated with both the tip and sample this is a

useful simplification. Since the overlap of tip and sample wavefunction are exponentially dependent on the distance between them (Equation 2.8) the tunnelling current is dominated by those atoms which are closest to one another, in the case of an STM experiment that is the atom at the apex of the tip and the surface atom closest to this. As such the tunnelling matrix can be simplified to a one-dimensional tunnelling probability which is of the same form as the solution to the Schrödinger equation for a rectangular barrier we saw earlier (Equation 2.8).

$$P(\epsilon) = P_0 e^{-2\frac{\sqrt{2m(\Phi_{eff}-\epsilon)}}{\hbar}d}$$

Equation 2.10

Where $P(\epsilon)$ is the one-dimensional electron tunnelling probability at energy ϵ. From this simplification the STM tunnelling current can be approximated as

$$I \sim \frac{4\pi e}{\hbar} \int_0^{eU} \rho_T(E_F^T - eU + \epsilon)\rho_S(E_F^S + \epsilon)e^{-2\frac{\sqrt{2m(\Phi_{eff}-\epsilon)}}{\hbar}d}d\epsilon$$

Equation 2.11

It should be noted that this approximation holds for a positive bias, whereas for a negative bias the limits of the integration should be inverted. From this equation we can see that the tunnelling current varies with the DOS, bias voltage and tip sample separation. If the sample has a constant DOS across the surface, the topography of the surface can be extracted by monitoring the current. The situation becomes more complicated where the DOS varies for different areas of the sample. An example of this may be when organic molecules are deposited on a surface. The energy level diagram associated with this can be seen schematically in Figure 2.12.
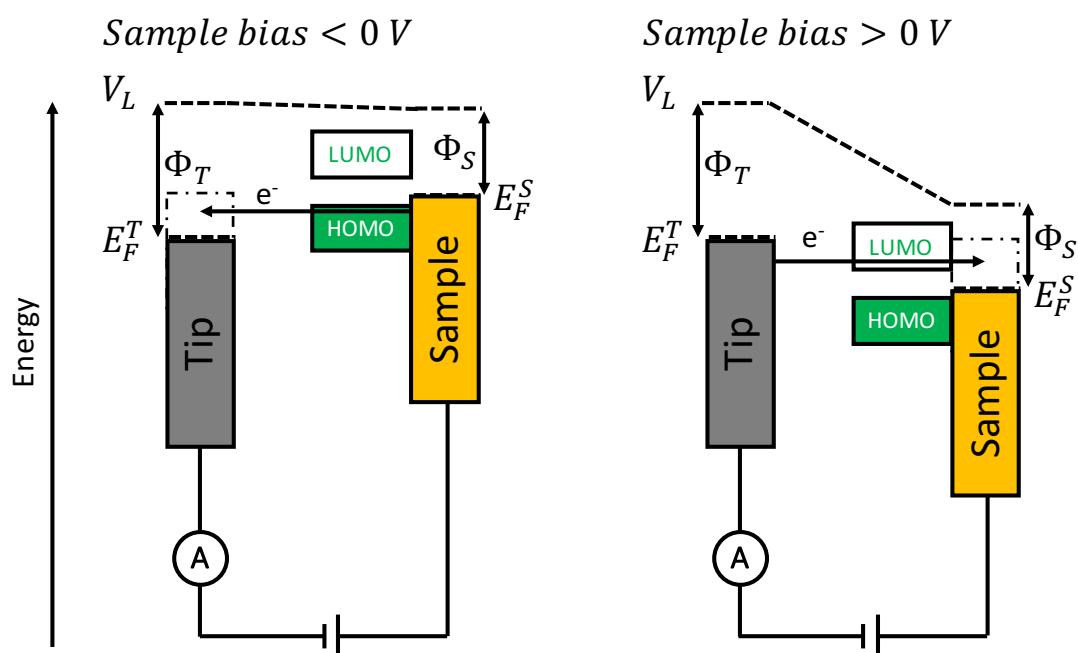
Figure 2.12 Schematic of the energy level diagrams associated with an STM experiment where imaging of the HOMO and LUMO orbitals of a molecule adsorbed on a surface is observed.

In this example, a molecule has been adsorbed to the metal sample, with the highest occupied molecular orbital (HOMO) lying below the Fermi level of the sample and the lowest unoccupied molecular orbital (LUMO) lying above the Fermi level of the sample. In the scenario where a negative sample bias has been applied electrons tunnel from the HOMO of the molecule into empty tip states, where the bias is positive, electrons from the filled tip states tunnel into the LUMO of the molecule. In this simplistic scenario it can be concluded that therefore in these two situations it is possible to measure the DOS associated with the HOMO and LUMO of the molecule. However, several complicating factors can cause this not to be the case. The electronic structure of organic molecules can be significantly modified through adsorption to metal surfaces which may mean a significant degree of hybridization between the molecular states (HOMO and LUMO) and metal states may have occurred. It is therefore important to remember that STM images represent a convolution of the topography of a sample as well as the DOS associated with the molecules and the underlying sample.

2.5 Operating in ultra-high vacuum (UHV)

Ultra-high vacuum (UHV) is defined as an environment where the pressure is lower than 10^{-9} mbar. Many surface science techniques are exclusively (or nearly exclusively) carried out under UHV conditions. All of the STM experiments contained within this thesis have been carried out in UHV. Although STM can be readily conducted in ambient conditions[87], UHV affords the ability to work with a wide range of surfaces that are otherwise incompatible with ambient conditions. In addition to this further benefits can be had from the clean environment in avoiding contamination which can often lead to STM images of a lower resolution.

In order to achieve a UHV environment specific equipment must be used. One of the main problems in achieving UHV is the outgassing of components which limits the ultimate pressure of the system. Stainless steel chambers and vacuum pumps with high pumping speed have both been used to overcome the hurdles in reaching UHV. Stainless steel chambers have been chosen due to their low out gassing properties[88].

A series of steps are taken in order to create a UHV environment. Firstly, the system is roughly pumped to a low vacuum with a scroll pump[89] achieving a vacuum of around 10^{-2} mbar. Following this, turbomolecular pumps can be used to reach a high vacuum (HV) of around 10^{-8} mbar[90]. Once this pressure is reached the limiting factor in reducing the pressure further is from the presence of hydrocarbons, water and other adsorbates which are present on the inner walls of the chambers[88] and outgas at a rate which is comparable to the speed at which the pumps can remove material. In order to overcome this, the system is heated to around 120 °C for approximately 48-72 hours. The contaminants desorb from the chamber surfaces at this temperature and are removed from the system through pumping. Additional pumping (such as ion pumps and getter pumps[89,90]) can be used to maintain the UHV conditions.

2.6 Conjugated polymers

2.6.1 Introduction

A polymer is a macromolecule consisting of repeating units called monomers, every aspect of human life has been influenced in some way by polymer materials and there continues to be a staggering amount of research into every aspect of their synthesis and properties. Conjugated polymers are a class of polymer where an sp^2 orbital extends along the length of the polymer backbone. As such, charge can flow freely

along the length of the polymer allowing them to be used in a number of electronic devices from solar cells[91], to light emitting diodes[92,93] as well as other examples[94,95]. Conjugated polymers are extremely promising in this respect as they have several advantages over traditional inorganic compounds[96]. For example, devices containing conjugated polymers can be made to be flexible as well as having a reduced manufacturing cost from the possibility of solution processing.

2.6.2 Structure and synthetic techniques

This thesis is not concerned with the specific methods of synthesis which organic chemists use in order to synthesise conjugated polymers, however, it is useful to understand the basic mechanism in order to interpret the results we see in later chapters.

For the most part, the conjugated polymers in this thesis fall into two categories: homopolymers and alternating co-polymers. Homopolymers are polymers where the chain consists of a single monomer. Alternating co-polymers consist of alternating monomer units. The synthesis of a homopolymer can be achieved through a range of routes[97] and is relatively straightforward and well understood. The synthesis of alternating co-polymers is less well understood and involves more complicated synthetic strategies[91,98–101].

A typical reaction schematic can be seen in Figure 2.13 where monomer A and monomer B react together in a 1:1 ratio to form an alternating $(AB)_n$ structured polymer. This is achieved through the use of a metal catalyst which selectively promotes the cross coupling of monomer A to monomer B[98,99,102]. Several variants of this technique exist where different monomer substituents (identified as X and Y in Figure 2.13) are paired with different metal catalysts[102–104] in order to achieve polymerisation of a wider range of monomer materials. Several review articles[91,100,105] regarding these techniques go into more detail about the specific mechanisms which are beyond the scope of this work.
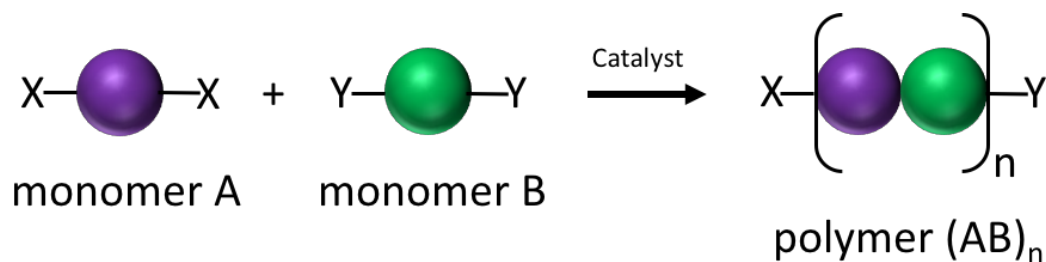
Figure 2.13 Schematic of the overall procedure for producing an alternating co-polymer.

The final structure of a conjugated polymer is typically probed by a number of techniques including nuclear magnetic resonance (NMR)[106,107], ultra-violet/visible spectroscopy (UV/vis)[26] and size exclusion chromatography (SEC)[98,108]. However, these techniques are known to have problems in accurately identifying the structure of the polymer chain

2.6.3 *Use in devices*

In order for the favourable properties of a conjugated polymer to be utilised to their full potential they must be configured into a useable device. Shown in Figure 2.14 is a schematic energy level diagram of an organic electronic device. The conjugated polymer is only one section of this device (the donor) and several other components are required for the device to function effectively.
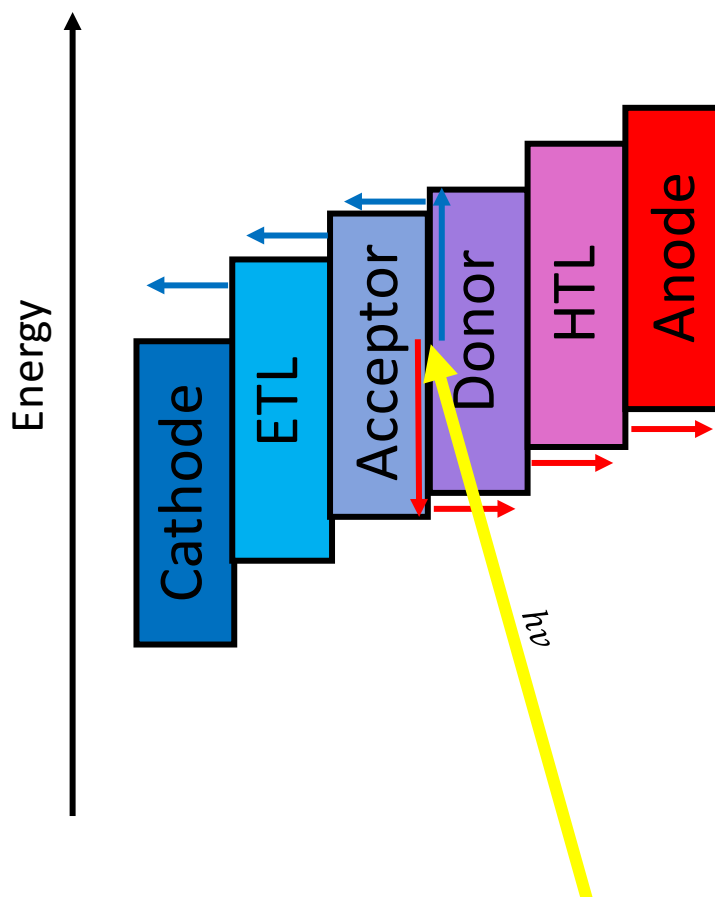
Figure 2.14 Energy level diagram for a typical organic photovoltaic solar cell. Blue arrows represent the path of electrons and red arrows represent the path of holes.

The operation of the device works in the following steps which are also shown in Figure 2.14. These steps represent a simplification of the overall process and for a fuller overview see the reference provided which includes many complicating factors which are beyond the scope of this discussion[4]. First, a photon (of energy *hv*) is absorbed by the photoactive layer; the donor and acceptor materials. In an organic solar cell, the donor material is typically the conjugated polymer and the acceptor material a fullerene or derivative thereof[109]. The absorption of the photon results in the creation of an electron-hole pair (an exciton) which is quickly separated at the donor-acceptor interface. The electron then flows towards the cathode and the hole towards the anode, generating an electrical current. The important aspect of this device is the interface between the donor and acceptor materials. This junction is where the initial separation of the hole and electron occurs. In order to maximise the efficiency of these devices this junctions surface area is maximised which can be achieved through mixing the donor and acceptor molecules to create what is known as a bulk

heterojunction[110]. In the case of alternating co-polymers the structure is often chosen such that monomer A and B represent donor and acceptor units within the polymer itself[111]. In this way an initial charge separation can occur within the donor molecules with the aim of reducing the likelihood of recombination of the electron hole pair[111].

3 Materials, methods and experimental setup

3.1 Super Electrospray Ionisation Source Made in Coventry (SEISMIC)

3.1.1 Introduction

SEISMIC is an instrument developed to overcome the limitations of thermal sublimation and to provide a sophisticated deposition system for a wide range of molecules. The aim was to build a system that could prepare surfaces both in high vacuum and ultra-high vacuum with control over landing energy and surface coverage whilst also having the ability to determine the exact composition of molecules in the beam by using mass spectrometry techniques. SEISMIC has been designed to use an electrospray ionisation source as a tool to deposit large molecules in vacuum with high control and precision. The system can be used to mass-select and energy-select molecules and deposit them at a controlled coverage on numerous substrates. This chapter presents the simulations, and 3D CAD drawings used to construct the instrument. Full details of the performance and characterisation of the system will be discussed in Chapter 4. In particular, in this first section we focus on the instrument, the main constituent parts, why they were chosen and the design principles behind each of them. A number of similar electrospray deposition systems already exist[13–16,19] however in this work we aimed to improve on these designs and create an instrument for our specific needs. That is: a compact, easily modified, robust, user-friendly system with a high ion flux and the ability to mass and energy select the ion beam. The system also includes the capability of depositing under both HV and UHV stages and is coupled to a UHV STM which can be accessed without breaking the vacuum.

SEISMIC consists of three main sections: the elctrospray interface; the ion guides and ion optics; and the deposition stages (HV and UHV). The electrospray interface is where ions are generated and first enter the system. The ion guides and optics are used for transferring the ion beam through the small apertures present in the system as well as for characterisation and mass-selection of the beam. Finally, the soft-landing deposition apparatus is a custom built set of lenses and sample housing used to slow or accelerate ions when being deposited onto a substrate under either HV or UHV.
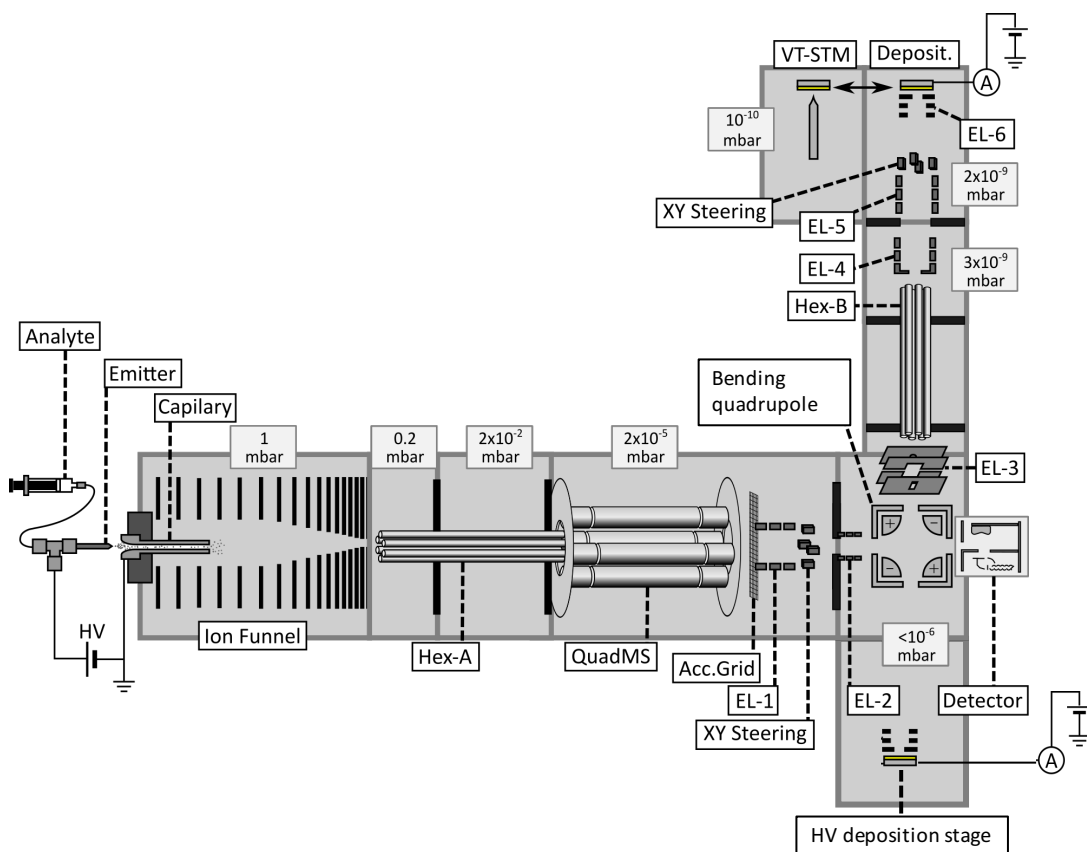
Figure 3.1 Schematic overview of the SEISMIC instrument showing the pressures and components in each of the differentially pumped chambers (not to scale).

An overview of the instrument is shown in Figure 3.1. SESIMIC consists of a series of custom built stainless steel vacuum chambers each of which has been specifcally designed to house certain components of the system. Each chamber contains a pump, a vacuum gauge and part of the ion guiding apparatus. The design of each of the sections will be discussed in more detail below.

3.1.2   Differential pumping of SEISMIC

The electrospray ionisation process occurs at atmospheric pressures[12]. However, for many surface science studies, surfaces are required which are highly reactive to atmosphere. For example, Cu(110) is a surface which has often been used in the literature to study the adsorption of small peptides[112,113], but it is so highly reactive that, if exposed to atmosphere, it would be fully oxidised within a fraction of a second. As such the Cu(110) sample must be held under vacuum conditions in order to maintain an atomically clean substrate; to be precise, Cu(110) is typically held at a pressure of 10^{-10} mbar or lower in order to prevent oxidation for any reasonable amount of time (several days) to allow for experiments to be carried out on this

surface. In order to deposit molecules onto the Cu(110) substrate using an electrospray ionisation interface (such as for the study of larger peptides which fragment when subjected to thermal evaporation) ions must be transported from atmospheric pressure (10^3 mbar) to UHV (10^{-10} mbar), bridging a pressure differential of 13 orders of magnitude. This is a more complicated task than is typically found in electrospray mass spectrometers where the vacuum required for mass-selection and detection of ions is typically much lower (10^{-7} mbar). In order to achieve this pressure drop SEISMIC comprises 8 vacuum chambers. Each chamber is equipped with its own pump and is separated from the neighbouring chambers by a small hole of a few millimetres in diameter (this value ranges from 0.5 mm at the smallest to 2.4 mm at its largest, and is equal to 2 mm for the majority of the chambers). Differential pumping is used to gradually lower the pressure from 10^3 mbar to 10^{-10} mbar. Although this solution allows to overcome the 13 orders of magnitude in pressure difference between the start and the end of the deposition source, it also introduces several challenges. For example, the introduction of small apertures between chambers which are needed to limit the gas flow from one chamber to the next (the differential hole limits) make the transmission of ions much more difficult than using larger aperture holes where ions could be more easily transmitted. The solutions to this and further challenges will be discussed in this chapter.

Figure 3.1 shows a schematic view of the 8 chambers and their typical pressures under operating conditions. Extensive pumping calculations (performed by Dr. Luís Perdigão) were used in order to optimise the interplay between the size of the holes separating the various chambers and the characteristics of the pumps needed to achieve the targeted decreasing pressure profile. From these calculations the number of chambers, approximate hole diameters and required pumps were determined and can be seen in Table 3.1 along with the final measured pressures.

Table 3.1 Chamber name and corresponding aperture size, pumping speed and measured pressure value. No pressure value is obtained for Hexapole B - stage 1 as no vacuum gauge is fitted here.

Chamber	Hole diameter from preceding chamber / mm	Pump speed / l/s	Pressure / mbar
Ion funnel	0.5	69	0.8
Hexapole A – stage 1	2	8	0.2
Hexapole A – stage 2	2.4	60	2×10^{-2}
Mass-filtering quadrupole	2.4	500	2×10^{-5}
Bending quadrupole	2	300	1×10^{-6}
Hexapole B – stage 1	2.4	67	-
Hexapole B – stage 2	2.4	67	3×10^{-9}
Preparation	2.4	67	2×10^{-9}

There are two different types of deposition that can be carried out with SEISMIC when considering the pressure the sample is held at: high vacuum, and ultra-high vacuum. We first consider the HV deposition stage. This stage can be seen in the lower part of Figure 3.1, lying at 90° from the entrance and can be reached by ions that have been directed this way via the "down" setting of the bending quadrupole. If instead a UHV deposition is required, the bending quadrupole is put in the "up" setting, so that the ions follow the path towards the preparation chamber (schematically shown at the top of the same figure).

In order to achieve pressures of less than 10^{-8} mbar in the final sections, a baking is required, so as to remove the residual adsorbate film (mostly composed of water) that persists on the inner walls of the steel chambers even after prolonged pumping. If this is not removed molecules will continue to desorb and limit the ultimate pressure of the system to around 10^{-8} mbar. Only the final stages of SEISMIC are baked (bending quadrupole, hexapole B, preparation chamber) which are separated from the rest of the system by a minimum thickness gate valve[114] (discussed in 3.1.8). During the baking, the chamber is heated to approximately 120 °C whilst being pumped for around 24-48 hours.

The differential pumping of SEISMIC is an effective way to create a vacuum interface between two processes that occur at very different pressures. Through careful chamber

design and consideration of pumping speeds we have been able to create a pressure differential which matches the needs of our UHV experiments.

3.1.3 Electrospray ionisation interface

The electrospray ionisation interface is the assembly of components used in order to generate the ion beam and transfer it with high efficiency to the first pumped stage of the instrument (for a detailed description of the formation of the electrospray see section 2.1.2). The interface assembly consists of the syringe and syringe pump used to deliver the solution to the emitter capillary where ions are produced and transmitted via the funnel inlet capillary. We use a Harvard Apparatus 11 plus programmable syringe pump with a 5 ml Hamilton glass syringe with a Luer lock connected to PTFE tubing. The tubing ends in a T junction where the electrical potential is applied to the solution by a stainless steel metal rod (see Figure 3.2). The T junction is mounted on a 3 axis positioner so that the emitter can be precisely aligned with the inlet capillary.

The electrospray ionisation interface and its transmission are very important for the overall performance of the instrument as this is where most of the ion losses occur[115].
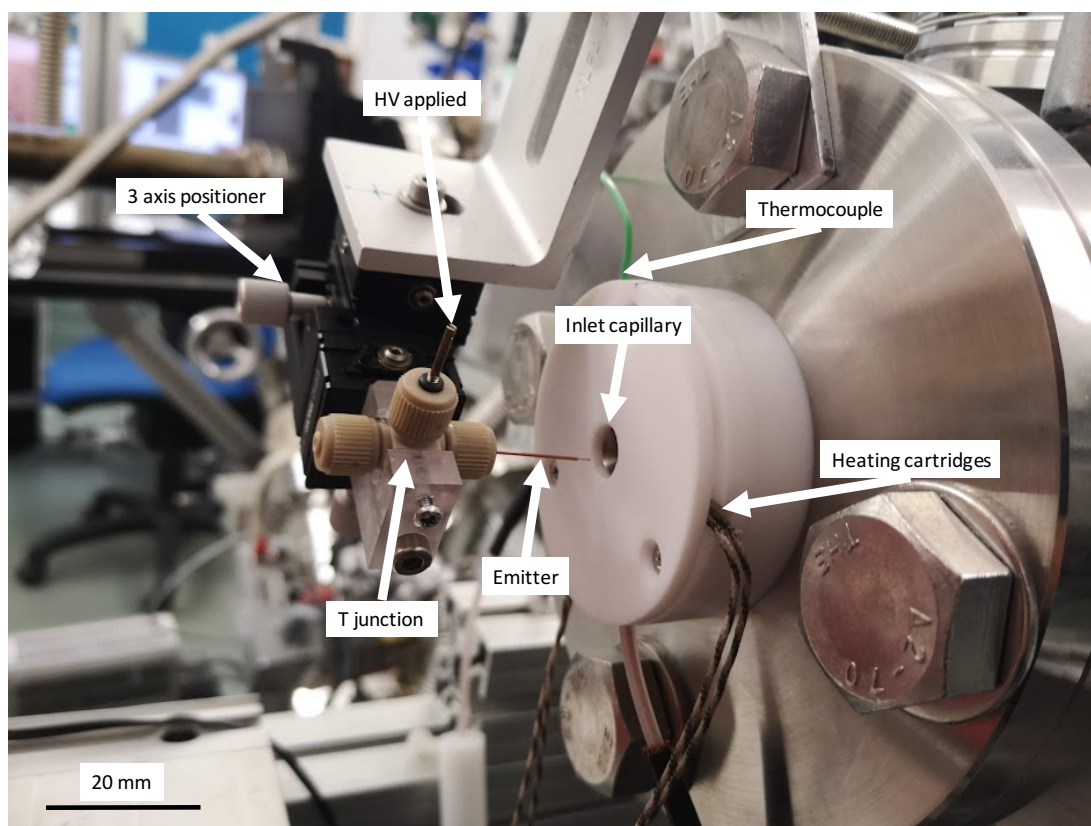
Figure 3.2 Labelled photograph showing the components which constitute the electrospray ionisation atmospheric interface.

41

The entrance capillary is a design from Rauschenbach and co-workers[115]. This funnel inlet (Figure 3.3) allows for a higher transmission of ions from the atmospheric interface into the first stage of the differentially pumped system. The shape of the funnel is such that the gas flow pulls ions in and aids in overcoming the electrostatic repulsive force between like charged particles (the so-called space charge field). It was shown that this shape of entrance capillary could achieve unity transmission for a range of samples[115] and therefore was chosen for use in SEISMIC. The tube capillary section after the funnel (see Figure 3.1) has an inner diameter of 0.5 mm and is 70 mm long.
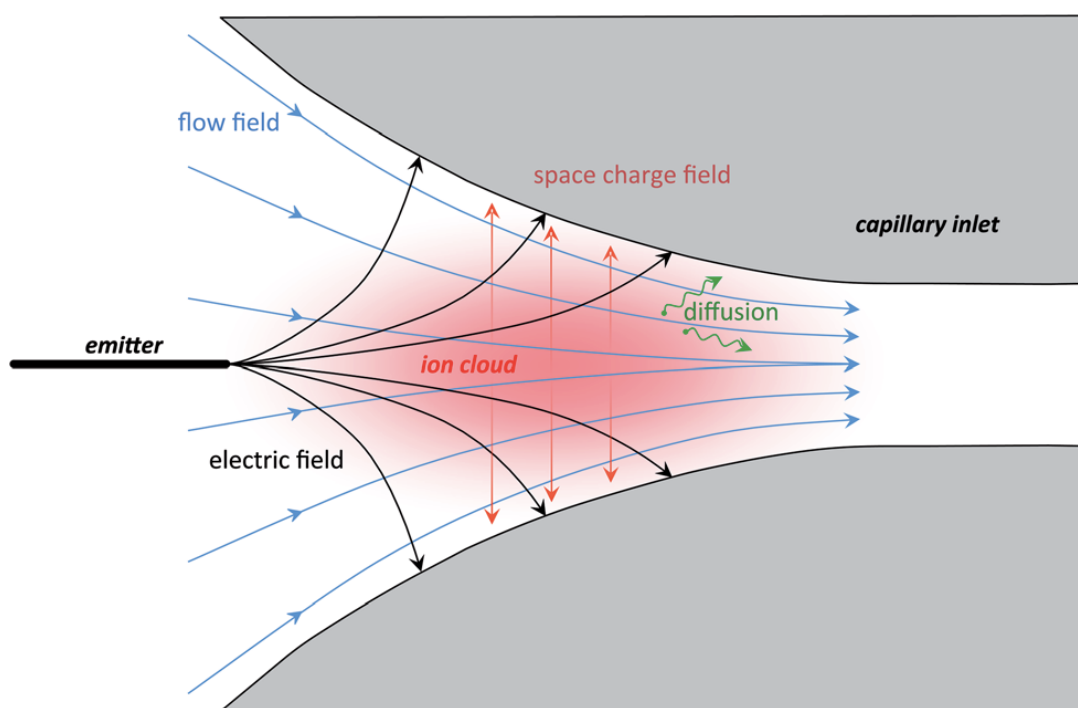
Figure 3.3 Schematic of the entrance capillary showing the competing forces acting on the ion beam. Adapted from Rauschenbach and co-workers[115].

The funnel capillary has been built into a flanged interface (Figure 3.2). The PTFE holder for the capillary also houses a copper block into which heating cartridges are placed, capable of heating the copper block to approximately 300 °C. The funnel capillary is fitted into this copper block to allow for the heating of the electrospray as it passes into the first differentially pumped chamber. This heating aids in the desorption of solvent molecules[116] and is essential for obtaining high ion currents in

the instrument. The screw-in design of the capillary into the copper block ensures a simple removal of the capillary for cleaning purposes and allows to easily test new capillary designs without the need of disassembling the main chamber. The heating cartridges can also be easily replaced and changed for others with increased power output, allowing the system to achieve even higher heating temperatures, if required.

3.1.4 Ion funnel

Simulations and design of the ion funnel were completed by Dr Luís Perdigão and Dr Alex Colburn. The electronics which control the ion funnel were designed and assembled by Dr Alex Colburn.

Beyond the flanged capillary interface is the first differentially pumped chamber of SEISMIC. The stainless steel chamber is connected to a rotary vane pump (pumping speed = 250 m^3/h) and has a base pressure of approximately 0.8 mbar. Within the chamber is the ion funnel (Figure 3.4), which is mounted to the chamber by a custom designed holder.
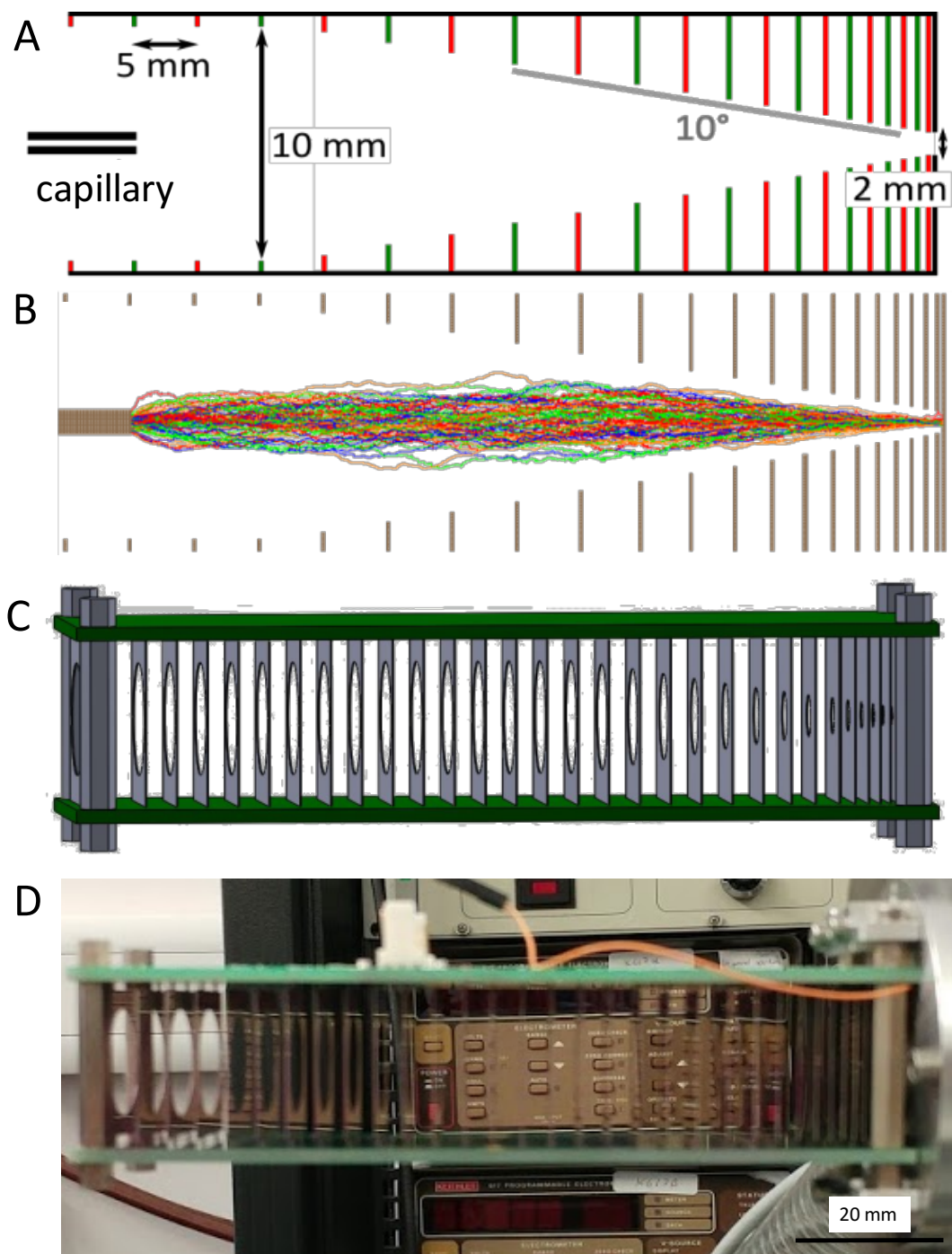
Figure 3.4 Overview of the ion funnel. (A) Schematic design of the ion funnel assembly showing the capillary entrance, electrode spacing and exit aperture. (B) SIMION simulation of ions travelling through the ion funnel (see text for more details). (C) 3D CAD of the ion funnel. (D) Photograph of actual device.

An ion funnel is a device used to focus ions (of either polarity) using a series of ring electrodes which decrease in inner radius[117]. A combination of a radio-frequency (RF) field and an electrostatic potential is applied to these electrodes, in order to shape the

ion beam and direct it from one end of the funnel to the other. Ion funnels are typically used in pressure regimes of 0.3 – 30 mbar as collisions with the background gas are essential for good ion focussing[118].

The principle of operation is as follows. RF electrical signals of opposite polarity are applied to adjacent ring electrodes. This arrangement of electrodes creates an effective potential energy landscape which is used to confine the ions radially. The alternating potential also causes ions to oscillate rapidly within the confined region, which increases the probability of collisions with neutral background gas. These collisions act to thermalize the kinetic energy of the ions, making further focussing easier by decreasing the energy spread of the ions. In addition to this, a DC electrical voltage is applied to each of the ring electrodes. A series of resistors is employed so as to obtain a potential gradient along the main axis of the device. The potential gradient (along with the pressure gradient) causes ions to flow from one end of the device to the other. The size of the DC potential and the amplitude of the RF voltage can be controlled and tuned for each specific experiment.

A compact design of the ion funnel was chosen to allow for easy removal and cleaning. This is essential as the early stages of the instrument receive the highest flux of ions and can become contaminated over time. The ion funnel is made of two printed circuit boards (PCB) and a series of laser cut stainless steel ring electrodes. Each ring electrode is soldered to the PCB where the electrical signal is applied. The funnel itself is mounted to the exit flange of the first vacuum chamber with a custom built holder.

The ring electrodes have been specifically designed to create an effective potential which best captures and funnels ions from one end of the device to the other. The first 4 electrodes are of equal inner diameter (10 mm) and create what is called the ion conveyor, needed to collect ions emerging from the entrance capillary; the remaining electrodes decrease in diameter along a 10° gradient (from 10 mm down to 2 mm). As the ring electrodes get smaller in diameter the distance between them also decreases. This was shown in simulations to have the highest transmission, the results of which can be seen in Figure 3.4B. The first section of the ion funnel captures and re-collimates the ions exiting the entrance capillary, preparing them for further focussing by the ion funnel. Due to the significant change in pressure between atmosphere and the first vacuum chamber, these ions undergo a rapid in-vacuum expansion in a region

referred to as the Mach disk[77], where no collisions with background gas occur. The axial extension of the Mach disk, x, is dependent on the diameter of the entrance capillary, D_0 and the ratio between the pressures, $P_{ambient}$ and P_{vacuum} on either side of the capillary. This can be calculated from the following formula

$$x = 0.67 D_0 \sqrt{\frac{P_{ambient}}{P_{vacuum}}}$$

Equation 3.1

Using this distance, which extends from the exit of the capillary, we have designed the ion conveyor region to be greater than this in order to capture the maximum possible number of ions where no collisions occur. The successive funnel region narrows to a final diameter of 2 mm which acts as the differential pumping limit between first and second vacuum chambers.

3.1.5   Hexapole ion guide

The electronics used to control the hexapole were designed and assembled by Dr Alex Colburn.

After ions exit the ion funnel they enter the first hexapole ion guide. There are two hexapoles of the same design used in SEISMIC (Figure 3.1), one is before the mass-selecting quadrupole (hexapole A) and the other is after the bending quadrupole (hexapole B). Both hexapoles are identical in their operation and design principle and shall be discussed in this subsection; the only difference between them being the length of the overall device and the way in which the vacuum separation between its two sections (see later) is made.

A hexapole consists of 6 cylindrical rods placed in a circular geometry. As with the ion funnel, the hexapole ion guide is driven by an RF field on top of which a DC voltage is applied. Adjacent rods are set to RF voltages that are in antiphase, thereby producing an electromagnetic field which, similarly to the case of the ion funnel, confines the ions radially within the device. The field has been simulated using the SIMION software package and the resulting trajectories for a group of ions can be seen in Figure 3.5. A more thorough discussion of the operating principles was given in section 2.2.3.

Figure 3.5 SIMION simulation of hexapole. Blue lines represent the paths followed by ions (m/z=500) travelling through the hexapole. The confinement of the ions to the central region of the hexapole is clearly visible.

The hexapoles used in this instrument operate at 2 MHz and have an amplitude which can be set up to a maximum value of 250 V (peak-to-peak). The pressure differential and a DC voltage offset between the hexapole and the preceding component is used to direct the flow of ions into the device. The amplitude of the RF voltage can be used to control the degree of ion confinement (the shape of the effective potential, see section 2.2.3), while the DC voltage offset is also used in order to maximise transmission between stages. The design phase of the hexapoles was supported by SIMION simulations that used sets of ions with starting conditions given by the output of the ion funnel simulation file. In particular, ions ranging from 10-2000 m/z were used with an average longitudinal kinetic energy of 20-40 eV and a transverse kinetic energy of 1.5 eV. The optimum RF frequency, peak-to-peak voltages and DC offset were determined as those maximising the ion transmission. These values are then re-optimised once the device has been built (Chapter 4). These simulations values were then used to build electronics for the hexapoles and the simulated values are very close to those used in the final apparatus.

Both hexapoles of SEISMIC have a unique design by which they can be considered as a single device from the electrodynamic/ion transmission point of view, while at the same time being composed of two consecutive sections of decreasing pressure, when seen from the vacuum technological point of view. This design allows to keep all ions within the confining RF potential without losses while transporting them through successive stages of a differently pumped vacuum system.

In a traditional differentially pumped system, most losses of ions occur as the ions are forced to pass through the small apertures that separate successive differentially pumped vacuum chambers. If using a conventional sequence of hexapoles to transmit ions thorugh each of the vacuum chambers, one has to break the hexapole rods, place an aperture (in order to define the differentially pumped limit) and place the next hexapole section immediately after the vacuum separation. In this way ions are

subjected to fringe fields[77] which can cause significant losses and reduce the overall transmission. Fringe fields, however, are not the only problem; introducing a small aperture also requires additional ion optic devices (typically electrostatic lenses, see 2.2.2) to focus the beam through it and re-collimate the beam on the other side of the aperture. These are all areas where losses can occur and are therefore to be avoided if at all possible. The hexapole designed in this work have extremely small rods and an inner inscribed diameter of 2.4 mm, considerably smaller than hexapoles currently available from commercial suppliers. This allows to use the inner inscribed section of the hexapole rods as a differentially pumped vacuum separation if the outside region is completely sealed at a given position along the hexapole.

A schematic of the hexapole design is shown in Figure 3.6. The six rods (diameter = 1 mm) are made of brass and are soldered to two different custom designed brass plates, where the electrical signal is applied. Each brass plate is connected to 3 rods, each of the two antiphase RF voltages being applied to one of the two brass plates. The plates sit in PTFE holders, electrically isolating the plates and the rods from the rest of the enclosure and creating, together with the enclosure, the seal between successive vacuum regions. The enclosure consists of aluminium pieces used for rigidity and to enable mounting within the vacuum chambers; the enclosure is electrically grounded. The designs for hexapole A and hexapole B differ slightly due to the constraints of working in different vacuum regimes. Hexapole A, which is in the lower vacuum regime, is discussed first.
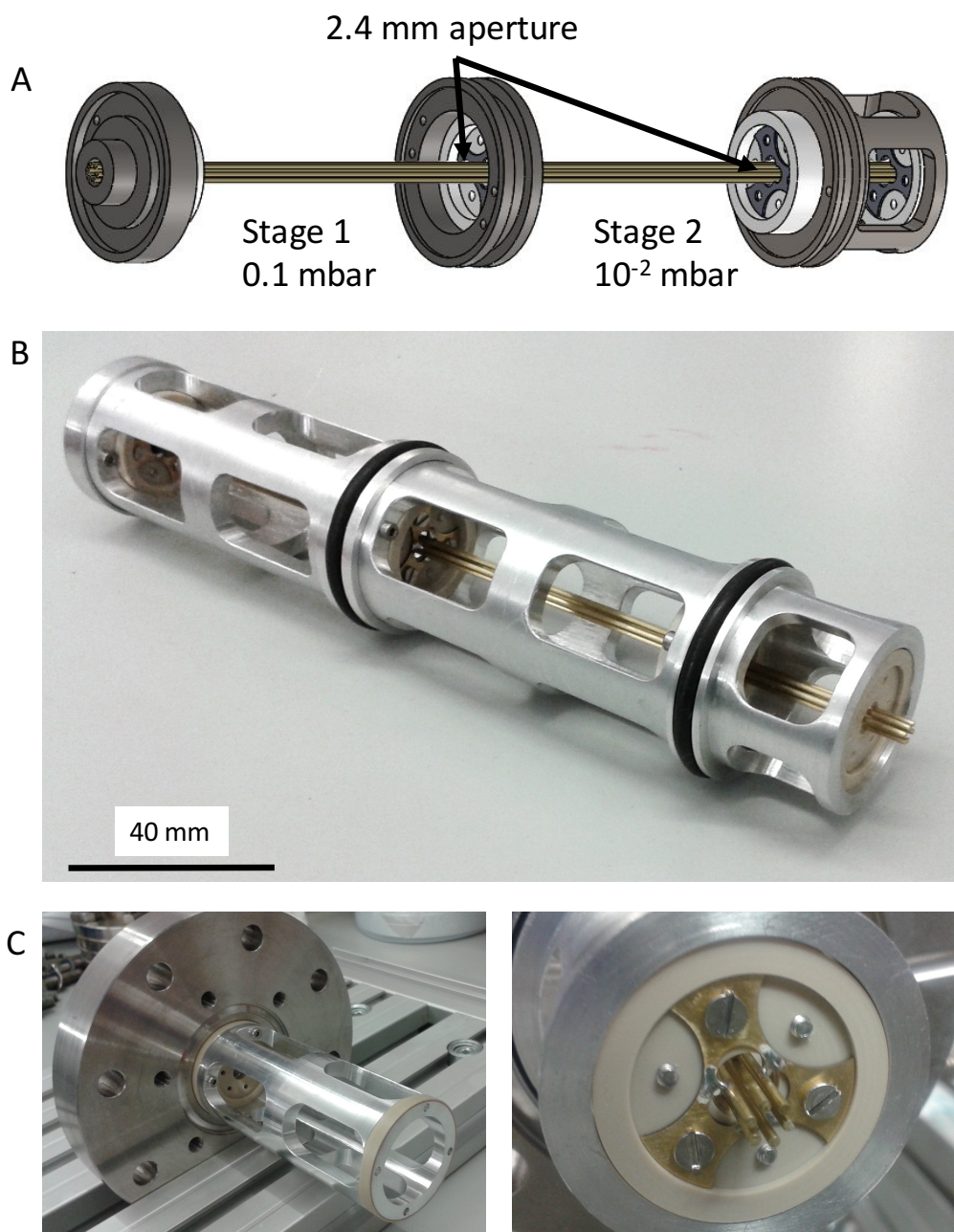
Figure 3.6 Overview of the hexapole apparatus. (A) Schematic 3D CAD drawing of hexapole A, showing the 2.4 mm aperture which separates the two vacuum stages. (B) Photograph of hexapole A. (C) Photograph of hexapole B highlighting the differential pumped seal created using a vacuum flange. (D) Photograph highlighting the soldering of the brass rods to the brass plate where the electrical signal is applied.

Hexapole A is used to transmit ions through from a starting pressure of 0.1 mbar (ions from the ion funnel) through to 10^{-5} mbar (where they enter the mass-selecting quadrupole). It consists of two differentially pumped seals and is therefore separated into three differentially pumped vacuum stages, the third stage of the hexapole being inside the quadrupole chamber. Stage 1 has a pressure of 0.1 mbar, and is pumped

with an Edwards rotary pump (pumping speed = 30 m^3/h); stage 2 is at 10^{-2} mbar and is pumped by a Pfeiffer turbomolecular pump (pumping speed = 60 l/s); stage 3 is at 10^{-5} mbar and is evacuated by an Edwards turbomolecular pump attached to the mass-selecting quadrupole chamber (pumping speed = 500 l/s). The seals ensure that the gas flow between the successive differentially pumped vacuum regions is limited to only the inner part of the hexapole rods (inner inscribed diameter = 2.4 mm). The seal is made by fitting fluoroelastemer O-rings to the outside of the aluminium enclosure and forms a tight vacuum separation by being pressed onto the inside of the stainless steel chamber. This latter has a cylindrical shape with a diameter just slightly larger than that of the aluminium enclosure. The advantage to this design is that the hexapole device can be easily push fitted and removed for modifications and cleaning, which is essential due to the high ion flux in this region of SEISMIC (similarly to the case of the ion funnel).

Hexapole B is used to transmit ions form 10^{-6} mbar (ions exiting the bending quadrupole and heading towards the UHV deposition stage) through to 10^{-9} mbar (where ions are soft-landed onto the substrate in the preparation chamber). Hexapole B has a single seal and is therefore split into two differentially pumped sections. The first section is at a pressure of 10^{-8} mbar and is pumped by a Pfeiffer turbomolecular pump (pumping speed = 67 l/s), while the second stage is at a pressure of 10^{-9} mbar (after baking) and is also pumped by a Pfeiffer turbomolecular pump (pumping speed = 67 l/s). The vacuum seal for hexapole B comprises a stainless steel flange to which the hexapole assembly (similar to that of hexapole A) has been mounted. A photograph of this can be seen in Figure 3.6C. O-rings cannot be used in this section due to the need to bake the system to achieve pressures in the UHV regime.

Multipole ion guides are ideal devices when ions need to be taken from one position to another with minimal losses[77], we have utilised this high transmission and pushed the design one step further by passing these hexapoles though differentially pumped limits. With our innovative design that integrates RF multipoles with a differentially pumped vacuum system, we have extended the functionality of these devices by achieving loss-less ion transport between regions of different pressure.

3.1.6 Mass-filtering device – Quadrupole

The end of hexapole A is situated 8 mm inside the mass-filtering device, implying that ions are immediately under its influence and avoiding the need for any further focussing component. In SEISMIC the mass-filtering device is a commercial quadrupole mass-filter purchased from Extrel. The rods are 9.5 mm in diameter and the device is capable of transmitting ions in the 20-4000 m/z range. The main purpose of the quadrupole is twofold: to check the composition of the ion beam; and to transmit only the molecules of interest. The quadrupole is not being used for identification of unknown molecular species (which would require a higher resolution mass spectrometer) but is instead being used to ensure that no side-reactions, contaminations, or fragmentations have occurred from sample preparation to electrospray ionisation. The quadrupole can also be used in RF-only mode whereby it acts as a high-pass m/z filter and affords much greater transmission than when in mass-filtering mode. The RF-only mode is reserved for experiments where high transmission is imperative and beam cleanliness has been previously ensured. The basic principle of operation of a mass-selecting quadrupole is given in section 2.3.2. The quadrupole is positioned in its vacuum chamber through a flange on which it is mounted via rods inserted into specific mounting holes. The chamber is at a pressure of 10^{-5} mbar and is pumped by the aforementioned Edwards turbomolecular pump (pumping speed = 500 l/s), and is separated from the successive vacuum chamber by an aperture with a diameter of 2 mm. In particular, because of the large inscribed diameter of the quadrupole (9.5 mm), severe losses would occur at this position If ions were not collimated and focussed before the apertures. For this reason, a lens assembly was designed and constructed (see next section), which is vitally important for achieving high ion transmission values.

3.1.7 Electrostatic lenses

The lenses discussed in this section have been developed in collaboration with Dr Luís Perdigão. SIMION calculations were performed by both Dr Luís Perdigão and the author, while the author completed all of the 3D CAD drawings as well as the design of the majority of the lenses. Dr Alex Colburn designed and built the power supplies which provide voltages to the electrostatic lenses.

At various stages in SEISMIC electrostatic lenses have been used to focus ions. The main purpose of these lenses is to focus the beam through a small differentially

pumped aperture or to collimate the beam so that it is more easily accelerated and transmitted.

Einsel lenses are electrostatic lenses which consist of three ring electrodes (normally with a cylindrical shape and a constant inner diameter) to which DC voltage are individually applied. Typically, the first and last electrode are at the same potential and the central electrode has a potential that can be varied in order to change the focal length of the device. As a consequence of having the first and last electrode at the same voltage ions are not accelerated or decelerated through this device. This is crucial when using the lenses to focus ions onto a sample for soft-landing as the the ions' kinetic energy is crucial in determining what sort of interaction they have with the surface[18,55,119]. The focal length of an einsel lens does not depend on the mass-to-charge ratio of the ions but is strongly dependent on their kinetic energy (as was discussed in section 2.2.2).

For all of the lenses designed for SEISMIC, SIMION calculations have been used to optimise their geometry and range of operating voltages. These simulations were typically run on a large number (>500) of ions with randomised starting velocities in order to sample a range of starting parameters to obtain reliable approximations of the voltages needed to achieve the desired focal lengths and spot sizes of the beam. Moreover, the ions' output conditions obtained from simulations of hexapole A were used as the input for the lenses directly after hexapole A in order to achieve results which can be considered close to what we would expect for the final device. This process was repeated with the output of the lens simulations being used for the next device and so on until the final set of lenses contained within SEISMIC.

Lenses have been used in SEISMIC at the exit of the mass-selecting quadrupole; the entrance and exit of the bending quadrupole; the exit of hexapole B; the free-flight region between hexapole B and the manipulator; and the soft-landing stage on the sample manipulator. A specific design was developed for each of them as can be seen in Figure 3.7, which shows the corresponding CAD models.

The first set at the exit to the quadrupole contains 3 lenses (diameter = 10 mm), an accelerating grid and a set of steering electrodes (Figure 3.7A). The specific design requirements of this particular set of lenses were: re-collimate the beam after it exits the quadrupole; accelerate the ion beam; focus the ion beam through a 2 mm aperture.

The accelerating grid is used to collimate and accelerate the beam while the 3 lenses work to focus the beam through the differentially pumped aperture. The accelerating grid is made of a stainless steel mesh with an open area of 83% to allow as many ions through as possible. In order to apply acceleration to the ions in only the longitudinal direction and not to spread the beam by applying a radial acceleration, grids have been chosen. By placing a grid after the quadrupole exit we aimed at achieving a linear acceleration field (analogous to the electric potential created between parallel plates). The accelerating grid is set to a voltage in the range of 30-40 V and defines the kinetic energy of the ion beam for the remainder of its flight before a final landing value is dictated by the final set of lenses (see below. The specific value of the acceleration value was determined from simulations that showed that a beam with kinetic energies of 30-40 eV was much easier to focus into the 2 mm aperture by the successive einzel lenses.

The steering electrodes can be seen in Figure 3.7A. They consist of four rectangular stainless steel blocks, with DC voltages applied in pairs (±x and ±y), and are located on the edge of a circle of diameter 10 mm. As the name implies, these electrodes are used to steer the beam of charged particles. After the beam has been collimated and focussed it is sometimes necessary to realign the beam with the aperture in the gate valve which follows the quadrupole. (see later). By measuring the current on the gate valve as a function of the voltages applied to the steering electrodes, a contour plot can be created (see section 4.1.6). This value of steering voltage is then used to send the ion beam through the aperture and correct any misalignment in the system. The steering voltages are applied in pairs (±x and ±y so a 3D contour plot of ±x, ±y and current is obtained).

The next set of lenses at the entrance of the bending quadrupole is formed of three ring electrodes with an inner dimeter of 5 mm (Figure 3.7B). They are mounted on the higher vacuum side of the minimum thickness gate valve and transport ions from the aperture of the gate valve into the bending quadrupole. The lenses are inserted into PEEK holders and are electrically isolated from the valve so that the ion beam current can be measured on the gate valve.
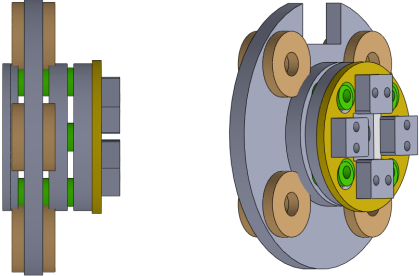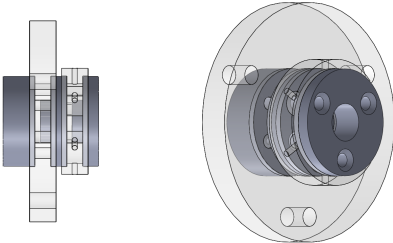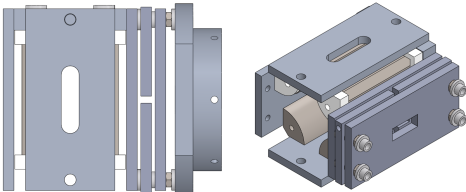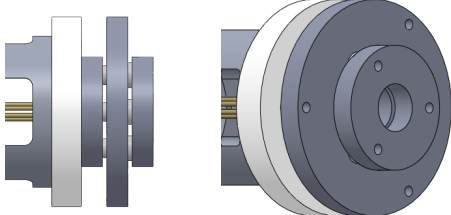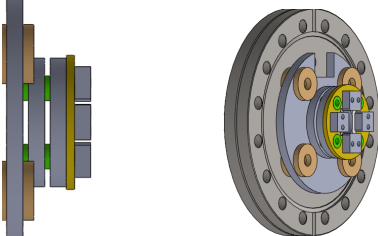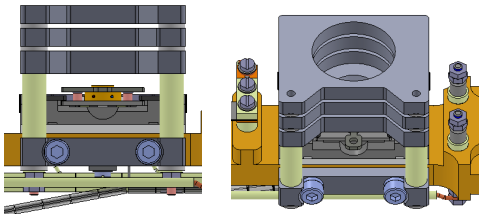
A	Post quadrupole	
B	Pre bending quadrupole	
C	Post bending quadrupole	
D	Post hexapole B	
E	Free flight region	
F	Manipulator	

Figure 3.7 Overview of all lens assemblies used in SEISMIC, see main text for full details of each.

There is a further set of lenses after the exit of the bending quadrupole which have a different geometry to the rest of the lenses used in SEISMIC. The potential landscape

of the bending quadrupole causes the exiting ions to be compressed in the xy plane but divergent along the z axis, which was determined through SIMION simulations. Therefore, a special lens was designed to counteract this effect and re-focus ions in the z axis (Figure 3.7C). The anisotropic focusing lenses consist of three aluminium plates, the first and third of which contain vertical slits of 10×5 mm. The second plate also contains the same vertical slit but is divided in two parts by a 5 mm gap; the application of two different voltages to the two segments, allows to steer the ion beam vertically. The vertically elongated geometry of the slits acts to counteract the divergence and re-create a circular geometry which is beneficial for focussing through the successive circular apertures.

The lenses situated at the exit of hexapole B consists of the standard three ring electrode configuration (Figure 3.7D). The electrodes are made from aluminium and have an inner diameter of 5 mm. The first ring electrode is mounted via a PEEK fitting to the end of hexapole B and has a small hole (2.5 mm diameter) which expands to the larger diameter (5 mm). This set of lenses collimates the beam exiting hexapole B and sends it into the lenses located in the free-flight region between the preparation chamber and the soft-landing lenses on the manipulator head.

Ions are transmitted through the free-flight region by a further set of einzel lenses (diameter = 10 mm) and a set of steering electrodes (Figure 3.7E) with a design that is identical to that of the lenses located after the mass-selecting quadrupole (Figure 3.7A). Both the einzel lenses and the steering electrodes are operated in an identical manner to what has been described previously.

Finally, the lenses used on the manipulator head are designed for the collection of ions from the free-flight region (Figure 3.7F). After collection the ions are focussed onto the sample and accelerated or decelerated to the required kinetic energy for that particular experiment by applying a voltage to the sample plate. These lenses consist of three electrodes with a diameter of 15 mm. The larger diameter is used here in order to collect as many ions as possible after the free flight region.

3.1.8 *Minimum thickness gate valve*
Adaptations to the gate vale design by O'Connor and co-workers[114] were completed by Dr Luís Perdigão.

As has been stated before, a high transmission of ions is absolutely paramount for a successful operation of SEISMIC. In order to achieve the ultra-high vacuum of the landing stage, the final sections of SEISMIC must be baked and a gate valve is needed to separate them from those first sections that are exposed to atmospheric pressure during baking (this is necessary as some components cannot be baked). Typical gate valves are large cumbersome devices and incorporating one into SEISMIC would result in a free-flight region of greater than 100 mm which we decide to avoid in order to minimise losses. These losses are particularly significant for the divergent beams which exit multipoles due to the fringe fields created by the multipoles[77] which cause ion trajectories which are far from collimated. We have chosen to incorporate instead a custom built minimum thickness gate valve adapted from the original design of O'Connor and co-workers[114]. This device has two sealed positions, open and closed. In the open position a 2 mm central aperture is aligned with the central axis of the quadrupole and lenses are used to guide ions through the hole (as discussed previously). This is the 'in-operation' position which is used for experiments. In the closed position the valve is sealed against the stainless steel plate with an O-ring holding the seal. The gate-valve is capable of holding a pressure differential of 11 orders of magnitude when tested (atmosphere versus 10^{-8} mbar vacuum). As mentioned before, the gate valve has a set of lenses mounted to the high vacuum side which are electrically isolated from it.

3.1.9 Bending quadrupole

SIMION simulations of the bending quadrupole were completed by Dr Luís Perdigão. The power supply for the bending quadrupole was designed and built by Dr Alex Colburn.

Ions which have been focussed through the minimum thickness gate-valve arrive at the bending quadrupole. The bending quadrupole within SEISMIC can be used to send ions in one of three possible directions: towards the HV deposition stage; towards the electron multiplier; or towards the UHV deposition stage within the preparation chamber.
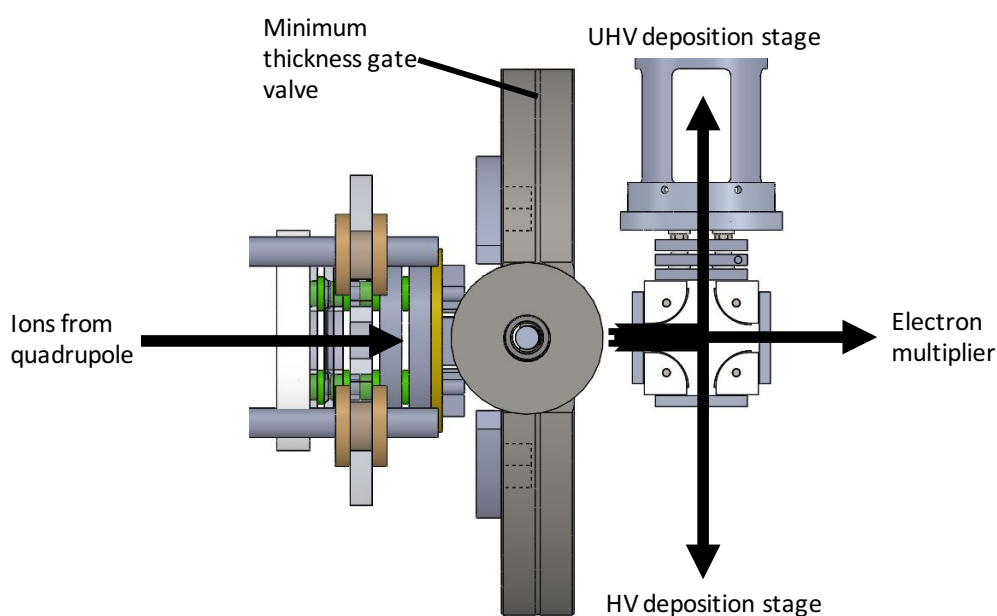
Figure 3.8 3D CAD of the exit lenses of the mass-selecting quadrupole, the minimum thickness gate valve and bending quadrupole assembly demonstrating the three paths ions can take at this stage of the instrument.

The bending quadrupole is a combination of four quarter-cylindrical rods (5 mm radius) placed on an inner inscribed radius of 15 mm. The geometry of the device is similar to that seen for the mass-selecting quadrupole. However, whereas the long axis of each of the rods in the mass-selecting quadrupole was parallel to the direction of ions' travel, in the bending quadrupole the rods are placed perpendicular to the ion path as depicted in Figure 3.9B (in this figure rods are shown as full cylinders which were used for simulation purposes). Also, whereas the mass-filtering quadrupole works with RF voltages the bending quadrupole has DC voltages applied to pairs of rods. For an ion beam travelling to the ion detector no voltage is applied, while in the

case of ions being sent to the deposition stages, typical DC voltages range from 0-50 V, depending on the energy of the ion beam. Optimisations can be completed by changing the voltage applied to each of the rods and monitoring the current after the bending quadrupole in order to maintain the highest transmission.
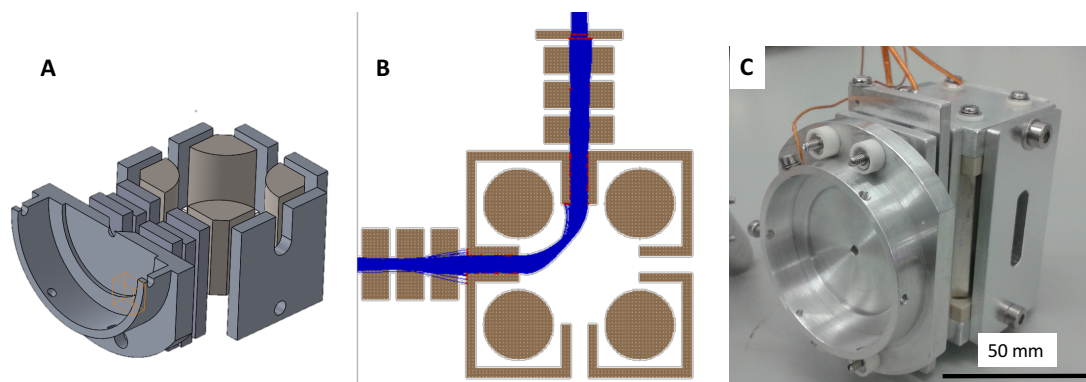
Figure 3.9 (A) 3D CAD section, (B) SIMION simulation and (C) photograph of the bending quadrupole assembly.

Ions directed towards the electron multiplier are measured as a function of the mass spectrometer scan line values (DC and RF voltages) applied to the mass-filtering quadrupole in order to create a mass spectrum. Ions which have been sent to the electron multiplier are lost and do not continue to a deposition stage. Ions directed towards the UHV stage are sent along hexapole B after which they are directed towards the soft-landing stage and subsequent analysis by *in-situ* STM. Ions directed towards the HV stage are typically being used for deposition on surfaces that will be analysed *ex-situ*. This is because the HV deposition stage also incorporates a quick access load lock in order to remove and insert samples relatively quickly. These types of sample may be analysed by X-Ray photoemission spectroscopy (XPS), Atomic force microscopy (AFM), Raman spectroscopy, transmission electron microscopy (TEM) or a number of other techniques. This versatility allows for a wider range of samples to be prepared and a greater number of analytical methods to be utilised.

3.1.10 Computer control system

The numerous electrical components, voltages and lenses that compose SEISMIC are all controlled by a computer interface which has been built with the LabVIEW 8 software (National Instruments Incorporated). The software is capable of applying voltages, measuring currents and controlling all components of the instrument. This software has been adapted from a similar piece of software kindly provided by

Professor Stephan Rauschenbach. The software interfaces with a number of digital to analogues converters (DAC) connected to the electrostatic lens supplies, the mass-selecting quadrupole control box and Keithley 617 electrometers. There are over 50 electrical voltages that can be applied to the system and nine current read-out locations. This software gives a user-friendly interface for optimising voltages and currents for all of the components in SEISMIC.

3.1.11 Operating procedure

In order to prepare a beam of ions for deposition several steps are taken. First the spray is created at the electrospray interface by applying a high voltage between the emitter capillary and the entrance capillary as the analyte solution is pumped through the tubing. The high voltage and solution flow rate can be tuned in order to achieve a stable spray with an optimum current which is measured on the ion funnel in collection mode (DC voltage of -100 V in order to collect all transmitted ions). Typical electrospray voltages are 1-3 kV and typical flow rates are 50-500 µl/hr. Once a stable spray has been achieved, a series of optimisation steps occurs in order to maximise the current of the ion beam.

Firstly, the ion funnel RF voltage amplitude and DC voltage gradient are varied while monitoring the current on the hexapole rods which are not in operation at this stage but set to a negative voltage (-50 V) in order to collect all transmitted ions. Typical values for high transmission are 100 V for the RF voltage and a DC gradient of 50 V. The next optimisation concerns the DC offset of hexapole A and its RF voltage. Again this is optimised by using the LabVIEW software to increase the applied values until an optimum current is achieved which in this instance is measured on the gate valve after the quadrupole. The next optimisation is that of the mass-filtering quadrupole. When experiments are run it is usual for the compound of interest to be of a known mass so this can be used as a starting point for the optimisation of the mass-filtering quadrupole. The first step is to increase the DC voltage of the quadrupole form 0-10 V (which corresponds to a mass scan in the range of 20-4000 m/z) and measure the current on the electron multiplier. In this way a mass spectrum is obtained. In the case where only a single peak is seen (or a series of peaks which can all be attributed to a single species, such as multiple charge states, sodium or potassium adducts, dimer or trimers of the species, etc.) the quadrupole is set to RF only mode and a wide transmission window is used to achieve maximum current. In the case where multiple

peaks are seen, corresponding to a number of different species, a voltage is applied to the quadrupole rods which corresponds to the filtering of only the mass of the analyte of interest. In this way the current dramatically drops (from 10^2 pA to 1 pA) but one can be sure that only the molecule of interest is being transmitted. The beam is focussed by the lenses on the thin gate valve, by using the mapping procedure with the steering voltages described before. After this point the ions enter the bending quadrupole where the voltages are optimised for either HV or UHV deposition, the two scenarios being identical in terms of optimisation. Again the voltages on the rods are varied using the LabVIEW interface and the current is monitored on the lenses on the exit of the bending quadrupole set to collection mode. After this stage, for HV deposition, the beam is sent through a set of lenses on the HV sample holder where the final current is measured. The amount of material deposited on the surface is measured in pAh (current of beam in pA multiplied by the deposition time in hours). For UHV deposition, several further optimisations steps must be completed prior to the final deposition. After exiting the bending quadrupole, the ions enter hexapole B that must be optimised by measuring the current on the UHV sample as the RF voltage and offset voltage are changed. This procedure is repeated for the intermediate lenses and steering lenses. The final optimisation is completed using the lenses attached to the manipulator head where the landing energy of the ions is defined by application of a retarding/accelerating potential to the sample. The amount of material is measured in the same way as was described for HV deposition. After deposition, the sample can be transferred without breaking the vacuum via the manipulator and wobble sticks to the SPECS Aarhus 150 VT-STM for characterisation.

3.2 Molecular Spray system

3.2.1 Introduction

A complementary electrospray deposition system has also been used in this work. The commercially available Molecular Spray[120] is a compact series of differentially pumped chambers connected to an electrospray source; a schematic can be seen in Figure 3.10. This can be mounted onto a UHV chamber and used to deposit molecules. The Molecular Spray system has been shown to be capable of depositing a variety of large thermolabile molecules including molecular magnets, porphyrin rings, and polymers[17,50,121–123].
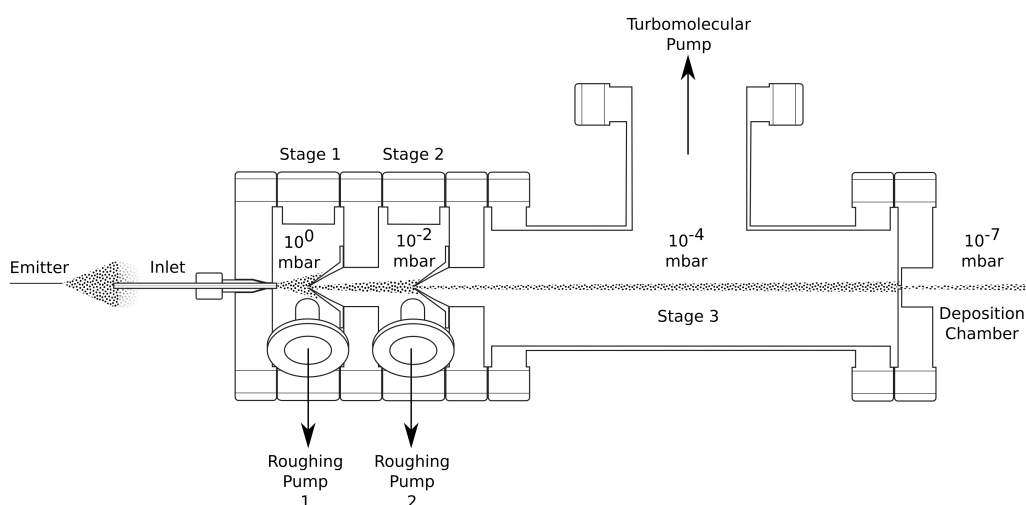
Figure 3.10 Schematic drawing of the Molecular Spray system[124]. The system used in this work had an additional differentially pumped stage before the deposition chamber.

The Molecular Spray system has many advantages and disadvantages when compared with SEISMIC as it is significantly easier to use and can in principle deposit molecules of any mass, so long as they are soluble and can be formed into an electrospray. This is due to the lack of any form of mass selection or ion optics and therefore to the absence of any condition on the m/z ratio of the analyte of interest. The lack of ion optics also means the only optimisations that are required to be carried out are those at the electrospray ionisation interface meaning experiments can be conducted much more quickly. Further, due to the compact nature of the system it can easily be moved from chamber to chamber, allowing for preparation of samples at a number of different facilities with varying analytical capabilities (such as synchrotron sources[125]). The main drawbacks are the lack of mass filtering and in-line beam analysis meaning the

62

absence of any knowledge about the composition of the beam that is deposited on the surface. This includes full ignorance of any damage potentially occurring to the analyte molecules between the electrospray process and the surface landing; of the degree of desolvation and/or aggregation of the molecules of interest; of the charging status, including the possible presence of many neutral species (aggravated by the direct line of sight and the short distance between the electrospray ionisation interface and the surface). As a matter of fact, the beam that reaches the surface is probably a very complex mixture of analyte ions, solvent molecules, analyte and solvent mixed clusters with various degrees of ionisation and both charged and neutral microdroplets. Finally, the more compact nature of the Molecular Spray system means it is composed of fewer differentially pumped chambers resulting in a base pressure during deposition which is higher than with SEISMIC (10^{-7} mbar for the Molecular Spray versus 10^{-9} mbar for SEISMIC). In this work, the Molecular Spray system has been used to deposit conjugated polymers on atomically clean and flat metallic surfaces and to characterise them by using STM. Conjugated polymers are unsuitable for use on SEISMIC mainly due to their mass being outside the transmission range of the mass-filtering device.

3.2.2 Electrospray ionisation interface

The electrospray ionisation interface used on the Molecular Spray system is very similar to that used on SEISMIC. The T piece, tubing and stainless steel emitter are all identical (see section 3.1.3), the main difference being the inlet capillary. The Molecular Spray system has a conventional flat geometry capillary (seen in Figure 3.10) but with a much smaller diameter of 0.5 mm. In fact, this is the only way to combine a compact design and small size of the setup with the requirement to achieve HV in the deposition stage and to avoid the need for large pumps in the first stages of the source. However, this can also compromise an efficient desolvation of the analyte molecules, as already noted in the previous section.

3.2.3 Differential pumping

The Molecular Spray system consists of four differentially pumped chambers that are separated from those either side of it by small holes with a diameter of 0.5 mm. The first chamber is pumped by an Agilent scroll pump (pumping speed = 1.65 l/s) and achieves a pressure of approximately 0.8 mbar. The second chamber is pumped by an Agilent scroll pump (pumping speed = 1.65 l/s) and achieves a pressure of 10^{-2} mbar. The third chamber is pumped by a Pfeiffer 70 l/s turbomolecular pump and achieves

a pressure of 10^{-5} mbar. Finally, the fourth chamber is pumped by a Pfeiffer 70 l/s turbomolecular pump and achieves a pressure of 10^{-7} mbar. All of the quoted pressures are measured before the electrospray deposition has started. Once the electrospray process begins, the pressures increase reaching a typical pressure of 10^{-6} mbar in the fourth chamber, which gives a pressure of approximately 10^{-7} mbar in the preparation chamber where the deposition sample is kept.

3.2.4 Operating procedure

The operating procedure for any experiment carried out using the Molecular Spray system follows the same basic set of instructions. The molecule of interest is tested in a number of solvents to determine its compatibility and solubility with the solvents typically used for electrospray ionisation measurements. Once this has been determined a solution of approximately 0.1 mg/ml is made (this concentration has been chosen as in previous published work[17,123,125] it has been shown to give a good surface coverage for a range of molecules in a reasonable deposition time of up to 30 minutes). Once the solution has been prepared, it is placed into the glass syringe which is subsequently placed into a syringe pump where the injection speed can be accurately controlled. Typical injection speeds are around 0.1-2.0 ml/min although this is often adjusted depending on a number of factors such as solvent and concentration. A high voltage is applied to the solution which is typically in the range of 1-3 kV with the same factors effecting this as those which dictate the injection speed. The position of the emitter relative to the inlet capillary is optimised by both monitoring the pressure rise in the preparation chamber and also by measuring the current on the sample (typical target values of 10^{-5} mbar and 10^{2} pA, respectively) . A three axis movement is used to attain the highest current possible. After this has been achieved, the deposition is left for an amount of time dependent on the desired surface coverage (typically between 5 and 30 minutes). After deposition, the gate valve between the Molecular Spray system and the preparation chamber is closed and the pressure is allowed to revert to the base value of around 10^{-10} mbar. The sample is then transferred *in-situ* to the STM chamber where imaging can be performed.

This procedure has been used for all of the results in chapters 5, 6 and 7. Any variations to this procedure or more specific details are given in the corresponding chapters.

3.3 Sample preparation

3.3.1 Surfaces – Au(111)

The Au(111)/mica samples were supplied by Georg Albert PVD in slides of 20 mm × 120 mm. Au(111) samples are cut to approximately 10 mm × 10 mm and attached to a SPECS sample plate through spot welding with tantalum foil.

3.3.2 Surfaces – Ag(111)

The Ag(111)/mica samples were supplied by Georg Albert PVD in slides of 20 mm × 120 mm. Ag(111) samples are cut to approximately 10 mm × 10 mm and attached to a SPECS sample plate through spot welding with tantalum foil.

3.3.3 Surfaces – Cu(110)

Cu(110) single crystals were purchased from SPL and in a top hat shape, with the polished Cu(110) surface comprising of a circle of 5 mm in diameter. The Cu(110) crystal was mounted onto SPECS sample plate using a tantalum ring which was spot welded to the plate.

3.3.4 Surface preparation

All surfaces used in this thesis (Au (111), Ag (111) and Cu (110)) were prepared in an identical manner. Repeated cycles of Ar^+ sputtering at 1 keV at a current of 4 μA/cm^2 for 15 minutes were performed followed by subsequent annealing to 500 °C for 20 minutes and checked with *in-situ* STM for cleanliness. The process was repeated if the surface was found to be unclean.

3.3.5 Analyte solution preparation

Table 3.2 outlines each analyte used, the solvent used to dissolve it in and the concentration of the solution used. The supplier is also indicated for each compound.

Table 3.2 Overview of all compounds used in this thesis.

Compound	Concentration	Solvent	Supplier	Deposition method
Rhodamine B	$10^{-4} - 10^{-5}$ M	Methanol	Sigma Aldrich	SEISMIC
Bovine Serum Albumin	10^{-6} M	Methanol	Sigma Aldrich	SEISMIC
Polyethylene glycol	0.1 g/ml	Methanol	Sigma Aldrich	SEISMIC
Nickel octaethyl porphyrin	0.1 g/ml	Methanol	Porphychem	SEISMIC
Zinc phthalocyanine	0.08 g/ml	Methanol	Porphychem	SEISMIC
poly (C_{14}DPPF-F)	0.04 g/ml	Toluene:Methanol (4:1)	Hugo Bronstein	Molecular Spray
Dimer of C_8C_6DPPT-P	0.05 mg/ml	Toluene:Methanol (4:1)	Hugo Bronstein	Molecular Spray
Tetramer of C_8C_6DPPT-P	0.05 mg/ml	Toluene:Methanol (4:1)	Hugo Bronstein	Molecular Spray
Hexamer of C_8C_6DPPT-P	0.05 mg/ml	Toluene:Methanol (4:1)	Hugo Bronstein	Molecular Spray
poly (C_8C_6DPPT-P)	0.06 mg/ml	Toluene:Methanol (4:1)	Hugo Bronstein	Molecular Spray
P3HT	0.07 mg/ml	Toluene:Methanol (4:1)	Sigma Aldrich	Molecular Spray
pBTTT	0.04 mg/ml	Toluene:Methanol (4:1)	Iain McCulloch	Molecular Spray
poly (C_{14}DPP-T)	0.05 mg/ml	Toluene:Methanol (4:1)	Hugo Bronstein	Molecular Spray
poly (C_{16}DPPP-P)	0.05 mg/ml	Toluene:Methanol (4:1)	Hugo Bronstein	Molecular Spray
KF829	0.06 mg/ml	Toluene:Methanol (4:1)	Hugo Bronstein	Molecular Spray

4 Development of a high flux ion source for controllable landing of complex molecules - SEISMIC

4.1 Performance of SEISMIC

4.1.1 Introduction

In this chapter the performance of each of the components of SEISMIC (which have been described in Chapter 3) has been evaluated. We demonstrate the capability of each component to transfer a high flux ion beam through the differentially pumped chambers of SEISMIC. In addition to this, we also demonstrate the soft landing capability of a test molecule to ensure that deposition is working effectively.

4.1.2 Electrospray ionisation interface

The electrospray ionisation interface consists of the inlet capillary and the solution delivery system. The solution delivery system used is a standard syringe pump and syringe set up (as outlined in Chapter 3), the emitter used is also a standard commercial emitter. However, the inlet capillary and its geometry has been specifically chosen for the highest possible ion transmission. The electrospray ionisation interface is the single most important component of SEISMIC in terms of minimising ion losses. It has been shown that the vast majority of losses occur at this stage due to the geometry of the inlet capillary and as such it was important to ensure the most effective inlet was chosen. The inlet capillary used in this work has been taken from a design from Stephan Rauschenbach and co-workers[115] which has shown very good performance in an instrument which is very similar to SEISMIC. We have tested the capillary in order to benchmark it against the previous published results and to ensure it works well with our interface design. In all of these benchmarks the key characteristics we are looking to optimise is the absolute ion current as well as the transmitted ion percentage.

The transmitted ion current was studied as a function of the temperature of the inlet capillary. It has been shown that an increased inlet capillary temperature can lead to better desolvation of solvent clusters and lead to a higher ion current[116]. In Figure 4.1 we show the measured ion current as a function of the inlet capillary temperature for a solution of Rhodamine B dissolved to a concentration of 10^{-4} M in methanol inside the first differentially pumped chamber (pressure = 0.8 mbar). We see that there is an increase in current from room temperature up to around 100 °C. After this temperature the increase slows and eventually plateaus. We suggest the reason for this plateau may

be due to a sufficiently high temperature being reached in order to desolvate all of the ions present in the capillary achieving 100% transmission. This was confirmed by measuring the total ion current exiting the emitter on a flat plate which was measured to be 5.3 nA, indicating that the plateau occurs at unity transmission. This is in agreement with what has been seen previously by Rauschenbach and co-workers.
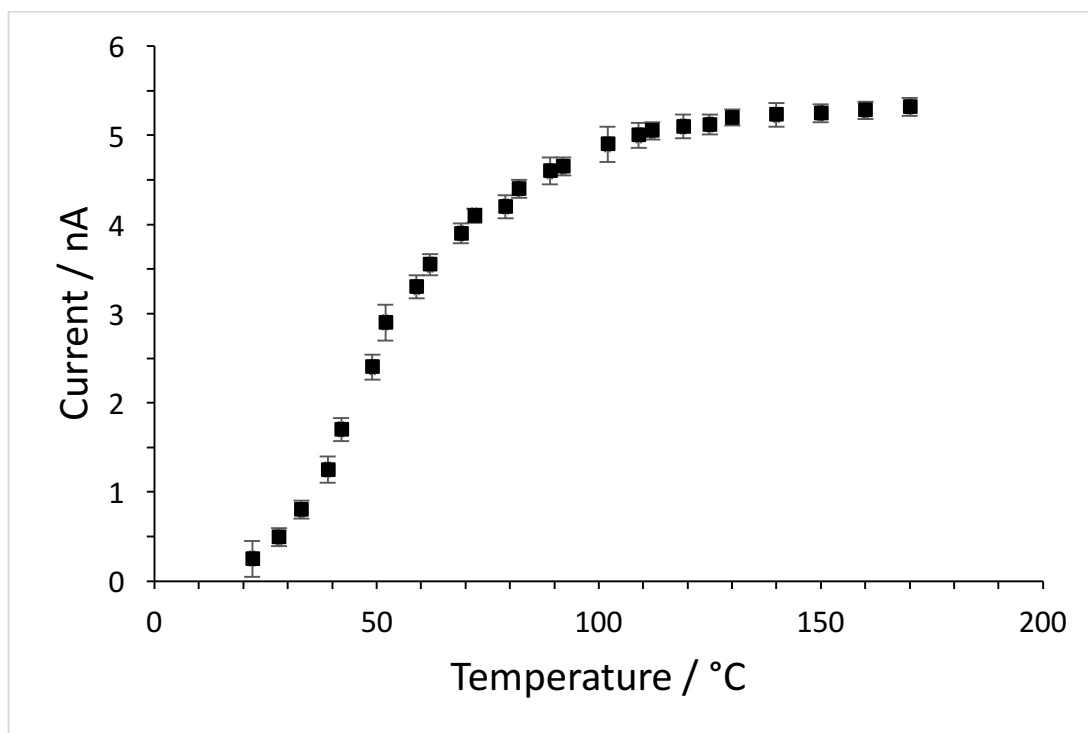
Figure 4.1 Graph showing the dependence of the transmitted current on the temperature of the inlet capillary.

The second transmission test of the inlet capillary was completed by varying the high voltage applied to the analyte solution. We see in Figure 4.2 the that as the high voltage is increased past a threshold value (around 1.5 kV) the current sharply increases and then remains at a constant value as the voltage is increased further. The overall ion current here is lower than in the temperature test as the experiment was completed with an inlet capillary temperature of 70 °C. A visual inspection of the exiting electrospray also confirmed that as the voltage was increased past the 1.5 kV threshold the spray changed from droplets to a more well defined spray.
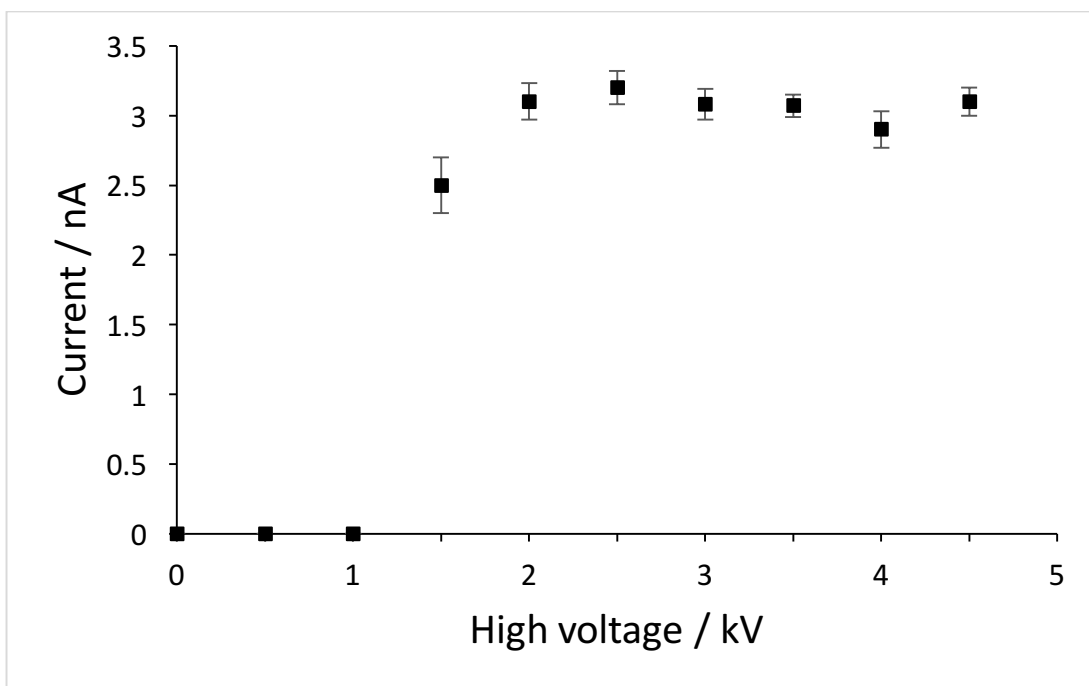
Figure 4.2 Graph showing the transmitted current through the inlet capillary as a function of the high voltage applied to the analyte solution.

In summary, both of these results show comparable transmission values and absolute current levels to the previously published results by Rauschenbach and co-workers. As such, we believe the funnel capillary is working as intended and provides an excellent starting point for SEISMIC. We have also shown that the electrospray ionisation interface we have built can reach sufficiently high inlet capillary temperatures to achieve unity transmission.

4.1.3 Ion funnel

The ion funnel design (section 3.1.4) has been tested for a range of molecules in order to characterise its performance. The ion funnel transmission has been measured as a function of pressure, temperature, RF voltage and DC gradient. Not only do these tests provide valuable information as to the effectiveness of the design of the component, they also provide a good basis for further experiments with molecules which may behave in a similar fashion giving a base line set of values which can be used as starting conditions.

The first set of results show the ion current which has been transmitted as a function of the pressure inside the ion funnel chamber. A solution of Rhodamine B in methanol (10^{-5} M) was used with a high voltage of 2.5 kV and an inlet capillary temperature of 100 °C. A gas valve was attached to the ion funnel chamber in order to be able to

manually vary the pressure inside the chamber. A graph of the results is seen in Figure 4.3.
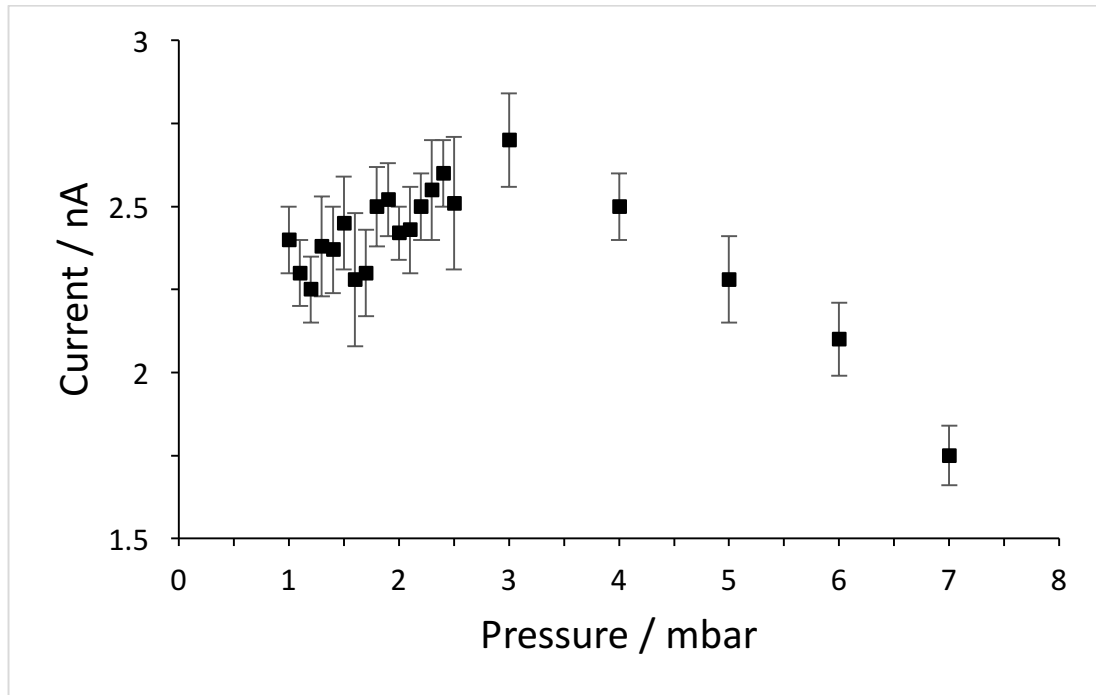
Figure 4.3 Graph showing the dependence of the transmitted current through the ion funnel as a function of the pressure within the ion funnel chamber.

We see that from 0.8-3 mbar the current measured at the final plate of the ion funnel increases by just over 20%. After this initial increase the current then drops by over 30% in the pressure range 3-7 mbar. The reason for the initial current increase can be explained by considering that the increased number of background gas molecules present in the chamber result in a greater number of collisions with the ion beam. This means the beam is thermally cooled faster and can be transmitted and focussed more easily[118]. However, increasing the pressure past a certain threshold (in this case 3 mbar) causes the current to drop significantly. A reason for this may be due to the increased amount of background gas lowering the overall pressure gradient, creating less of a pull for ions travelling through the funnel. Further, ions travel through the funnel from left to right, the gas was leaked in from above this path and the pumped is situated below the path of ions. It may be that the flow of leaked gas from the inlet to where it is removed by the pump caused ions to be dragged out of the ion funnel path and to not be transmitted through. From this experiment the ideal pressure range (2-3 mbar) was found and used for subsequent experiments optimising the voltages applied to the ion funnel. However, by increasing the pressure in the ion funnel to 2-3

mbar the pressure further along the differentially pumped system also significantly increased, therefore it was decided to keep the ion funnel at the lower pressure of 0.8 mbar, sacrificing some ion transmission so that the final deposition pressure could be maintained at a lower value.

As noted in the previous chapter, the pseudo potential which is created in order to control the path of ions through the ion funnel is generated by the RF voltage which is applied to the ring electrodes. The peak-to-peak voltage of this wave can be changed during an experiment. The effect of the peak-to-peak voltage has been studied in terms of its effect on the overall transmission of the ion funnel by measuring the transmitted ion current.

The peak-to-peak voltage was measured as a function of the total ion current exiting the ion funnel, the results can be seen in Figure 4.4. Two molecules of different molecular weights and number of charge states were chosen so as to explore the effects of m/z on the transmission of the ion funnel. The peak-to-peak voltage was increased from 0-200 V and then decreased from 200-0 V whilst the current was being measured (indicated by the key in Figure 4.4). Good overlap of these data points ensured that there was no hysteresis in the measurements. For both rhodamine B (RhB) (m/z =440) and bovine serum albumin (BSA) (m/z = 1000-2000) the same shape is seen for the current as a function of increasing peak-to-peak voltage. That is, from 0-75 V the current increases linearly and then from 75-200 V the current plateaus. This plateau is the expected shape for an ion funnel[77,118] and shows that our ion funnel is effectively transporting ions in the mass range tested. The plateau represents a transmission of 100% of the ions which have entered the device. This was verified by setting the ion funnel into collection mode (-100 V DC voltage applied to the ring electrodes, with peak-to-peak voltage set to 0 V) and measuring the total current entering the ion funnel and comparing this to the plateau value. For all the molecules tested these values gave a 100% transmission. No dependence on m/z value was seen as is consistent with this design of ion funnel[77,118].
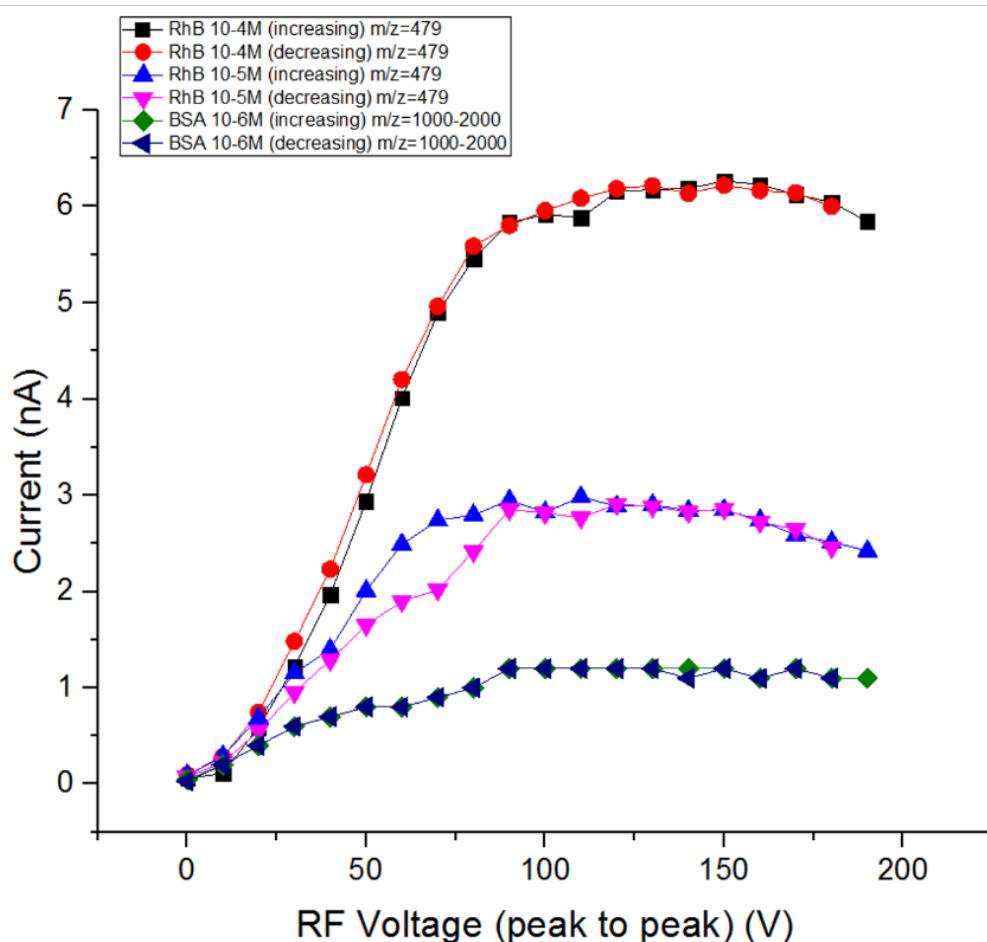
Figure 4.4 Graph showing the dependence of transmitted ion current as a function of the peak-to-peak RF voltage for rhodamine B and BSA.

The DC gradient along the ion funnel is also expected to play a critical role in dragging ions from the entrance to the exit of the ion funnel. The gradient is defined as the voltage applied to the final electrode minus the voltage applied to the first electrode and ranges from 0-130 V. This has been varied and the current measured at the exit of the ion funnel the results of which can be seen in Figure 4.5 (a RhB solution of 10^{-5} M in methanol was used). Across this range of values, the current increases by approximately 10% from 0-20 V and remains constant from 20-140 V. From these results it appears that the DC gradient does not make a significant difference to the transmitted ion current, this may be because the pressure gradient is playing a more significant role and the DC gradient's effect is masked by this.
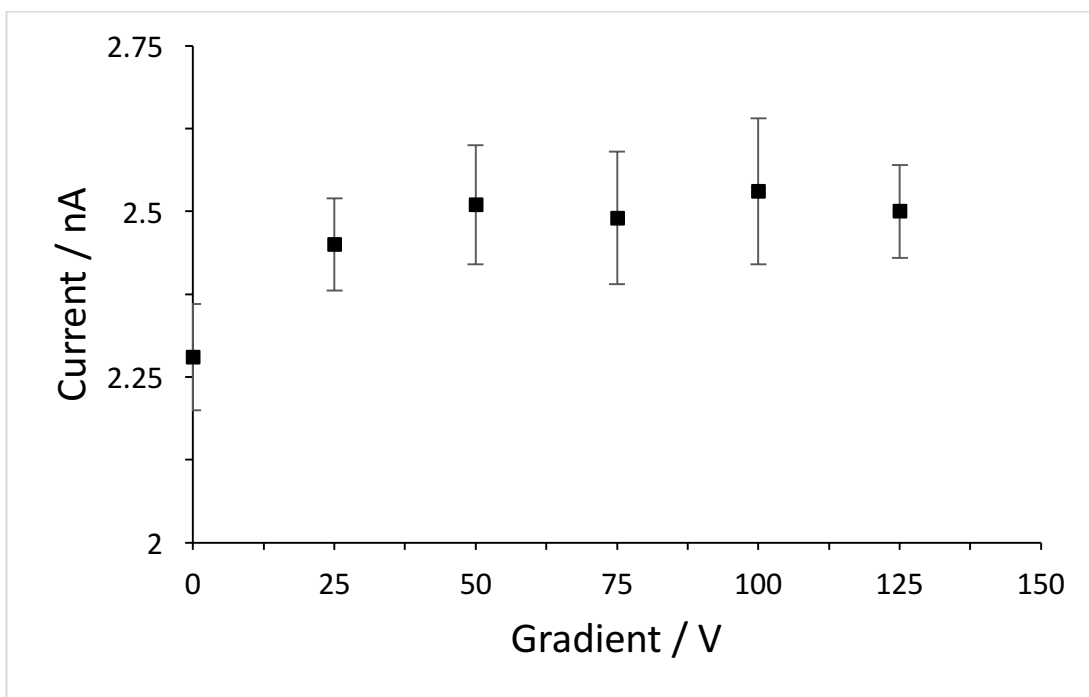
Figure 4.5 Graph showing the transmitted current as a function of the DC gradient applied to the ion funnel.

The ion funnel design presented in Chapter 3 and tested here has shown very good transmission values of up to unity transmission. A wide m/z range of molecules have also been shown to be transmitted with no issues. This ion funnel design represents a robust and easy to use piece of apparatus that can be easily fitted, removed and cleaned in SEISMIC.

4.1.4   Hexapole ion guide

The unique hexapole design outlined in section 3.1.5 has here been tested in order to characterise the effectiveness of transmission. The hexapole has also been tested in order to characterise the performance of both the differential pumping seal and the RF peak-to-peak voltage.

In Figure 4.6 we see results for the transmitted current from an ion beam of RhB (dissolved in methanol to a concentration of 10^{-5} M) ions as a function of the peak-to-peak voltage applied to the hexapole rods. We see that as the voltage is increased the transmitted current also increases across the full range from 0-200 V after passing a threshold voltage of 100 V. This shape of transmission is typical of multipole ion guides[77] and shows the hexapole is working effectively. Moreover, the absolute transmitted current value of 1.2 nA is very high (compared to similar apparatus[14,19]) and demonstrates that the hexapole's multistage differentially sealed design can result

in higher ion currents. The value of 1.2 nA is however significantly lower than that measured at the end of the ion funnel (approximately 2.5 nA for the same solution). This means that some losses have occurred either as the beam passes through the exit of the ion funnel and enters the hexapole or along the length of the hexapole. By setting the hexapole into collection mode (-100 V DC applied to the rods and the peak-to-peak voltage set to 0 V) it was possible to confirm that only 1.2 nA of current arrived into the hexapole chamber. We can therefore conclude that the hexapole is transmitting all of the ions which enter but that a significant number are lost at the interface between the ion funnel and hexapole components.
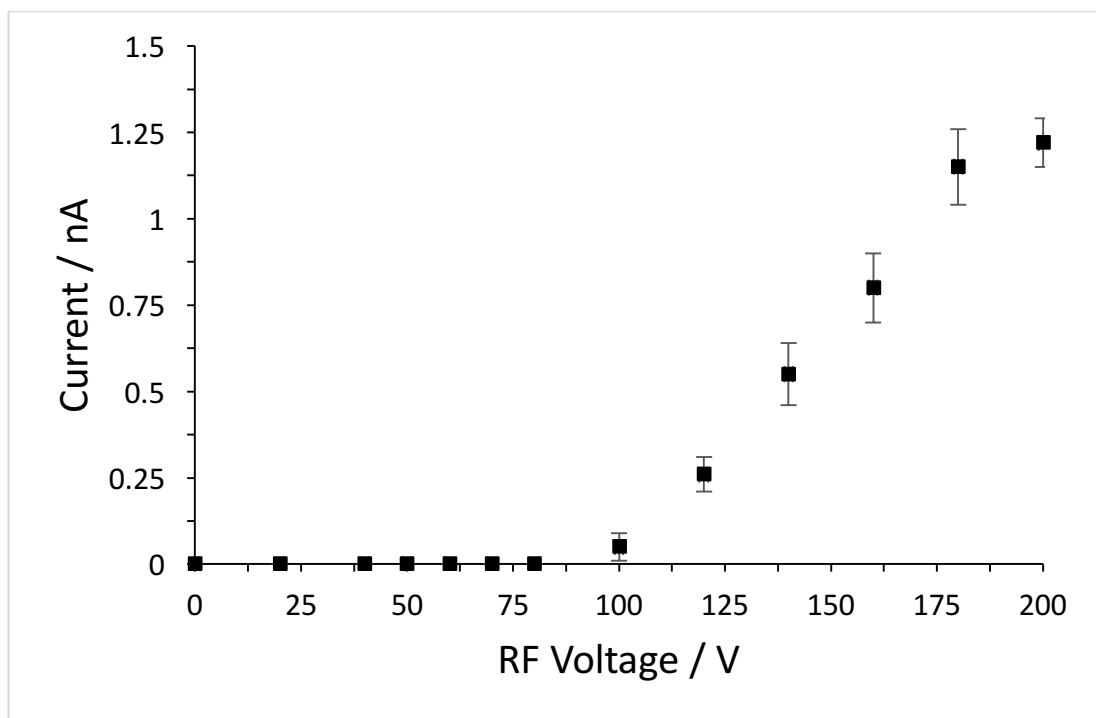
Figure 4.6 Graph showing the transmitted current through the hexapole as a function of the RF voltage applied.

The differential seal system has been shown to work well here. The first stage of the hexapole is typically at a value of 0.2 mbar whilst the second stage is at 2×10^{-2} mbar and the third (which resides inside the next chamber) is at 2×10^{-5} mbar. Considering the significant losses which have occurred at the interface between the ion funnel and hexapole (50% loss), the ability to pass ions through several differentially pumped sections without incurring more interfacial losses is extremely beneficial. For example, if the same losses were incurred as was seen at the ion funnel-hexapole interface across the two interfaces which are mitigated by the hexapole design we

would have a current of 0.3 nA as opposed to the 1.2 nA which is achieved by this design.

Although some losses have occurred in the transition from ion funnel to hexapole the absolute current is still very high when compared to the same stage in similar instruments[14–16]. The differential seal has also allowed for the instrument to be made more compact and to achieve a significant pressure drop across a very small volume. In this way the final pressure of the deposition stage has also been able to be lowered with the need for fewer differentially pumped components limiting the losses that may occur with the inclusion of these.

4.1.5 *Mass-filtering quadrupole*

The mass-filtering quadrupole is a commercially available piece of apparatus which has been purchased from Extrel. In this section the quadrupole has been tested for a range of compounds. The electronics supplied with the mass-filtering quadrupole can be controlled though LabVIEW software in order to control: the DC offset of the quadrupole; the resolving power; the mass scan range; and setting the quadrupole in RF only mode. For our purposes most of these values are not modified. What is important to test is the accurate calibration of the mass range. To do this we have taken mass spectra for a number of compounds and used these in order to ensure that the quadrupole is well calibrated.

In Figure 4.7 we see mass spectra for RhB, nickel octaethyl porphyrin (NiOEP), and a zinc phthalocyanine. It has been possible to obtain a mass spectrum for each of these species which match with the expected values. The resolution of the instrument can be increased in order to see isotopic distribution patterns as can be seen for rhodamine B (Figure 4.7A) and NiOEP (Figure 4.7B). However, increasing the resolution of the spectrum results in a significantly lower transmitted current (1 pA compared with up to 500 pA in some instances) and is therefore only suitable for analysis and not a mode of operation when attempting to prepare a sample with SEISMIC. For each of the molecules presented here the m/z value matches with what is expected for an electrosprayed sample run in positive ion mode. For rhodamine B the predicted value is 440 m/z and we see a peak at 440 (as well as 441 and 442 representing the isotopic distribution pattern); for NiOEP the predicted value is 592 and again we see an isotopic distribution pattern which matches with this; for the zinc phthalocyanine we expect to

see a peak at 1088 m/z for a singly charged molecule and this is indeed what is seen. The other minor peak seen in the zinc phthalocyanine spectrum at 1015 m/z is likely due to the loss of a silyl (SiMe$_3$) group which has either been lost in the synthetic procedure or as a result of the electrospray process. The peak at around 1150 m/z is expected to be the zinc phthalocyanine plus a solvent adduct.
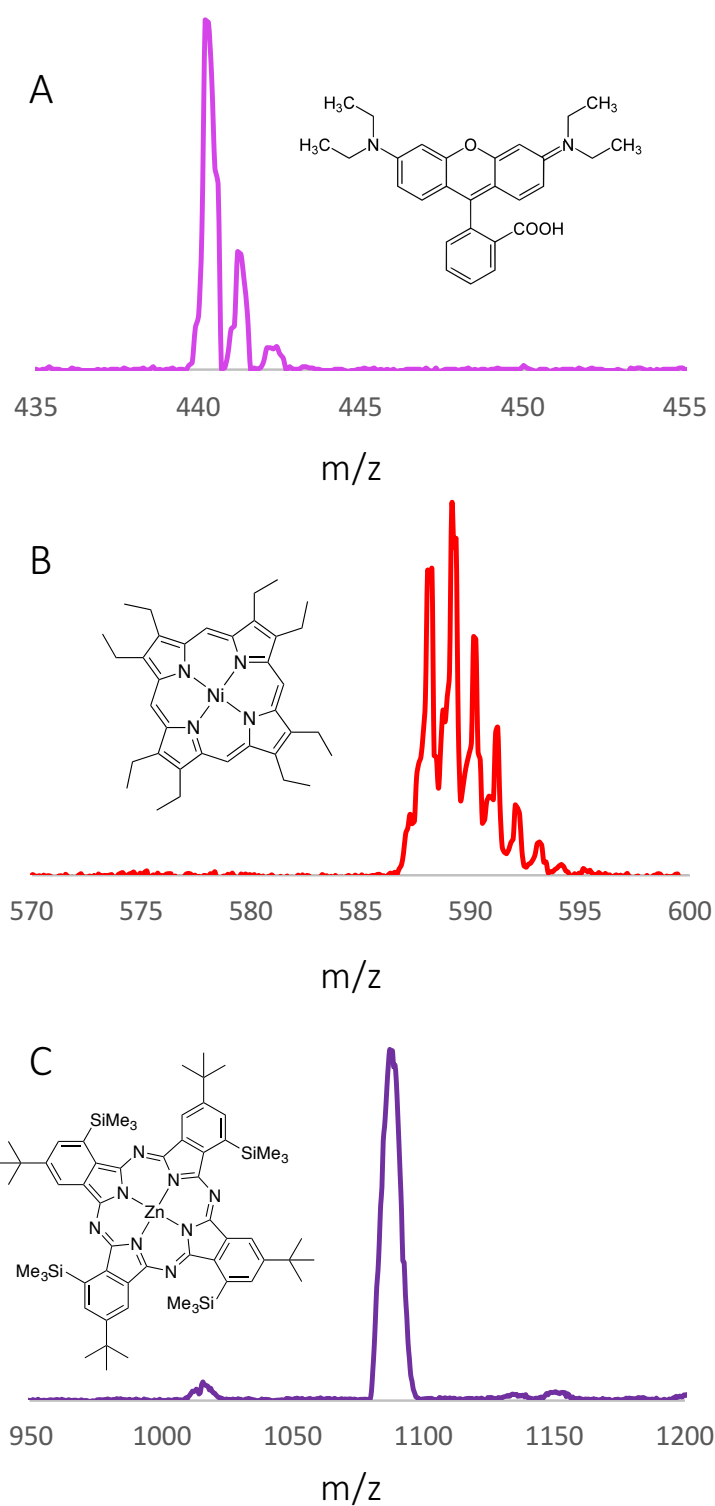
Figure 4.7 Mass spectra and corresponding molecular structures. (A) Mass spectrum of rhodamine B and molecular structure. (B) Mass spectrum of nickel octaethyl porphyrin and corresponding molecular structure. (C) Mass spectrum of a zinc phthalocyanine and the corresponding molecular structure.

Shown in Figure 4.8 is a mass spectrum taken using SESIMIC of polyethylene glycol (PEG) where several peaks can be clearly identified corresponding to m/z values of: 313.5, 337.5, 359.5, 381.5, 403.5, and 425.5. Also displayed on the figure is the chemical structure of polyethylene glycol. The repeat unit of PEG is 44 g/mol and we see that there is a separation between each of the peaks of 22 m/z. This series of peaks represents a series of PEG polymers which are one repeat unit different in mass. Therefore, we can conclude that the PEG molecules are doubly charged. We also see a second series of peaks at m/z values of: 326, 348, 370, 392, and 414. Again, these peaks are separated by 22 m/z so represent a second series of polymer chains which are doubly charged, the difference in mass between these two series in an indication of polymers with different end groups present. For example, the mass difference of 13.5 m/z between the 313.5 m/z and 326 m/z could be indicative of the mass difference expected between a polymer chain terminated by an alcohol or a methyl ester (expected difference of 14 m/z). This result shows that the mass spectrometer capabilities of SEISMIC are working well and can help to identify charge states for larger molecules.
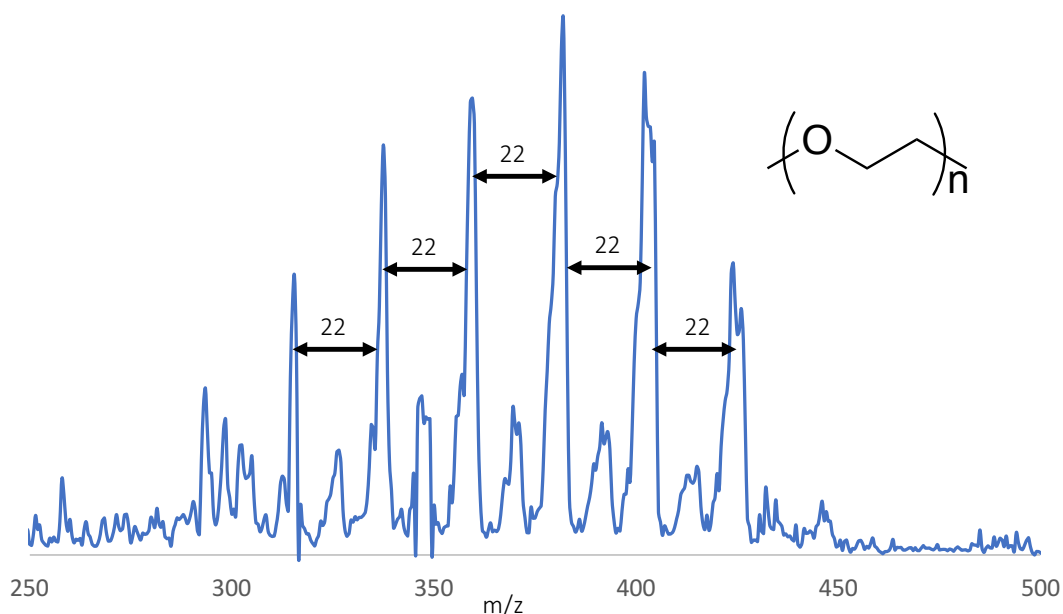
Figure 4.8 Mass spectrum and molecular structure of polyethylene glycol.

The mass-filtering quadrupole has been shown to be able to effectively generate spectra for a range of compounds with resolution high enough in some cases to be able to distinguish isotopic distribution patterns. Moreover, for the purposes of this

instrument the identification by means of mass or charge state for a number of molecules has been readily achieved. Transmitted currents of unfiltered ion beams can reach up to 500 pA and filtered ion currents of up to 200 pA have been achieved.

4.1.6 *Electrostatic lenses and minimum thickness gate valve*

After ions leave the mass-filtering quadrupole they must pass through a specially designed gate valve aided by an accelerating grid, a set of focussing lenses, and a set of steering lenses. The accelerating grid is typically biased to accelerate ions to 40 eV (applying a voltage of -40 V for a singly charged positive ion). The focussing lenses have been described in Chapter 3 as have the steering lenses and gate valve design. The effectiveness of the steering lenses can be seen in the heat map shown in Figure 4.9.
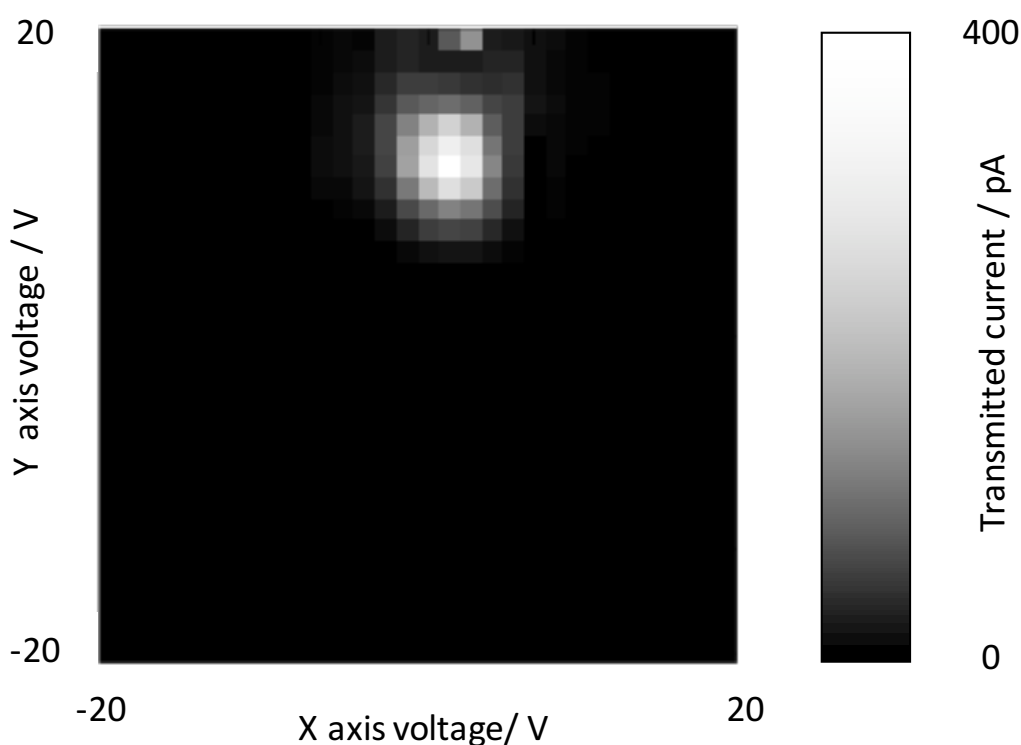
Figure 4.9 Heat map showing the transmitted current through the gate valve aperture as a function of the x and y steering voltages.

In this figure we see a bright spot which corresponds to the maximum transmitted ion beam (400 pA at the maximum). By applying a voltage to the 4 steering electrodes the beam can be directed through the 2 mm dimeter aperture in the gate valve. We see that

the hole is not centred at 0 V in either the x or y axis demonstrating the necessity of the steering electrodes to adjust for misaligned components within SEISMIC.

4.1.7 Bending quadrupole

The bending quadrupole is used to send ions along 1 of 3 different pathways: towards the ion detector; towards the HV deposition stage; or towards the UHV deposition stage. The transmission along each of these pathways has been measured. The effectiveness of the post bending anisotropic lenses have also been tested as a function of the transmitted current.

First we focus on the path which sends ions towards the electron multiplier. In this mode the bending quadrupole is switched off i.e. no voltage is applied to any of the electrodes. Ions pass through the bending quadrupole after exiting the mass selecting quadrupole and are accelerated towards the electron multiplier by a high voltage of the opposite polarity to the ions being detected (typically ±7-9 kV). This mode of operation is used exclusively for the collection of mass spectra and is an analysis tool (as has been discussed previously) the results of this were shown in the previous section.
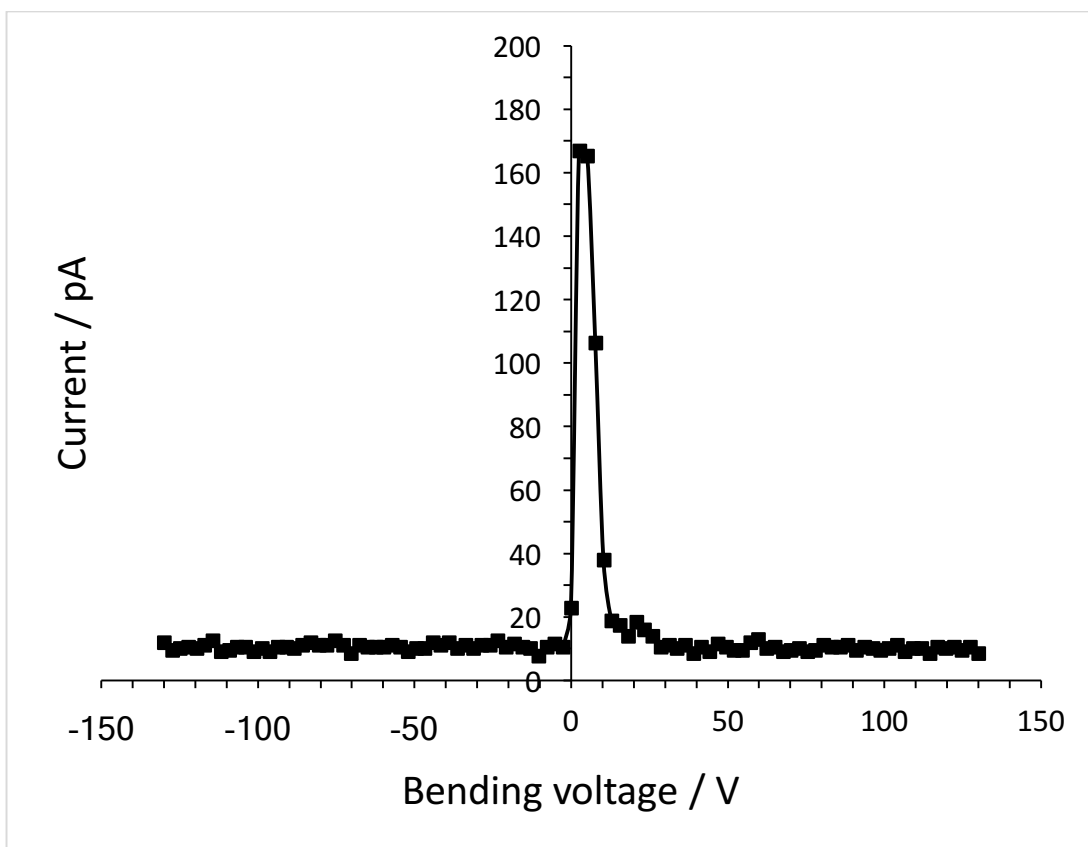
Figure 4.10 Graph showing the bending voltage required to send ions to the UHV deposition stage and the corresponding current.

The other two paths the ions can take through the bending quadrupole are towards the HV and UHV deposition stages. Both of these landing stages lie at 90° to the initial path of the ions, hence the need for the bending quadrupole. This was a deliberate design choice in order to avoid neutral molecules from landing on the substrate as neutral molecules cannot be discriminated through ion optics. In Figure 4.10 we see the transmitted current measured after the bending quadrupole as a function of the voltage applied to the bending quadrupole rods for the UHV bending directions. There is a sharp peak which corresponds to the voltage at which the ions are being deflected through the exit aperture of the bending quadrupole and onto the next stage of the instrument. The maximum achieved current after the bending quadrupole of approximately 400 pA represents a transmitted beam current of 80 % of that which leaves the quadrupole.

4.1.8   *Free flight and ion landing energy*

Not only is SEISMIC able to controllably deposit molecules which are otherwise incompatible with more conventional deposition techniques, there are additional

benefits which cannot be achieved through, for example, thermal sublimation. The one which is demonstrated in this section is the controlled landing energy of an ion beam.

After ions exit from the bending quadrupole and second hexapole there is a region of free flight. In this region ions are collimated and guided by two sets of electrostatic lenses. Typical lens voltages of -100 V are used to collimate and focus the beam onto the soft landing apparatus. A sample current of up to 300 pA can be achieved representing an overall transmission for the system of 12%. This value may appear low but it represents the ability to generate a monolayer coverage of molecules within a reasonable time frame (approximately 1 hour).

After ions have been detected at the landing stage an optimisation for deposition can occur. First, the exact energy of the ion beam is determined. The set of 3 lenses are used to collect the ion beam and focus it onto a small spot on the substrate. The exact spot size can be varied by changing the focusing voltage, a higher voltage giving a smaller spot size and a lower voltage giving a larger spot size. Below the lenses is the sample which can be biased using a voltage supply. By biasing the voltage of the sample from 30-40 V and measuring the current we obtain a graph as seen in Figure 4.11. Differentiation of this curve gives energy distribution of this beam. For this particular experiment the energy of the beam was 36.5 ± 1.2 eV. This relatively narrow beam energy is very important for the controlled landing of the sample as if the beam energy distribution is too wide then a large number of ions would be lost upon deceleration of the beam.
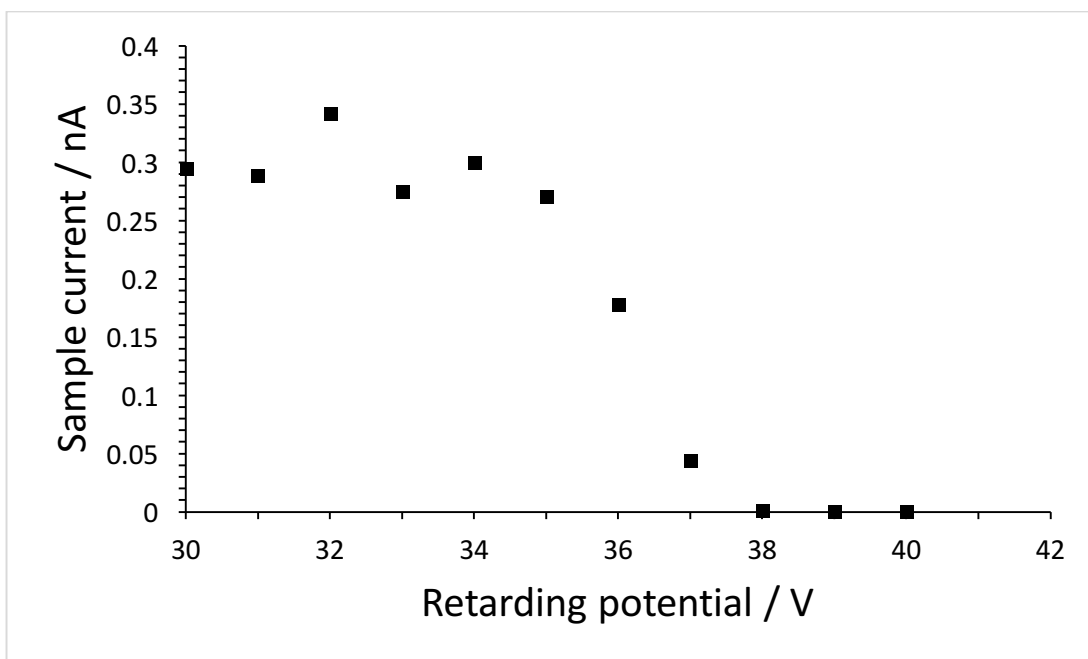
Figure 4.11 Graph showing the sample current as a function of the retarding potential applied to the sample.

Knowing the polarity of the ions and the average beam energy it is then possible to control whether ions arrive with more or less energy, i.e. whether they will be reactively or soft landed. In order to test this NiOEP was used as an example molecule, the results of which can be seen in the next section.

4.1.9   *Nickel octaethyl porphyrin – test molecule*

Nickel octaethyl porphyrin has been used as a test study molecule for the overall deposition performance of SEISMIC. The reasons for this decision are: the molecule has been previously studied with STM so results can be compared[126–128]; we found in tests that a high ion current could easily be achieved; the molecule is readily soluble in electrospray compatible solvents; no complications from fragmentation are likely to occur.
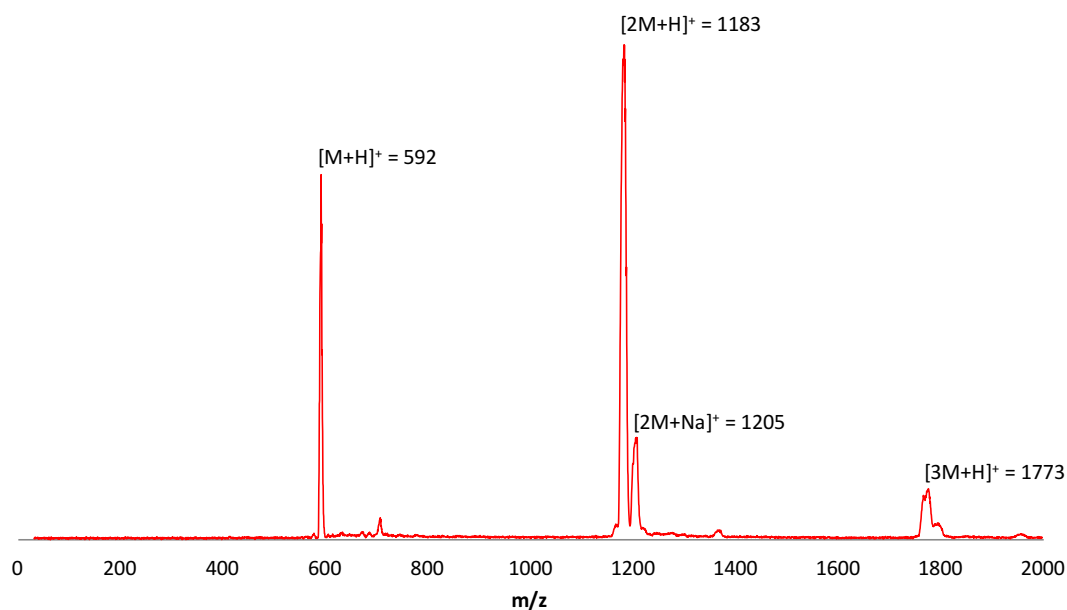
Figure 4.12 Wide range mass spectrum of NiOEP showing multiple peaks, corresponding to either monomer, dimer, or trimer clusters of the protonated or sodiated molecule.

Previously, in Figure 4.7B we saw the mass spectrum which corresponds to the NiOEP molecule and in Figure 4.12 we see a mass spectrum taken a cross a wider range of mass values that shows no fragmentation has occurred and that no other species are present in the ion beam. We do see clustering of porphyrin molecules which may be an indication of strong intermolecular bonds between molecules. After optimisations the current of NiOEP which arrived at the Au(111) surface was 200 pA. We can see the current arriving at the deposition stage as a function of the retarding potential in Figure 4.11 indicating a beam energy value of 36.5 ± 1.2 eV (calculated from the derivative of the curve seen in Figure 4.11). The molecule was deposited for 60 minutes in order to achieve a coverage of approximately 0.9 ML with a landing energy of 5 eV.

In Figure 4.13 we see an STM image of the NiOEP molecule prepared via SEISMIC and in the panel adjacent an STM image from previous literature result where the same molecule was prepared through thermal sublimation[126]. We note that the NiOEP which has been deposited via SEISMIC has self-assembled into ordered 2D domains with a unit cell size of 1.62 ± 0.10 nm, 2.74 ± 0.07 nm which is in excellent agreement with that seen for the previous literature results (1.65 and 2.76 ± 0.20 nm). We can therefore conclude that the controlled deposition of NiOEP has been achieved.

85

Unit cell: 1.62 ±0.20 nm, 2.74 ± 0.20 nm   Unit cell: 1.65 ± 0.20 nm, 2.76 ± 0.20 nm
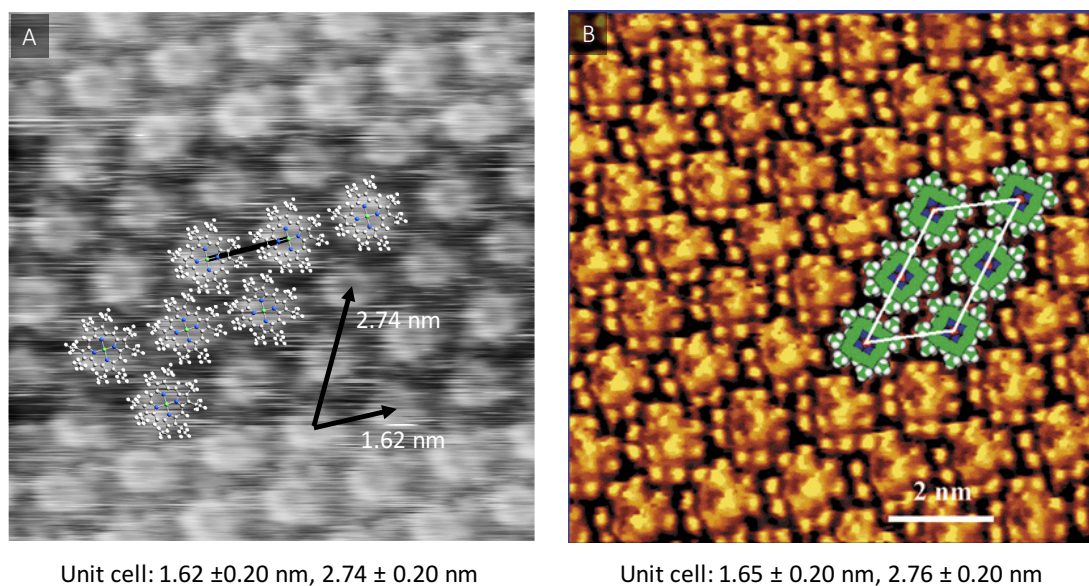
Figure 4.13 STM images of NiOEP on Au(111). (A) NiOEP monolayer on Au(111) deposited via SEISMIC. (B) NiOEP monolayer on Au(111) deposited via thermal sublimation, adapted from Hipps and co-workers[126]. V = -2.0V, I = 30 pA.

With the exact same setup NiOEP was also deposited at 40 eV in order to demonstrate the effects that different landing energies can have on the self-assembly of a molecule. In Figure 4.14A is a representative STM image of the Au(111) surface after having NiOEP deposited on it for 60 minutes at 200 pA and a landing energy of 40 eV. It is immediately obvious that the increased landing energy has had an effect on the self-assembly of the molecules. We see a very disordered assembly that does not resemble what was seen when deposited at 5 eV. The molecule appears to have been broken apart upon landing which has been seen previously for high energy landing of molecules on surfaces[56,129,130].

40 eV landing energy   5 eV landing energy
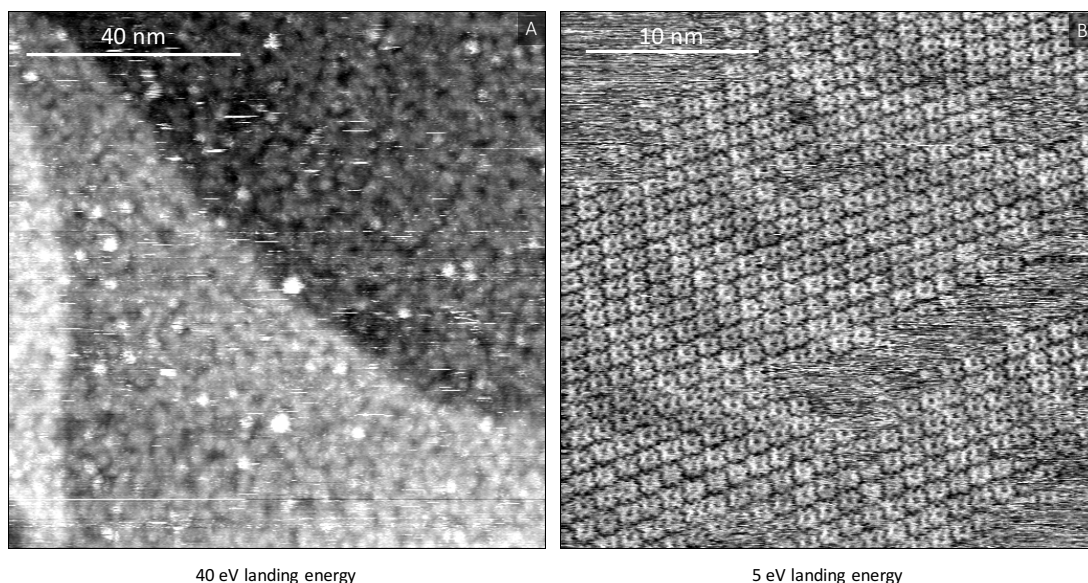
Figure 4.14 STM images of reactively and soft landed NiOEP on Au(111). (A) STM image of NiOEP deposited on Au(111) at a landing energy of 40 eV. (B) STM image of NiOEP deposited on Au(111) at a landing energy of 5 eV. V = -2.0V, I = 30 pA.

It should also be noted that in both of these cases the Au(111) surface was checked for cleanliness by STM prior to deposition therefore ensuring what is seen here is a result of the NiOEP ions.

4.2 Summary

Each component of SEISMIC has been tested and shown to work well with particular success with creating a high transmission hexapole ion guide and ion funnel. It has been shown that a test molecule – Nickel octaethyl porphyrin – can be deposited and imaged by STM using this apparatus. We have also shown the successful transmission of a number of larger molecules which are not compatible with thermal evaporation (BSA, PEG) which represents an excellent starting point for further experiments utilising SEISMIC's unique capabilities. From these results we can conclude that an overall transmission of up to 300 pA (12%) can be achieved representing a very high flux of ions. This high flux is advantageous for a number of reasons. Firstly, it allows experiments to be completed quickly. Secondly, we can be more selective with a narrow energy distribution of ions which arrive at the sample, essentially eliminating ions outside of a narrow distribution. In this way the effects of landing energy can be more precisely controlled.

SEISMIC represents an evolution of current electrospray ion beam deposition apparatus[13–16] and improves upon them in a range of aspects. From the more compact

design, greater ion flux and minimisation of user input for optimisation. Further tests exploring the limits of the experiments that can be completed with SEISMIC are currently underway and are heading in a number of interesting directions.

5 Using ESD-STM to Probe the Local Structure and Sequence of a Conjugated Polymer

5.1 STM studies of poly (C$_{14}$DPPF-F) – a donor-acceptor polymer

5.1.1 Introduction

Polymer synthesis was completed by Dr David Stringer and Professor Hugo Bronstein. X-Ray diffraction measurements were performed by Dr Anastasia Leventis and Professor Hugo Bronstein. Harry Pinfold and Professor Alessandro Troisi performed theoretical calculations.

The solid-state microstructure of a conjugated polymer is the most important parameter determining its properties and performance in (opto)-electronic devices. A huge amount of research has been dedicated to tuning and understanding how the sequence of monomers, the nature and frequency of defects, the exact backbone conformation, and the assembly and crystallinity of conjugated polymers impacts on their basic photophysics and charge transporting properties. However, due to the lack of reliable high-resolution analytical techniques, all the structure-property relations proposed in the literature are based either on molecular modelling or on indirect experimental data averaged on polydisperse samples. Here we show that a combination of electrospray vacuum deposition and high-resolution scanning tunnelling microscopy allows the imaging of individual conjugated polymers with unprecedented detail, thereby unravelling structural and self-assembly characteristics that have so far been impossible to determine.

The steadily increasing research in conjugated polymers is motivated by these materials being at the heart of low-cost, lightweight and flexible (opto)-electronic applications such as organic photovoltaics, light-emitting diodes, transistors, sensors, actuators and supercapacitors. In recent years, it has emerged that the electronic properties of these materials (such as charge carrier mobility, energy band-gap, adsorption spectrum, etc.) are controlled at their most fundamental level by six main characteristics of the polymer microstructure: (i) the polymer chemical composition[91]; (ii) the planarity of the backbone[131,132]; (iii) the relative conformation of the heterocycles[133]; (iv) the conformation and interdigitation of the solubilizing side chains[134]; (v) the interaction between polymer strands[135]; (vi) the presence and nature of chemical defects such as regioregularity[136,137] or polymerization defects[26,138,139].

The precise microstructure of conjugated polymers is however very difficult to determine, in particular for the new generation of materials that are based on complex

compositions of monomers obtained through multi- and co-polymerization techniques. Here the control on the final product is reliant upon differences in kinetic reaction rates with side-reactions being more difficult to prevent and the intrinsic statistical nature of the polymerization process becoming more apparent. Polymer sizes and mass distributions are mainly evaluated by chromatography (e.g. size exclusion chromatography (SEC)) and mass spectroscopy (e.g. MALDI), although these techniques often struggle to handle the complexity and heterogeneity of last-generation conjugated polymers. In particular, questions on the presence and nature of polymerization defects and on what the exact monomer sequence within a copolymer is, remain essentially unanswered. This constitutes a major limitation to further progresses in the field, as it hampers the possibility of better understanding the polymerization process and thus achieving a more precise control of the ensuing functional materials.

Herein we propose a novel and radically different approach to the analytics of conjugated polymers, based on high-resolution scanning tunnelling microscopy (STM). In order to fully harness the analytical power of STM and to image individual molecular species with subnanometer resolution, it is essential that the molecules are deposited in vacuum onto atomically clean and flat surfaces and that the measurements are performed in situ. Previous studies of conjugated polymers through the use of ambient STM at the liquid-solid interface have been completed[140,141] however due to the sometimes limited resolution these studies can miss finer structural details within assemblies of polymers. We achieve vacuum deposition of intact polymers by exploiting recent advances in the soft landing of thermolabile molecules[18,142], thereby demonstrating a significant development in vacuum electrospray deposition (ESD)[53,143–146]. In this chapter we report the first combination of ESD with sub-molecular resolution STM to analyse diketopyrrolopyrrole (DPP) based polymers. We demonstrate the ability to identify the monomer units and the solubilizing alkyl side-chains and use this to precisely sequence the polymer structure. Importantly, we show that we can determine the nature, locate the position, and ascertain the number of defects in the polymer backbone. Our analysis also reveals that the main driver for backbone conformation of surface-adsorbed polymers is the maximization of alkyl sidechain interdigitation, which leads to unexpected cis conformations of the heterocycles. This unique insight into the microstructure of conjugated polymers is

not attainable by any other existing analytical technique and represents a fundamental advance in polymer analytics.

A commonly used DPP based polymer Poly Tetradecyl-diketopyrrolopyrrole-furan-co-furan (poly (C$_{14}$DPPF-F)) has been used. Poly (C$_{14}$DPPF-F) is an example of the most recent generation of donor acceptor polymers which consist of alternating donor (D) and acceptor (A) monomers. The synthetic procedures used lead to an expected polymer sequence of (DA)$_n$. These type of polymers have been shown to have high efficiency as use as the active layers in organic solar cells as well as field effect transistors[147].

5.1.2 Self-assembled islands of poly (C$_{14}$DPPF-F)

Poly (C$_{14}$DPPF-F) was deposited for 15 minutes at a current of 20 pA via the electrospray procedure outlined in section 3.2.4 resulting in a coverage of approximately 60%. The surface was annealed to 100 ºC for 10 minutes and cooled to -153 ºC before being imaged by STM.
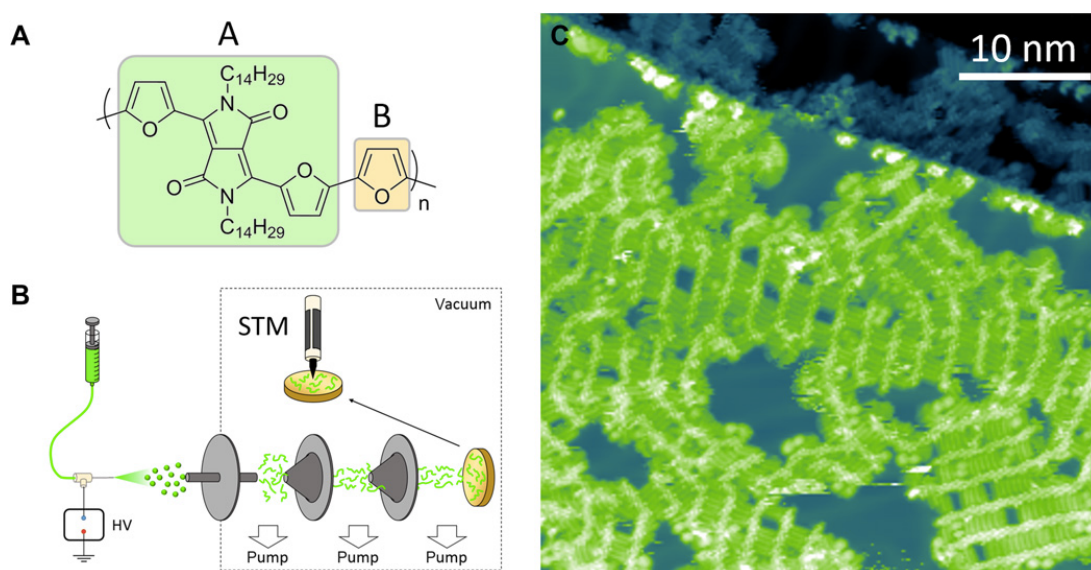
Figure 5.1 Vacuum deposition and STM imaging of poly (C$_{14}$DPPF-F) polymers. (A) Molecular structure of poly (C$_{14}$DPPF-F). (B) Schematic representation of the experimental setup. (C) STM image showing poly (C$_{14}$DPPF-F) adsorbed on Au(111) after annealing to 100 °C. The polymer backbones appear as bright rows, and the alkyl side chains are seen as darker rows perpendicular to the backbones. V = -1.8 V, I = 300 pA.

Poly Tetradecyl-diketopyrrolopyrrole-furan-*co*-furan (poly (C$_{14}$DPPF-F), Figure 5.1 A) is a conjugated polymer of the DPP-based family[100] that is currently showing some of the best performance in optoelectronic devices. Figure 5.1 shows a typical STM

image of poly (C_{14}DPPF-F) deposited by electrospray on a Au(111) surface at room temperature, demonstrating that both the polymer backbone and the alkyl sidechains can be clearly identified. The backbones of the polymers are mostly straight and tightly aligned with the $[11\bar{2}]$ directions of the Au(111) herringbone reconstruction, even bending around the elbow sites of the reconstruction, which indicates a strong molecule-substrate interaction. The alkyl chains are generally oriented perpendicular to the backbone and are thus aligned along the $[\bar{1}10]$ substrate directions. The polymer strands self-assemble into extended two-dimensional (2D) islands through attractive interactions between the alkyl side-chains. Chains of neighboring polymer strands interdigitate to maximize van der Waals contact, resulting in an inter-strand separation of 2.6 ± 0.1 nm, in excellent agreement with what has been observed for small furan-DPP molecules[148] with the same structure as the monomer repeat unit shown in Figure 5.1. A drop cast thin film of poly (C_{14}DPPF-F) was also prepared and analysed by thin film X-ray diffraction (XRD, see Figure 5.2). This showed (100) and (200) Bragg reflections at $2\theta = 4.3°$ and $8.6°$ respectively. These values are indicative of a lamellar distance of 2.05 nm which is considerably shorter than the total width of the molecule (~4 nm), indicating interdigitation is likely to be occurring also in the solid state (as has been observed for other conjugated polymers[134]). Therefore, we speculate that the intermolecular ordering observed here provides insight for the local assembly of a bulk sample, but that the bulk sample may have a different geometry to that seen in the first layer growth. This is an area of great interest and further work is underway in order to investigate how the first layer growth influences the bulk structure growth.
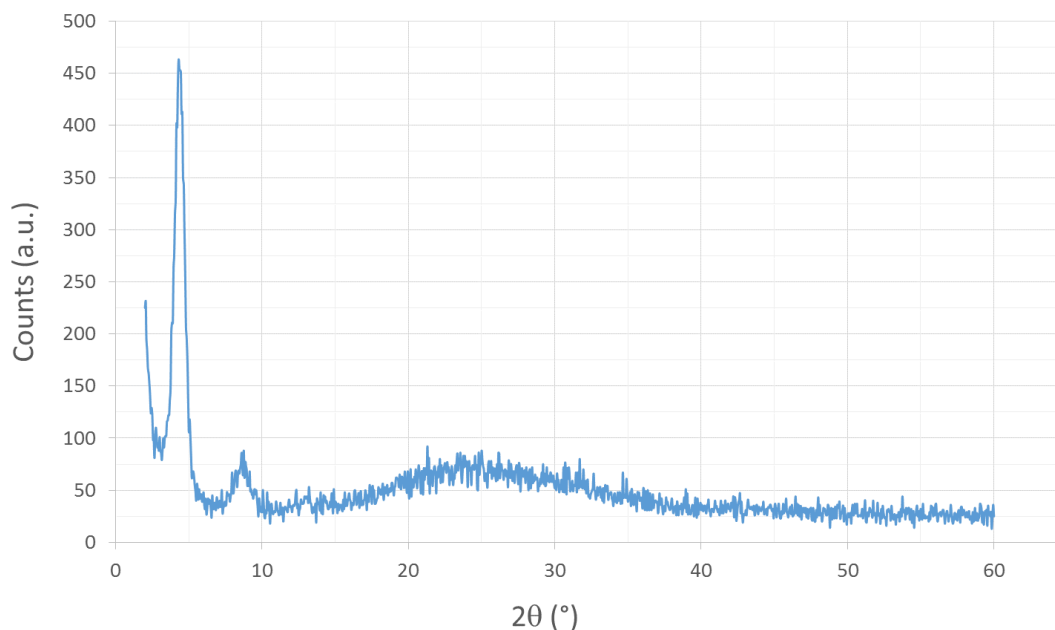
Figure 5.2 XRD of a drop cast thin film of poly (C$_{14}$DPPF-F).

Higher magnification STM images (Figure 5.3), display a periodic sub-molecular contrast, allowing for the identification of the individual monomer units – DPPF (A) and furan (B) – and their sequence in the polymer chain. The DPPs form an angle of approximately ± 45° with respect to the straight backbone axis and are the points from which the alkyl side chains extend. The so-determined AB repeat unit has an excellent match with any STM image containing a section of polymer with no defects as seen in Figure 5.3.
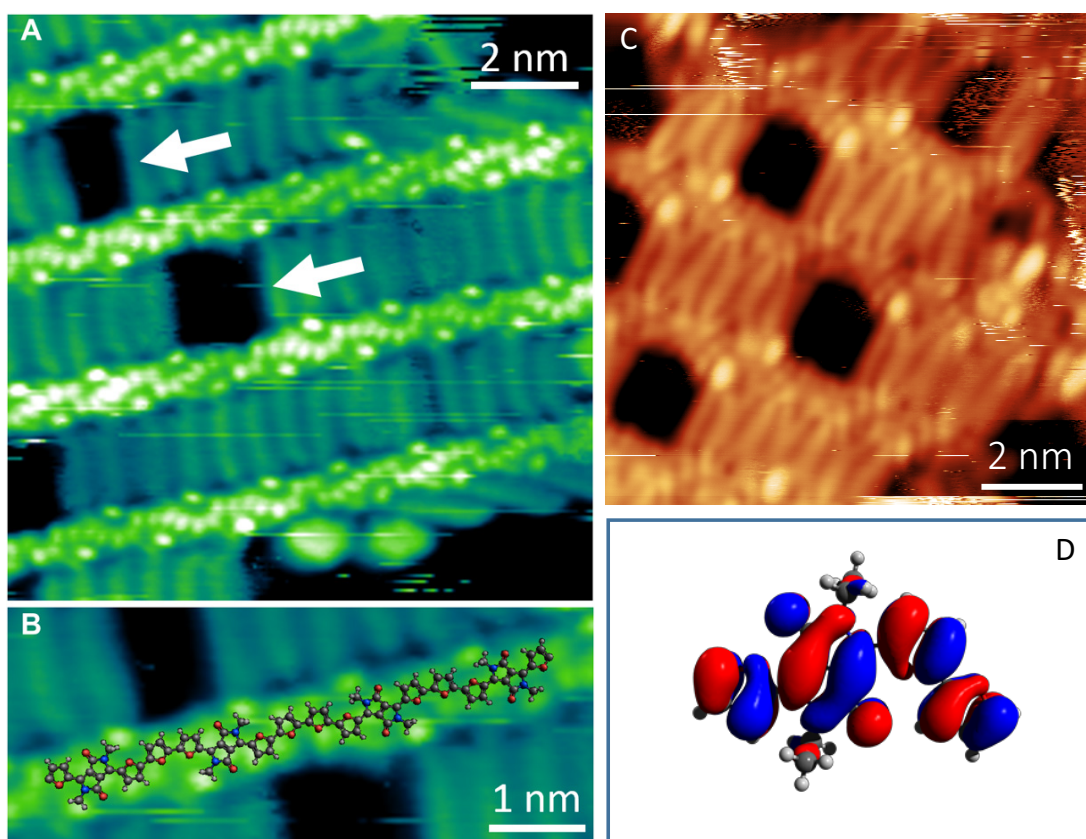
Figure 5.3 High-resolution STM images of poly (C_{14}DPPF-)F polymers on Au(111). (A) Submolecular resolution of the polymer backbone and the interdigitation of the alkyl side chains. White arrows indicate gaps in the alkyl chain interdigitation. (B) Molecular model of the polymer backbone overlaid on a section of poly (C_{14}DPPF-F) (C atoms are shown in grey, O in red, N in blue, and H in white). The alkyl chains have been substituted with methyl groups for better visualization. An ABBA defect is visible in the centre of the image. (V = -1.8 V, I = 300 pA). (C) High-resolution STM images of poly (C_{14}DPPF-)F polymers on Au(111) (V = 1.5 V, I = 300 pA). (D) DFT simulation of the HOMO for a monomer of (C_{14}DPPF-)F showing a similar shape to the contrast seen in (A).

5.1.3   Chain length distribution and estimated mass distribution

The STM images can be used to evaluate the mass distribution of the polymer chains. This is not only useful information as mass distributions of polymers can be difficult to attain but is also a good check that these results represent a good sampling on the polymer distribution. The number of repeat units is obtained by measuring the length of a large number of polymer strands (164) and counting the number of repeat units present in each, this results in an average value of 17 ± 7 monomer units per chain. By multiplying this by the mass of a single repeat unit (724 Da), the average mass of the polymers is evaluated to be 12.2 ± 4.8 kDa (the full size and mass distribution are shown in Figure 5.4). This value can be compared with what is obtained from size

exclusion chromatography (SEC) measurements on the same polymer, which resulted in a number average (M_n) and weight average (M_w) molecular mass of 6.4 and 37.3 kDa, respectively (as measured by high temperature SEC, Figure 5.5).
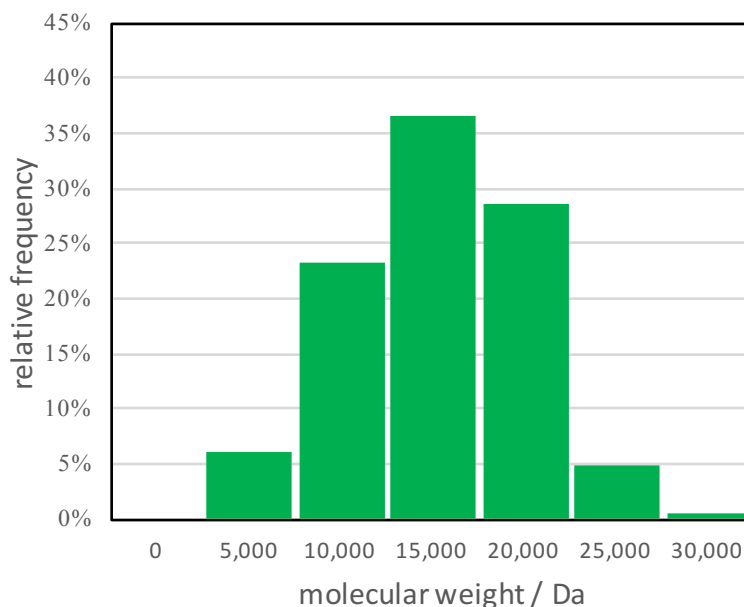
Figure 5.4 Analysis of the mass distribution of poly (C_{14}DPPF-F) on Au(111). Histogram of molecular weight distribution determined from STM images (see text for detailed methodology).

The mismatch in the measured molecular weights (between SEC and STM measurements) is likely a consequence of the methodology used. SEC is known to provide inaccurate evaluations of the true molecular weight of conjugated polymers[108] as they are measured relative to polystyrene standards which have notably different hydrodynamic radii, with uncertainties up to a factor of 2 having been reported[149]. Additionally, solution aggregated species are commonly observed in narrow band-gap conjugated polymers[150], further affecting the measured molecular weight. A further possibility which could lead to the discrepancy is in the electrospray process. It is known that electrospray mass spectra peak intensities do not indicate the relative concentrations of species present in the solution[151] but instead selectively charge some molecular species over others. However, as this work has been carried out using the Molecular Spray equipment this should not be an issue. That is, it is assumed that a large number of neutral molecules reach the surface due to the direct line of sight between the inlet capillary and the surface.
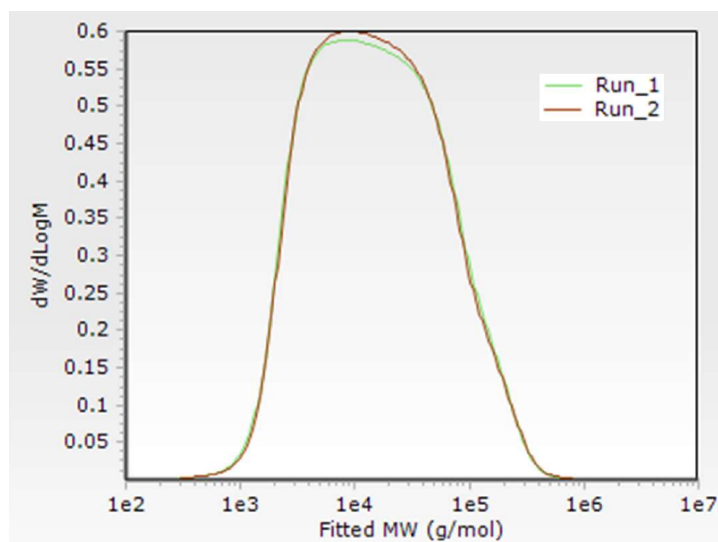
Figure 5.5 GPC molecular weight analysis of poly (C$_{14}$DPPF-F) at 160°C. Overlay of molecular weight distributions for two repeat experiments. Run_1: Mn = 6,400 Da, Mw = 37,300 Da; Đ = 5.87. Run_2: Mn = 6,500 Da, Mw = 39,400 Da; Đ = 6.06.

Additionally, the length analysis was completed by measuring the length of each polymer chain whose entire length was contained within the scan frame. The logic behind only including those polymers whose entire length can be seen is fairly obvious, one cannot predict how much further outside of the scan frame a polymer extends and therefore cannot accurately record the length. The consequence of this is that there is a preference towards shorter chain length polymers which are more likely to be included inside a scan frame of a given size. Therefore, we can conclude that this selection in evaluating the chain length and inferring the molecular mass may also contribute towards the discrepancy between the SEC and STM values.

5.1.4   Fitting a molecular model and sequencing a conjugated polymer

The detail which can be seen in the backbone of the polymer can be used in order to accurately fit a molecular model to the polymer and attempt to determine the sequence of monomers within. As stated before, the sequence of monomers within a conjugated polymer is key in determining its properties and at present there exists no analytical technique which can gain insight into this for individual polymer molecules. Attempts have been made via MS-MS to sequence polymers but these results have been obtained from samples specifically designed for this purpose with predictable fragmentation patterns[152,153]. Further, these type of measurements are the result of averaging from a large number of polymers which, on the one hand, provides better statistics for measurements but means individual mistakes may be masked or missed entirely.
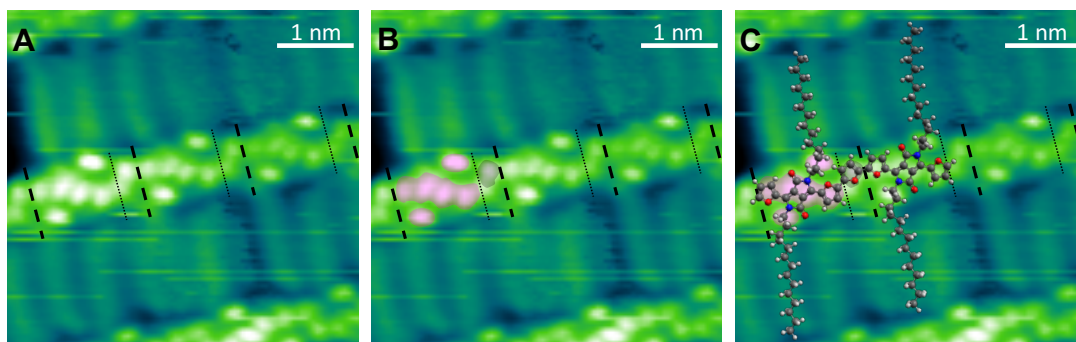
Figure 5.6 High-resolution STM images of poly (C$_{14}$DPPF-F) and corresponding molecular models. (A) Monomer (AB) repeat units are separated by thick dashed lines, individual A (DPPF) and B (furan) subunits by thin dotted lines. (B) Same image as (A) with the characteristic 4+2 bright lobes of A and the single bright lobe of B highlighted in pink and grey, respectively. (C) Same image as (B) with the molecular model superposed onto part of the central polymer strand. V = -1.8 V, I = 300 pA.

To assign the features appearing in the backbone, the unambiguous location of the alkyl side-chains is used as a reference. The chains extend from two circular lobes situated at opposite positions with respect to the main polymer axis and correspond to the first carbon atoms extending from the DPP moieties (Figure 5.6). Quantum chemistry calculations show that the alkyl chains are not coplanar with the DPP moiety (Figure 5.7) allowing to identify these two lobes with the protruding start of the alkyl chains and to precisely locate the A monomer. This corresponds to four aligned bright dots within the backbone, two central ones for the DPP unit, and two on each side for the lateral furan rings (Figure 5.6). The position of the B monomer is also determined by using a geometry-optimized molecular model and appears to coincide with a fifth bright dot.
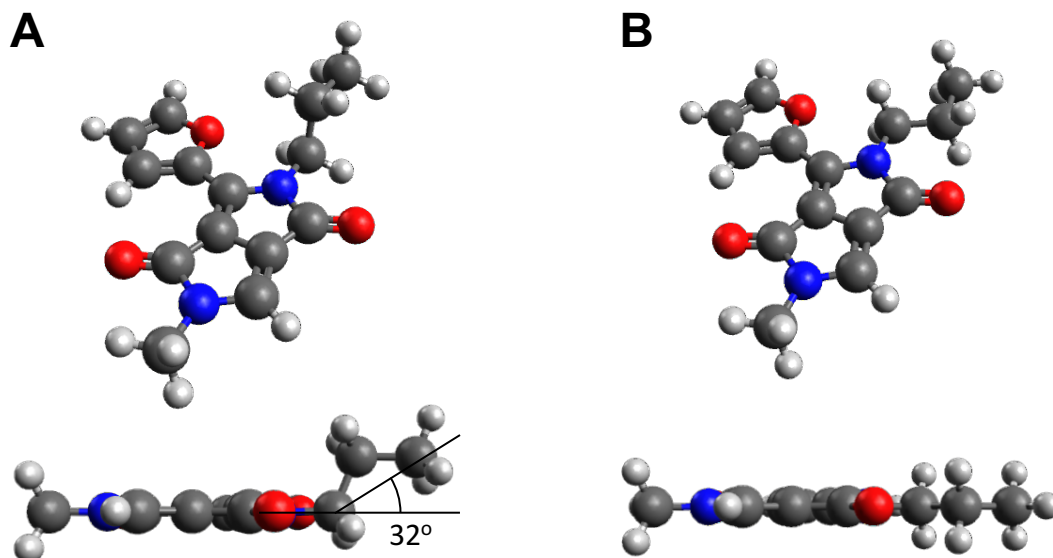
Figure 5.7 Ab initio calculations of the conformation of alkyl chains with respect to the polymer backbone. (A) Lowest energy conformation with the alkyl chain forming an angle of 32° with the plane of the DPP unit. (B) Conformation with the alkyl chain in the same plane as the DPP unit, 252 meV higher in energy than the conformation in (A).

The final dimer unit (seen in Figure 5.6), which also includes 14 carbon alkyl chains extending from the DPP units, has an excellent agreement with the defect free polymer backbone seen in this image and matches well with all other sections of defect free polymer which have been imaged. There are instances where this sequence and orientation of monomer units does not fit; where defects in the monomer sequence have appeared.

5.1.5 *Identifying defects in the chain sequence*

Two main types of defects can be recognized in the 2D assembly of poly (C_{14}DPPF-F): darker gaps in the interdigitation sequence of alkyl side-chains; and circular protrusions, which can be found either within these gaps or at the edge of polymer islands (Figure 5.3 A). While the circular protrusions are attributed to impurities either in the solvent or in the sample, the gaps are linked to defects in the monomer sequence of the polymer. Each gap is accompanied by a change in the orientation of the submolecular features (assigned as the DPP units) in one of the two polymer backbones delimiting the gap itself (wider gaps, as in the center of Figure 5.3, show an inversion in both flanking polymer backbones). Moreover, an additional bright dot is always observed between successive DPP units in correspondence to the gaps. In fact, while in the regular parts of the polymer strand the distance between consecutive DPPs is 1.4 ± 0.1 nm – corresponding well to the expected periodicity of a regular $(AB)_n$ polymer sequence – it becomes 1.8 ± 0.1 nm across the gaps.
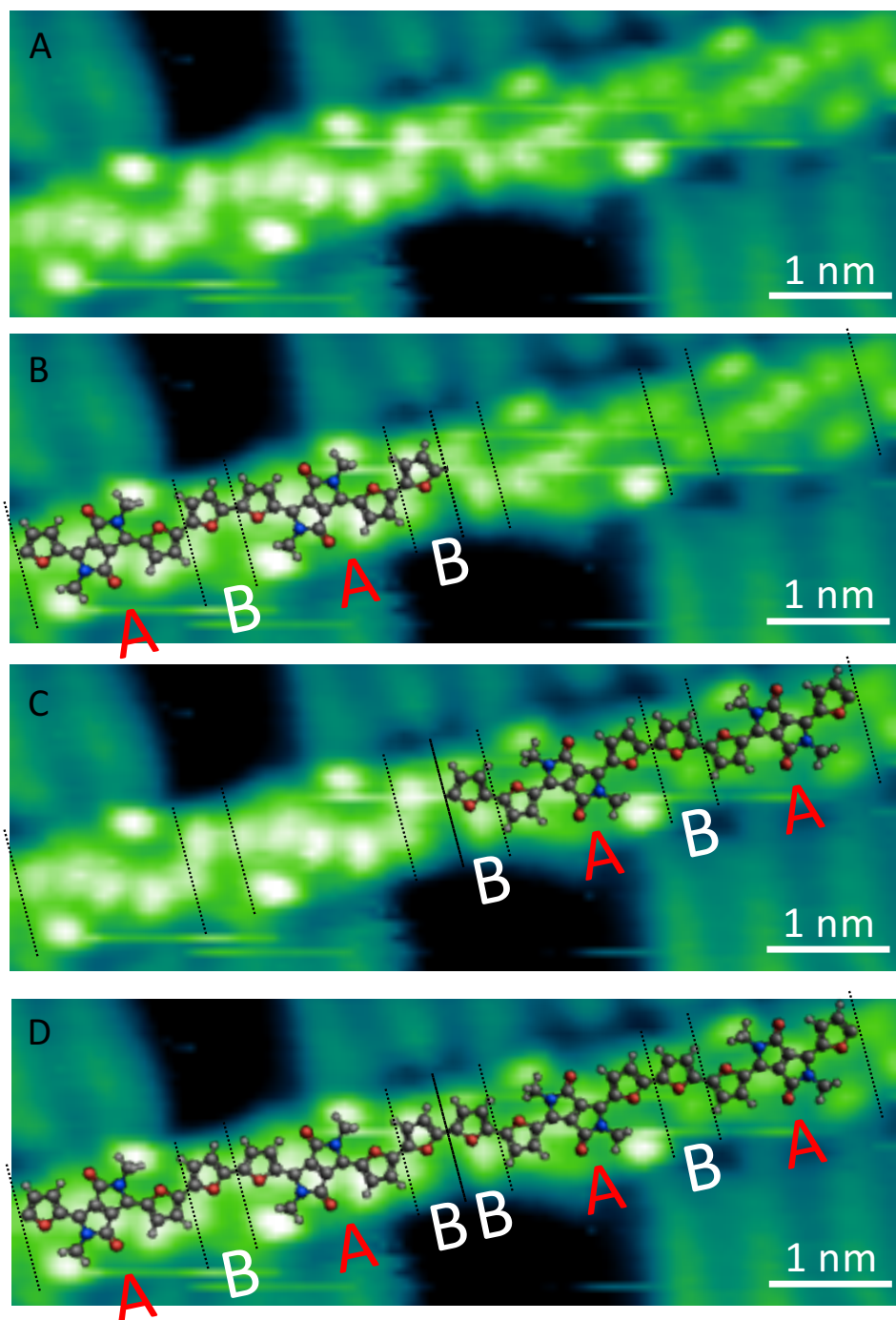
Figure 5.8 Fitting a model to the defective regions of the C$_{14}$DPPF-F polymer deposited on Au(111). (A) STM image of sub-molecular contrast of the polymer. (B) Overlay of a molecular model of the defect-free region. (C) Overlay of a molecular model to the defect-free region inverted through a mirror plane centred at the defect. (D) Overlay of a molecular model containing the ABBA defect at the centre. V = -1.8 V, I = 300 pA.

The defective regions can be explained by the same molecular model described in Figure 5.6 if, at the position of the gaps, the model is inverted through a mirror plane perpendicular to the polymer backbone, resulting in an extra furan ring and an ABBA

101

monomer sequence (Figure 5.8). A detailed analysis of the high-resolution STM images can thus reveal the presence of defects in the monomer sequence and identifies these as ABBA (instead of the regular ABAB) arrangements. Only this type of defect was observed in all analyzed images with the exception of two single occurrences of an ABBBBA defect (see Figure 5.9). It is speculated the ABBBBA defect has occurred from the coupling of two ABB defective chain ends.
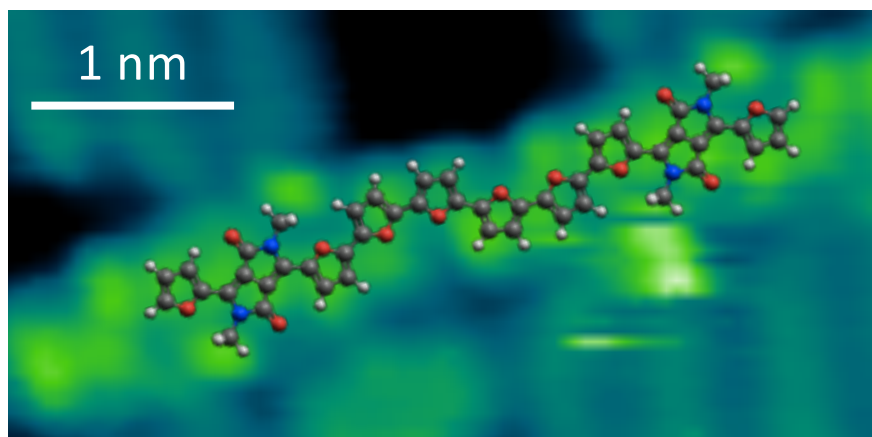
Figure 5.9 STM image of ABBBA defect within the $C_{14}DPPF$-F polymer deposited on Au(111) with an overlay of the molecular model. V = -1.8 V, I = 300 pA.

An evaluation of a large number of polymer strands (180) shows that there is approximately one defect in every 10 nm of strand length, which is equivalent to one extra B monomer for every 8.5 AB units. In particular, Figure 5.10 shows that the number of defects in a polymer strand scales linearly with its length, as would be expected for a random inclusion of defects. Moreover, Figure 5.10 also demonstrates that this linear relation holds across a large range of molecular weights, indicating the generality of this result.
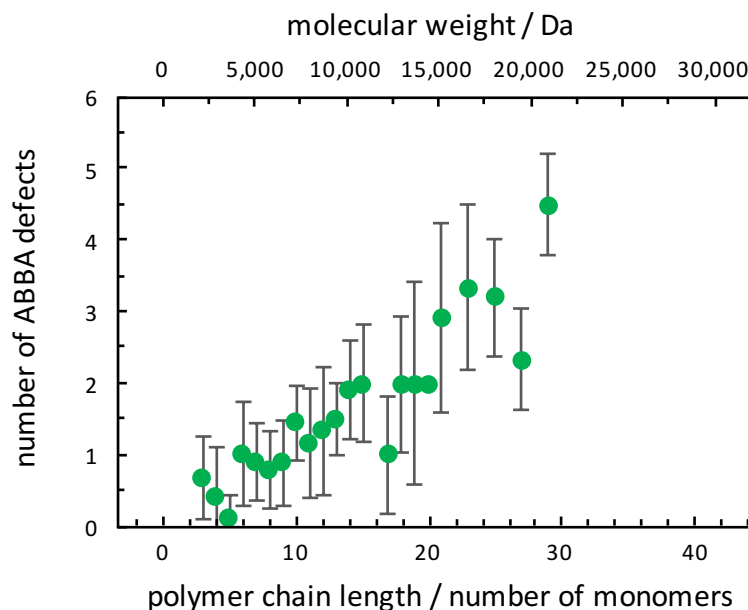
Figure 5.10 Analysis of the defect frequency of poly (C14DPPF-F) deposited on Au(111). Frequency of ABBA defects as a function of the polymer chain length expressed as number of (AB) monomers or molecular weight. A linear dependence is visible.

5.1.6 Alkyl chain interdigitation

It is evident from the STM images that the polymer side-chain interaction, maximized by interdigitation, strongly influences the orientation of the alkyl chains. This is clearly seen in Figure 5.3 where a number of chains at the edge of a molecular island (top and bottom right corner of Figure 5.3) are significantly distorted with respect to those within the island. Perhaps more surprisingly, the drive to maximize alkyl chain interactions is also responsible for the orientation of the monomers within the polymer backbone. In fact, while the commonly assumed all-trans-conformation of the furan units predicts an alternating orientation of the DPPs (Figure 5.11 A), the STM images clearly show that the DPP units are all parallel to each other in the defect-free regions of the polymer (Figure 5.3). Alternating orientations of the DPP moieties imply alternating large and small separations between the alkyl chains which are not ideal for intermolecular interactions (Figure 5.11 C). On the other hand, a backbone configuration where one of the furan units of the A monomer is cis to the furan of the B monomer (Figure 5.11 B) would have equally spaced alkyl chains, allowing an ideal interdigitation (Figure 5.11 D). The conformation in Figure 5.11 B is obtained from that in Figure 5.11 A through 180° rotations around the C-C bonds between the A and B monomers and is thus characterized by having all DPP units parallel to each other,

as experimentally observed DFT calculations show that the conformation in Figure 5.11 B is only 0.06 eV less stable than that in Figure 5.11 A and that the two can easily interconvert through a barrier of 0.32 eV (Figure 5.12).
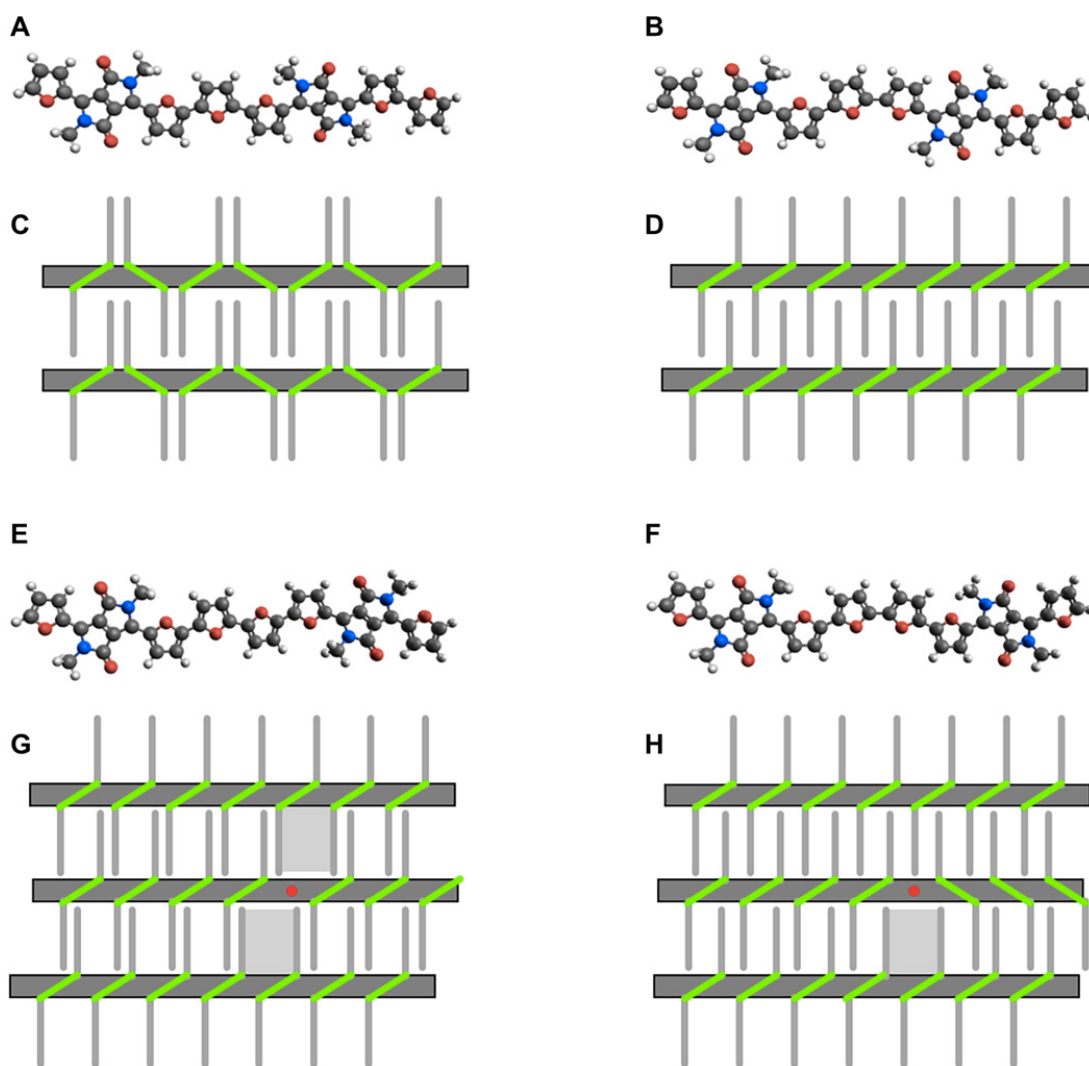
Figure 5.11 Molecular structure and intermolecular interactions of pristine and defective C₁₄DPPF-F polymers. (A and B) Structure of defect-free poly (C₁₄DPPF-F) in the all trans configuration (A) and with a single furan-furan cis arrangement (B), demonstrating specular and parallel DPP orientations, respectively. (C and D) Schematic representation of interstrand interactions for the polymer configurations corresponding to (A) and (B), respectively. The alkyl chains are represented by thin grey lines, and the DPP units are represented by green segments. (E and F) Structure of poly (C₁₄DPPF-F) around an ABBA defect in the all-trans configuration (E) and with a single furan-furan cis arrangement (F). The DPP units across the defect are arranged in a parallel and specular orientation, respectively. (G and H) Schematic representation of interstrand interactions for the polymer configurations corresponding to (E) and (F), respectively. The ABBA defects are represented by red dots, and larger gaps in the chain interdigitation are represented by grey-shaded areas.

The parallel orientation of the DPPs is disrupted across ABBA defects, where the DPP units are specular to each other (Figure 5.3). Also in this case, optimization of the intermolecular interaction is the driving force since an all-trans conformation with an extra furan ring (parallel DPPs, see Figure 5.11 E) would create two gaps in the sidechain interdigitation, one on each side of the defective strand (Figure 5.11 G). On the contrary, the experimentally observed configuration, obtained by a 180° rotation around the C-C bond connecting the two central furans (specular DPPs, Figure 5.11), generates a gap only on one side of the defective strand and thus allows a better alkyl chain interdigitation (Fig. 4H).
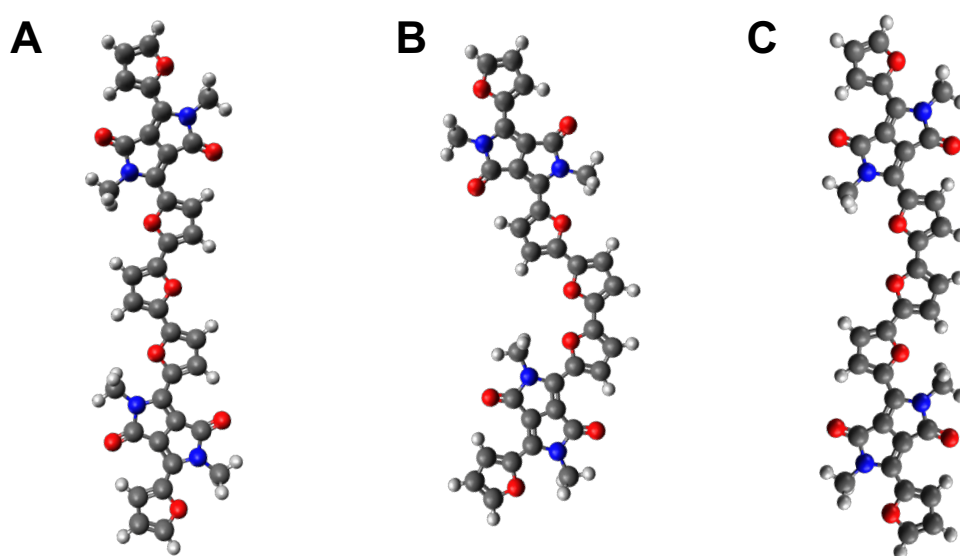
Figure 5.12 Gas-phase optimized structure of a C$_{14}$DPPF-F oligomer. (A) Optimized structure for the all-trans conformation. (B) Optimized structure with one pair of furan units in cis conformation, obtained from (A) through a 180° rotation around a C-C bond. (C) Optimized structure obtained from (B) by constraining the DPP units to be parallel.

It should be noticed that the backbone of a defect-free isolated C$_{14}$DPPF-F polymer in the conformation with parallel DPPs would not be straight but curved, due to the optimal angle between heterocycles (see vacuum DFT optimized structure in Figure 5.12 B). This curved conformation is however observed only in isolated strands while, in the majority of cases, the polymer backbones are straight within the molecular islands (Figure 5.13). This latter conformation maximizes side-chain interdigitation by having evenly spaced alkyl chains and the calculations show that the energetic cost of straightening the polymer backbone, is compensated by the better alkyl-alkyl chain interactions formed in ideally interdigitated monolayers. The strong polymer-substrate

interaction and the likely electronic hybridization between the two is expected to play an important role too. On the other hand, the phenomena presented here do not depend on the specific metallic substrate, since the same alkyl chain interdigitation and the same structure of the backbone (straightness, monomer orientation, and defects) were observed also when poly (C_{14}DPPF-F) was deposited on Ag(111) (see section 5.1.7).
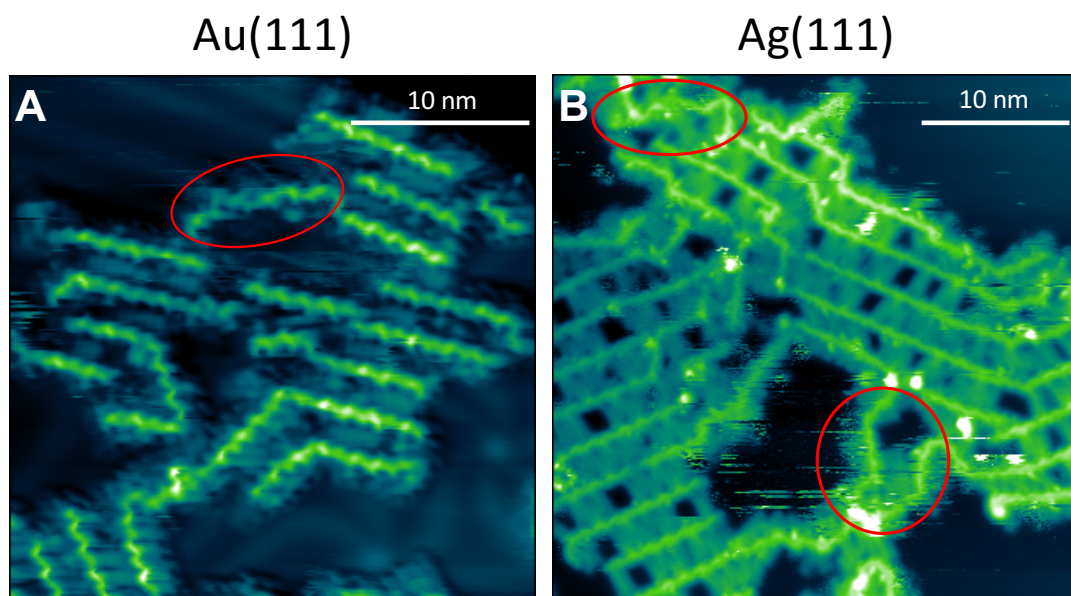
Au(111)   Ag(111)

Figure 5.13 STM images of C_{14}DPPF-F polymers deposited on Au(111) and Ag(111). (A) STM image showing poly (C_{14}DPPF-F) adsorbed on Au(111) after annealing to 100°C. The polymer backbones are mostly straight within molecular islands in order to maximise side-chain interdigitation. A curved conformation is however observed for isolated strands, one of which is circled in red. (B) STM image showing poly (C_{14}DPPF-F) adsorbed on Ag(111) after annealing to 100°C. Irrespectively of the substrate, the same alkyl chain interdigitation and the same structure of the backbone (including monomer orientation and defects) as observed. In particular, also on Ag(111) interdigitated polymers have a straight backbone conformation while isolated strands are much more curved. V = -1.5 V, I = 350 pA.

As mentioned, the calculations show that the energy gained by a linear polymer backbone with alkyl side chain interdigitation makes up for the energy loss in having to straighten the polymer. Structure B in Figure 5.12 is 8.4 kcal/mol higher in energy than structure C in the same figure. This value is given per monomer unit in the chain. The interaction energy has been computed for a number of n-alkane chains[154], for two interacting decane chains the interaction energy is given to be 7.5 kcal/mol. Decane has been used as opposed to tetradecane due to the non-planar geometry of the first 4 carbon atoms in the alkyl chain (Figure 5.7) which we expect will reduce the

interaction energy between these segments. What must also be considered is the number of alkyl chain interactions per monomer unit.
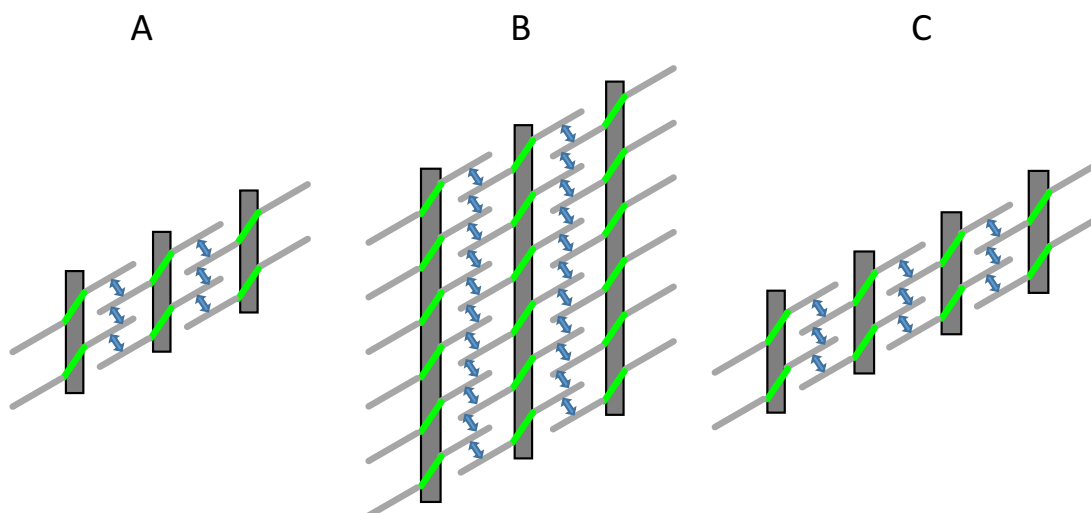
Figure 5.14 Schematic representation of intermolecular interactions for C$_{14}$DPPF-F polymer chains of varying lengths and number of monomers per chain. Grey boxes represent polymer backbones, green lines represent DPP units, grey lines represent alkyl chains, and blue arrows indicate pair-wise alkyl side chain interactions. (A) 3 polymer chains of 2 monomers, (B) 3 polymer chains of 6 monomers and (C) 4 polymer chains of 2 monomers.

Table 5.1 Number of alkyl chain interactions per monomer unit as a function of polymer chains in an island and number of monomer units in a polymer chain.

	A	B	C	General
Number of polymers	3	3	4	N
Monomer units per polymer	2	6	2	M
Alkyl chain interactions	6	22	9	$(2M-1)(N-1)$
Alkyl chain interactions per polymer	2	7.33	2.25	$\dfrac{(2M-1)(N-1)}{N}$
Alkyl chain interactions per monomer unit	1	1.22	1.125	$\dfrac{(2M-1)(N-1)}{NM}$

Depicted in Figure 5.14 and given numerically in Table 5.1 is a demonstration of how the number of alkyl chain interactions scales with both the number of monomer units in a polymer chain and the number of polymer chains in an island. What this results in is a general formula for the number of interactions per monomer unit, which is given below: where I is the number of alkyl chain interactions per monomer unit; N is the number of polymer chains in an island assembly; and M is the number of monomer units per polymer chain.

$$I = \frac{(2M-1)(N-1)}{NM}$$

Using this formula, the average number of monomer units per chain (17) and the average number of chains in an island of polymers (12) we obtain that there are on average 1.78 alkyl chain interactions per monomer unit. Taking this value and multiplying it by the interaction energy of a pair of decane chains we obtain a value of 13.3 kcal/mol. This value more than compensates for the energy required for straightening the backbone of the polymer chain.

5.1.7   Poly (C₁₄DPPF-F) on Ag(111)

The same experiments were also completed on a Ag(111) substrate in order to try and understand the degree to which the substrate influenced the assembly of the polymer on the surface.

Poly (C$_{14}$DPPF-F) was deposited for 15 minutes at a current of 20 pA resulting in a coverage of approximately 60%. The surface was annealed to 100 °C for 10 minutes and cooled to -153 °C before being imaged by STM.
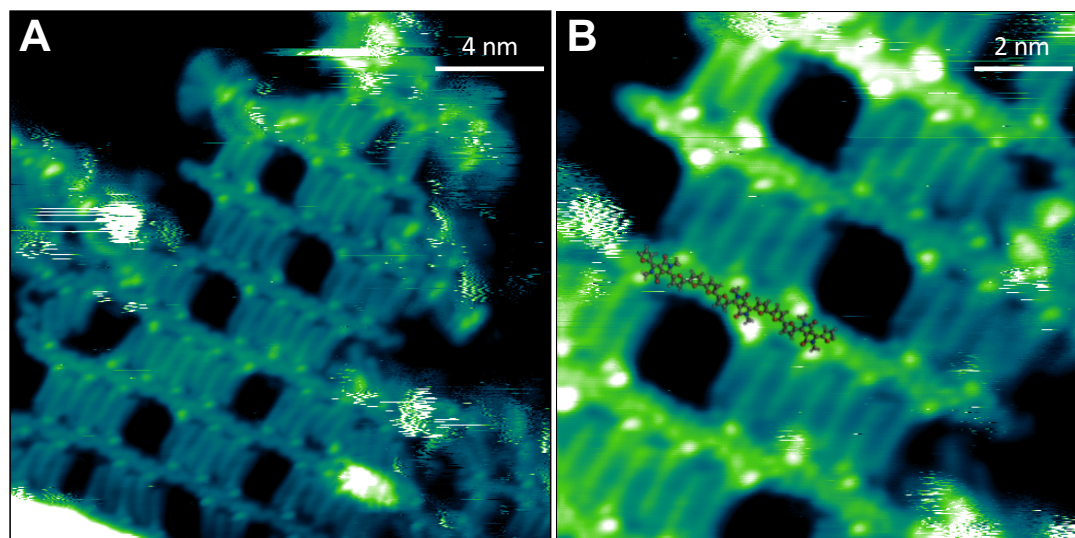
Figure 5.15 STM images of poly (C₁₄DPPF-F) polymers deposited on Ag(111) after annealing to 100°C. (A) Large scale STM image showing dark gaps in the interdigitation sequence of alkyl side-chains caused by ABBA defects in the monomer sequence. (B) Higher magnification STM image demonstrating the parallel orientation of DPP units in unfaulty sections of the polymer strand, and specular orientation across defects. A molecular model of the polymer backbone is overlaid on

part of a polymer strand. The alkyl chains have been substituted with methyl groups for better visualisation. The alkyl chain interdigitation and the structure of the backbone (straightness, monomer orientation, and defects) are the same as those observed when poly (C_{14}DPPF-F) is deposited on Au(111). V = -1.5 V, I = 350 pA.

Figure 5.15 shows a typical STM image of the polymer on the Ag(111) surface. It is immediately obvious that there are a number of similarities in the assembly of poly (C_{14}DPPF-F) on Ag(111) as compared to Au(111).

Firstly, in both cases polymers have formed 2D islands with chains held together through interdigitation between strands, with the same chain-chain separation of 2.6 ± 0.1 nm. We also note that the defects within the polymer backbone present themselves in the same fashion for both adsorptions on Ag and Au. That is, the same flipping of DPPs is present indicating that the driving force for this is maximisation of alkyl chain interdigitation and is not dependent on a particular surface geometry. We also see the same characteristic bright blob indicative of the first few carbons of the alkyl side chain. Again we can overlay a molecular model and confirm that this once again fits with the model from section 5.1.4. Numerically, the spacing between parallel DPP units is again measured to be 1.4 ± 0.08 nm and for specular DPP units to be 1.8 ± 0.07 nm.

We again use the molecular model to assess the mass distribution of the polymer chains on Ag(111). By analysing a large number of chains (127) from different regions of the sample we measure that there are an average of 16 ± 6 monomer units per chain (with a corresponding mass distribution of 11.6 ± 4.9 kDa), which is in very close agreement with what was seen on Au(111) suggesting the surface has not played a significant role in selecting for different chain length molecules. The full size distribution can be seen in Figure 5.16.
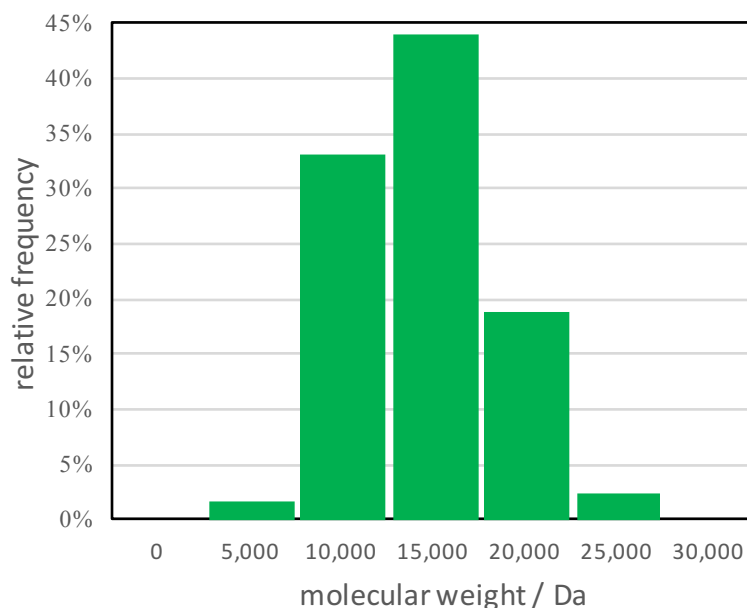
Figure 5.16 Analysis of the mass distribution of poly ($C_{14}DPPF$-F) on Ag(111). (A) Histogram of molecular weight distribution determined from STM images (see text for detailed methodology).

The agreement between the results on Ag(111) and Au(111) provide further evidence that the polymer we sample on the surface is representative of the bulk solution and that the surface selection is not playing a significant role on the results.

5.2 Summary

In summary, we have presented a radical new approach to polymer analytics based on the concept of structural analysis through high-resolution microscopy[27]. The unprecedented spatial resolution of our STM images allows us to precisely sequence conjugated polymers by simply counting the monomer units. This is used to demonstrate the presence of unexpected ABBA defects in the poly ($C_{14}DPPF$-F) co-polymer and to quantify their occurrence. The existence of chemical defects in a conjugated polymer backbone has long been speculated and suggested[155]. While these defects have been identified as possible exciton trap sites, little was known about their nature and their frequency, although it has always been assumed that they were either torsional defects in the backbone – i.e. hairpin defects[156] – or chemical defect – which can be either intrinsic[157] or extrinsic[158]. In the specific case of DPP polymers, it has been suggested that the primary defects are chemical, resulting from the homocoupling between the DPP-containing units[26,139]. Here we show unambiguously that this is not always the case, by identifying the chemical defects in the poly ($C_{14}DPPF$-F) co-

polymer as homocouplings between furan rings. By proving the possibility of attaining a detailed understanding of the amount and types of defects in conjugated polymers, our work demonstrates the potential to finally resolve this long-standing issue and to establish an essential – presently still missing – structure-property relationship. A further emerging field of research that would highly benefit from the analytical advances demonstrated here, is the recent development of greener methods for the synthesis of conjugated polymers. New synthetic strategies such as the direct arylation polymerization[159] do not rely on the use of highly toxic tin-containing compounds but produce conjugated polymers with widely varying properties, often inferior to those obtained using conventional reaction schemes (e.g. via the Stille cross coupling reaction[160]). Although progress has been made using the conventional analytical techniques of NMR, MS, and SEC it is still not clear what the origin of the defects is and how they can be avoided. Using the ESD-STM technique, it would be possible to analyse polymers synthesized by different methods, identify and quantify the defects, and then relate these to the measured optical and electronic properties. Current work by Meyer and co-workers[161,162] combining electrospray deposition and non-contact atomic force microscopy (ncAFM) could provide even greater insight into the sequence and location of defects within conjugated polymers due to the additional information ncAFM contrast can afford[30,31,35].

The analysis of the STM data also allowed the determination of the orientation of individual monomers within the polymer backbone, showing that surface-adsorbed polymers adopt unexpected conformations in order to optimize intermolecular interactions. These results represent a further unique insight into the microstructure of conjugated polymers that is not attainable by any other existing analytical technique.

Since the sequence of a polymer is clearly not altered when adsorbed on a substrate, the chemical composition uniquely determined from our STM analysis is valid in absolute terms and thus relevant to any type of device or application involving this material. This might not be true for some aspects of the observed 2D assembly, which could result from the interaction with a metallic surface and thus not be representative of the solid-state bulk packing. However, we believe that other features – such as the maximization of alkyl chain interdigitation – are very general and that our work thus lends insight relevant for the local packing of functional polymeric thin films. As we

will see in later chapters this rule of alkyl chain interdigitation holds for a number of related polymer systems we have also investigated.

We speculate that this novel approach might have profound impact on the wider field of polymer science, representing a first, fundamental step in tackling a major and still unresolved problem, i.e. how to precisely and reliably characterize a polymeric macromolecule with monomeric precision.

6 ESD-STM as a new analytical tool to investigate conjugated polymer synthesis

6.1 Conjugated polymer synthesis and the developments in conjugated polymer structures

All molecules in this section have been synthesised by Dr Anastasia Leventis and Professor Hugo Bronstein.

There are many synthetic pathways and reaction conditions which can be used to synthesise a conjugated polymer and the choice of method depends heavily on the requirements of the final product[91,163]. The latest generation of conjugated polymers rely on specific patterns of monomer repeat units and a great level of control over the chain length in order to achieve the highest device efficiencies[100]. A great number of factors are considered when designing a conjugated polymer for use in an organic solar cell or other organic electronic devices. They range from the electronic structure of the polymer to the physical properties such as the ability to be easily cast in a film[91].

The simplest conjugated polymer structure is a homopolymer – the same monomer unit repeated in a sequence. A commonly studied example of this is poly (3-hexylthiophene-2,5-diyl) (P3HT)[164]. Due to the good processability and relatively easy and controllable synthesis which can be used to create the regioregular version of P3HT[97,165], this type of polymer has been widely studied[166] and significant amounts of research activity are still invested in developing devices based on this molecule. This synthesis is well understood. As such, P3HT in particular, and homopolymers in general were not chosen as system where to further test the analytical capabilities of ESD-STM.

Alternating co-polymers are also a common structure where two monomer units are added in an alternating sequence to build the polymer molecules[98,99,131,167]. In the field of organic electronics, these typically consist of alternating donor (D) and acceptor (A) units. As was outlined in chapter 2, when used in photovoltaic devices a key statistic of good device performance is the lifetime of the charge carrier[168]. By having the donor and acceptor units in an alternating pattern along the length of the chain one establishes a series of local charge separation states therefore increasing the possibility of hole-electron separation and increased charge carrier lifetime[5]. The choice of donor and acceptor units also allows the synthetic chemist to finely tune the HOMO and LUMO levels in order to optimise the efficiency of charge transport (and, in photovoltaic devices, to maximise light absorption) and charge separation within the

polymer molecule. In a conventional photovoltaic device created from a conjugated polymer (acting as the donor) and another molecule (typically a fullerene or derivative thereof acting as the acceptor) the only place where charge separation of the exciton can occur is where these two meet (the microscopic heterojunction). For that reason many techniques of blending the molecules[110,169,170] were developed to maximise the size and number of boundary regions.

Synthetic control over the alternating sequence of a co-polymer is achieved by utilising the differences in reactivity ratios between the monomer units in the case of radical polymerisation[171]. Alternatively, and more commonly for conjugated polymers, the selective cross-coupling of a halide and a nucleophilic substituted (such as stannyl[102], boron[103] or copper[104]) monomer using a nickel or palladium based catalyst can be used. All of the polymers in this chapter utilise the Stille coupling method with stannyl and bromide monomer substituents[98,99]. In this method, there are competing reactions between the coupling of monomer units. The catalyst is chosen so as to favour the cross-coupling of one monomer preferentially to the other and to avoid homocoupling of monomers. However, as we have seen previously and will see further in this chapter the competition between reactions is not as efficient as has always been assumed and deviations from the ideal monomer sequence can occur.

Several other synthetic strategies exist for producing conjugated polymers, for example more 'green' methods, avoiding the use of stoichiometric tin[163]. Block polymers can also be created through the engineered choice of monomer units that preferentially homopolymerise. For block polymers the opposite is true in terms of the reactivity ratios; each monomer preferentially reacts with itself rather than with the other monomer and, only once one monomer has been used up, the second is incorporated into the structure creating a block of one monomer followed by the other. Alternatively, block copolymers can be created through living radical polymerisation[172] where a chain end can be reactivated to add additional monomer units of a different structure. Finally, a random inclusion of two monomers into a sequence can be achieved by selecting monomers where the probability of homo and heteropolymerisation are approximately equal. A schematic illustration of the different types of polymer structures is shown in Figure 6.1.
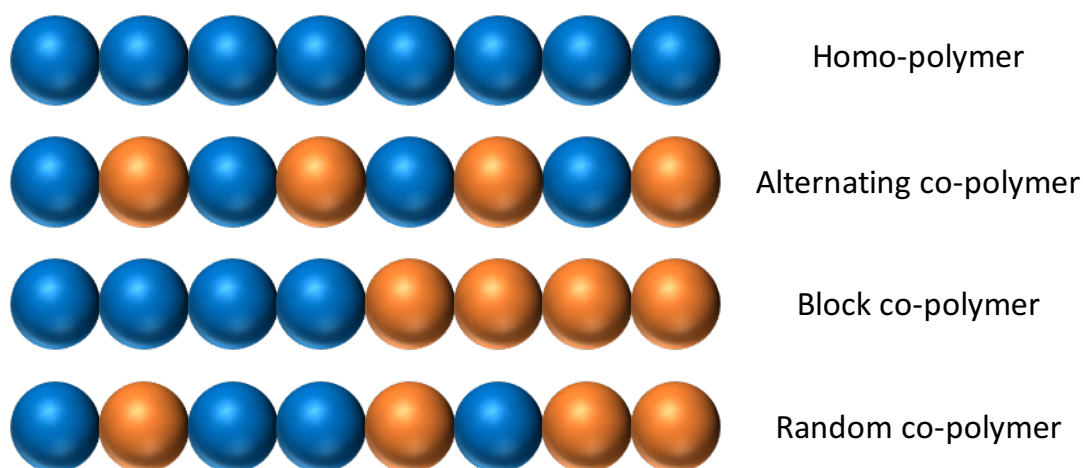
Figure 6.1 Schematic showing a representation of some of the different types of polymer composition, blue and orange balls represent different monomer chemical structures.

These methods have been developed over the last 20 years and a great degree of control has been achieved over the resulting product[5,91,98]. However, as new methods are developed, it is of paramount importance that the products can be thoroughly analysed and evaluated. This lies at the basis of developing and optimising new and efficient synthetic strategies and we see the feedback form our ESD-STM analysis as a key step in the iterative process of improvement.

As we have seen in chapter 5, the lack of high-resolution single molecule analytical techniques has meant that a great deal of information about the polymer sequence has been missed even in what were thought to be well understood synthetic methodologies[123]. We have also seen that ESD-STM provides complementary information to several existing analytical techniques about mass distribution and self-assembly.

In this chapter we aim to identify the size and monomer composition of synthetic polymer products through STM imaging. We have taken a series of oligomers and the corresponding alternating polymer and imaged them by STM. The aim was to investigate the growth mechanism of the polymer chains, whether defects occurred preferentially at a certain stage of polymer chain length growth and how the control over the number distribution of the length of the polymers changes with time.

6.2 Oligomer studies

6.2.1   Molecules being studied

Shown in Figure 6.2 are the molecules studied in this section of the thesis. The basic monomer unit is shown which consists of acceptor (A) and donor (D) subunits. The dimer consists of 2 monomer units, the tetramer of 4 units, and the hexamer of 6 units. The number of monomer units in the polymer chain is difficult to ascertain by means of standard analytical techniques – as has been previously discussed in chapter 5 – and could not be obtained by our synthetic collaborators due to coagulation of the solids at the concentration needed for SEC measurements. The growth mechanism by which the polymer chain is synthesised starts with the coupling of monomers to form a dimer, this then grows to a trimer, then to a tetramer and so on. The final length of the polymer chain is controlled by a number of factors[101] including the ratio of monomers to catalyst as well as the amount of time the reaction is allowed to run for. A final separation of products can occur via a mass separation step completed via a solvent extraction. In this work, we have chosen to study the dimer, tetramer and hexamer molecules as they represent the first steps along the synthetic pathway from monomer to polymer.
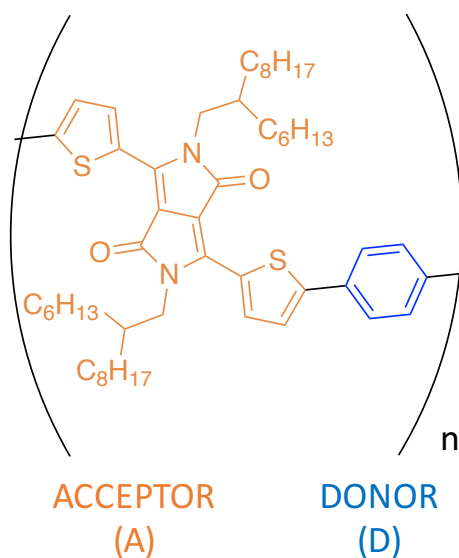
Figure 6.2 Chemical structure of dimer (n=2), tetramer (n=4), hexamer (n=6) and polymer (n>6) of poly (C_8C_6DPPT-P).

6.2.2 Dimer

The dimer was deposited (by the method outlined in section 3.2.4) for 20 minutes with a current of 50 pA onto a Au(111) surface which had been cleaned through repeated cycles of Ar^+ sputtering and subsequent annealing to 500 °C. Prior to deposition, the Au(111) was checked for cleanliness by an *in-situ* STM. The sample was then transferred to the *in-situ* STM and cooled to -153 °C. Images were acquired in constant current mode.

Figure 6.3A shows a typical STM image of the surface after deposition. The dimer can be identified as the rod-like shape which has ordered into 2D islands characterised by a rhombic unit cell with parameters a = 2.8 ± 0.1 nm, b = 2.4 ± 0.1 nm, and θ = 70 ± 2°. As this unit cell is incommensurate with the underlying Au(111) surface and the herringbone can still be seen faintly in large scale images (Figure 6.3A) the molecule-surface interaction is expected to be relatively low[173,174]. It is therefore anticipated that the stabilising force within the 2D islands is van der Waals interactions between molecules and, more specifically between, the alkyl side chains which are seen to slot together in order to maximise this interaction. This is similar to what has been seen in the previous chapter and also in a number of small molecule studies[175–177], although the alkyl chains studied here have a more complicated branched structure meaning that the simple geometric interdigitation cannot be the case here.
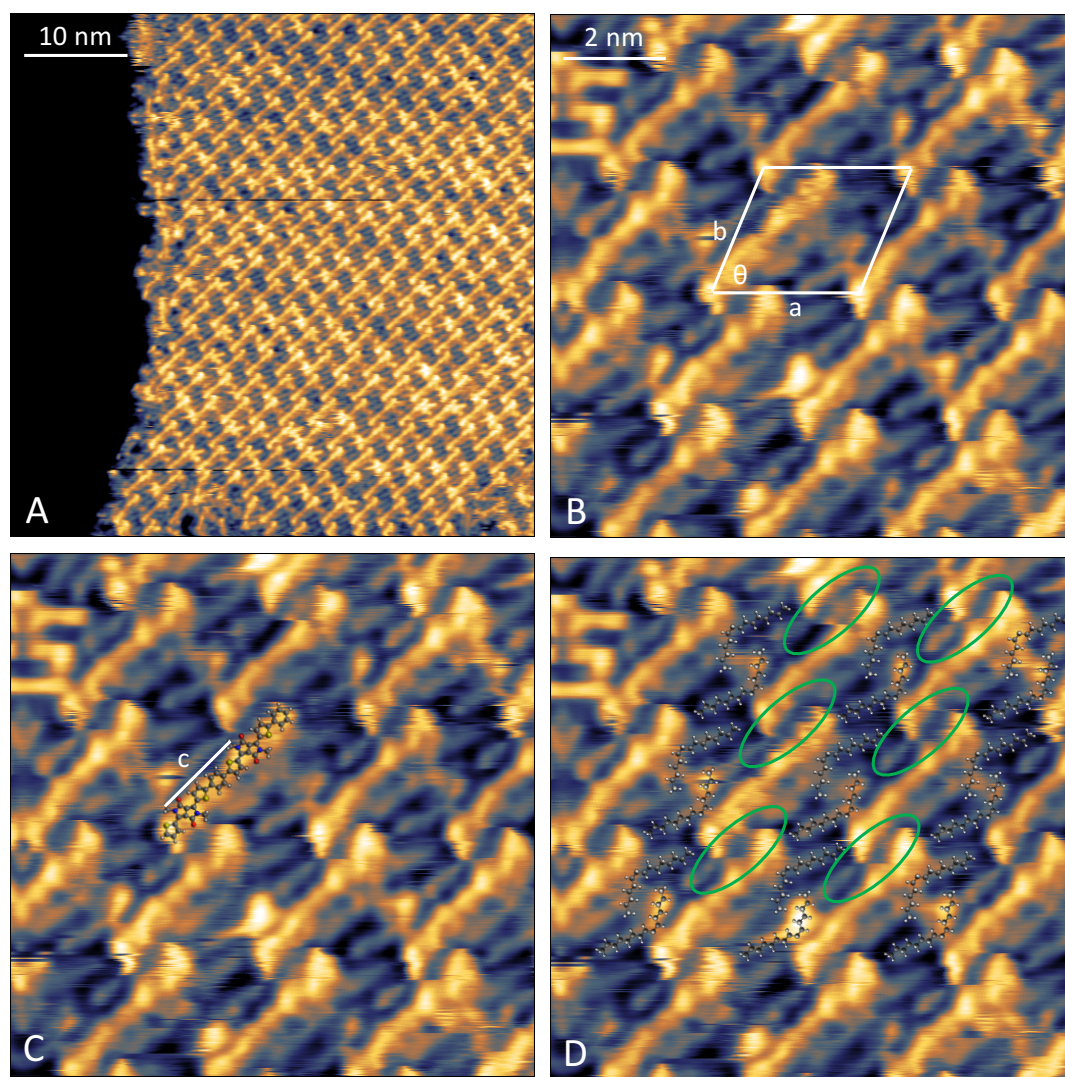
Figure 6.3 (A) STM image of dimer molecules deposited on Au (111) showing the self-assembled island. (B) Higher magnification of (A). The unit cell is explicitly indicated with parameters a = 2.8 ± 0.1 nm, b = 2.4 ± 0.1 nm, and θ = 70 ± 2°. (C) Molecular overlay of the dimer molecule. The sequential alkyl chain separation distance is indicated with the white line. (D) Molecular overlay of the C_8C_6 alkyl chains and green ovals showing expected location of second set of alkyl chains. V = 1.5V, I = 100 pA.

Both the backbone and branched alkyl side chains are visible. The backbone of the dimer is assigned as the central brighter section of the structure seen in the images and the alkyl side chains extend from this central rod. The unit cell vectors are a = 2.8 ± 0.1 nm, b = 2.4 ± 0.1 nm, θ = 70 ± 2°. A scaled and geometrically optimised molecular model of the dimer has been placed on the STM image (Figure 6.3C) showing a good size agreement between the measured structure and the molecule. This agreement can be quantitatively evaluated across the molecular islands by measuring the distance, c, between sequential alkyl side chain protrusions along the length of the backbone (which is essentially the repeat unit of the polymer chain itself) as shown in Figure

6.3. This is a useful measurement guide as the alkyl chain protrusions are easily recognisable across many tip conditions and can be used as a good indication of potential polymerisation defects such as to the inclusion of additional D or A units in a molecule. The expected distance for the molecule shown in Figure 6.1 is 1.6 nm (obtained from a geometrically optimized molecular model) and the measured value for the dimer of 1.6 ± 0.1 nm is in excellent agreement with this value (measured for 185 molecules across different sample locations).

Some alkyl side-chains can be identified as Y shaped structures protruding from the central rod. The chemical structure in Figure 6.1 shows that this is the expected shape of the branched alkyl side chains. By overlaying a scaled molecular model with the correct number of carbons it is clear to see that again the size of the alkyl chain matches with what is expected in most cases (Figure 6.3D). There is some variability in how well the model fits with the Y shape, this is likely due to the highly flexible and easily distortable nature of the alkyl group. The 3D nature of the alkyl group is also expected to cause significantly more tip-molecule interactions and there is some indication of this in the frequent noise and streaks seen in the images presented here.

The best fit with the STM images is obtained for a molecular model where the poly (C_8C_6DPPT-P) dimers form rows of parallel offset molecules and the short and long branches of the alkyl chains interact selectively, and exclusively, among each other. In particular, the C_6 branch in the alkyl chain of one molecule packs next to the C_6 branch of the dimer in the neighbouring row, while its C_8 branch interacts with the C_8 branch of the preceding dimer in the neighbouring row (see Figure 6.3B). This model explains well two out of the four alkyl chains that compose each dimer molecule (one set of two branched solubilising chains for each monomer unit). While the STM images show clear evidence for the remaining two alkyl chains, it is much more difficult to assign their exact location. Most probably this is because the remaining two alkyl chains are located in a more compact areas between the dimer backbones (see green ovals in Figure 6.3B) where they are likely not to lie flat on the surface and instead adopt an out of plane geometry.

By using higher resolution images, it is possible to identify sub-monomeric contrast and attempt to identify potential defects occurring in the monomer sequence. Acceptor units (A) can be easily located through the presence of the alkyl side chains which, by

subtraction from the remaining parts of the backbone, allows also the identification of the donor units (D). By analysing all of the acquired STM images in this manner, the ideal $(AD)_2$ sequence can always be assigned, as for example shown in Figure 6.3B. This is clearly a different manifestation of the fact that the measured alkyl chain spacing is in perfect agreement with the value of 1.6 nm, expected for ideal dimers.

It is clear from these results that the poly $(C_8C_6DPPT-P)$ dimer has been deposited intact and that there seem to be no defects in its structure, for both the length and the chemical composition of the chains. This further implies that defects must be very rare at this early stage of the synthesis of the $(C_8C_6DPPT-P)$ polymer.

6.2.3   Tetramer

The tetramer was deposited on Au(111) following the same procedure used for the dimer (previous section) but using a deposition time of 6 minutes at a current of 60 pA. Also in this case, the sample was transferred to the *in-situ* STM and cooled to -153 °C before images were acquired in constant current mode.

Figure 6.4 (A) STM image of $(C_8C_6DPPT-P)$ tetramer molecule deposited on Au (111) showing the self-assembled island. (B) Higher magnification of (A) showing the unit cell of the molecular superstructure with parameters a = 2.0 ± 0.2 nm, b = 1.6 ± 0.1 nm, and θ = 90 ± 1° and a molecular overlay. V = 2.0 V, I = 300 pA.

As was seen for the dimer, STM images reveal that the molecules have self-assembled into ordered 2D islands (Figure 6.4), although these are considerably smaller in size.

For the dimer, islands were in excess of 50 nm x 50 nm, but tetramer islands were rarely larger than 20 nm × 20 nm. The 2D islands are comprised of individual tetramer molecules – easily identifiable as the narrow rod structures with bright protrusions at regular intervals along the length – which run parallel to one another with an average separation distance of 2.0 ± 0.2 nm. The most common packing is for molecules to align their long axes parallel to one another with the alkyl chains either side interacting with the alkyl chains of neighbouring molecules appearing to slot together.

The straight backbones are reminiscent of what has been seen in chapter 5 for poly (C_{14}DPPF-F). There it was determined that the straightening of the backbone was in order to maximise the alkyl chain interdigitation, as the enhanced van der Waals interaction compensated for the energy cost associated with adopting a linear conformation. Figure 6.4 demonstrates that also for the tetramers of poly (C_8C_6DPPT-P) the alkyl chains are interacting even if the exact interdigitation motif is not as clear as with the linear alkyl chains in chapter 5. Moreover, for poly (C_{14}DPPF-F) in chapter 5 it was possible to determine the rotational conformation of the furan rings directly from the STM images, while this is not the case for the tetramer. In this case, a better way to determine the rotational conformation is to establish which molecular structure – among several different optimised structures – fit with the STM images. In Figure 6.5 we see two such possible optimised structures of the tetramer overlaid on the STM data, where structure A (parallel DPP units, panel A) provides a much better match than structure B (specular DPP units, panel B).
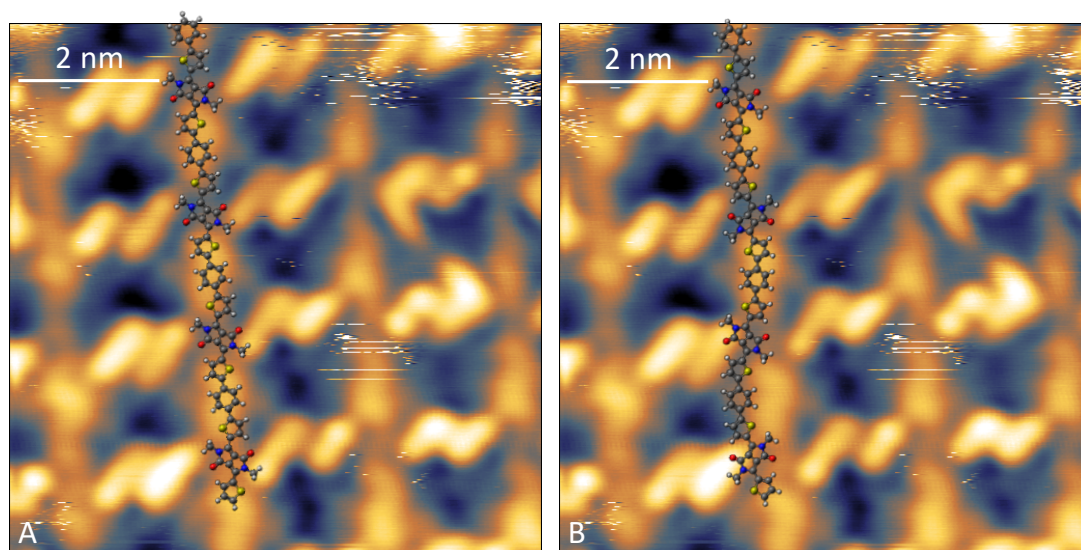
Figure 6.5 (A) Overlay of tetramer model A where all DPP units are parallel on an STM image of the molecule and (B) an overlay of tetramer model B where subsequent DPP units are specular. V = 2.0 V, I = 300 pA.

The alkyl side chains appear brighter than the backbone of the polymer and, as they are not expected to have a higher density of states we conclude that the alkyl chains have adopted a non-planar geometry. Further evidence for this comes from comparing the shape of these bright protrusions to the Y shape of the alkyl chains seen in the dimer molecule. Whereas that Y shape fits well with the branched geometry of the chains, the more elongated shape of these chains does not match directly match with it. The origin of this is not clear: the out-of-plane geometry of the tetramer alkyl chains might have been adopted in order to facilitate a greater degree of interdigitation between neighbouring molecules. At the same time, the increased length of polymer backbone could change the balance between the unfavourable distortion of alkyl chains and their favourable interdigitation.

The measured repeat unit length (1.7 ± 0.1 nm) was close to the expected value (1.6 nm), as demonstrated by the excellent match of the optimised molecular model and the STM image in Figure 6.4. This indicates that there are no defects in the expected monomer sequence of the tetramer, as a shorter repeat distance would be expected for an AA defect and a greater distance for an ADDA defect. However, several of the analysed molecules contain more than the expected 4 monomer units. A complete distribution of the number of monomers per molecule is shown in Figure 6.6 where 105 chains were analysed across several different images and regions of the sample.

Only 55% of the imaged molecules here the expected 4 monomer units length. Both longer (up to 6 units) and shorter (as low as 2 units) are present in this synthetic batch.
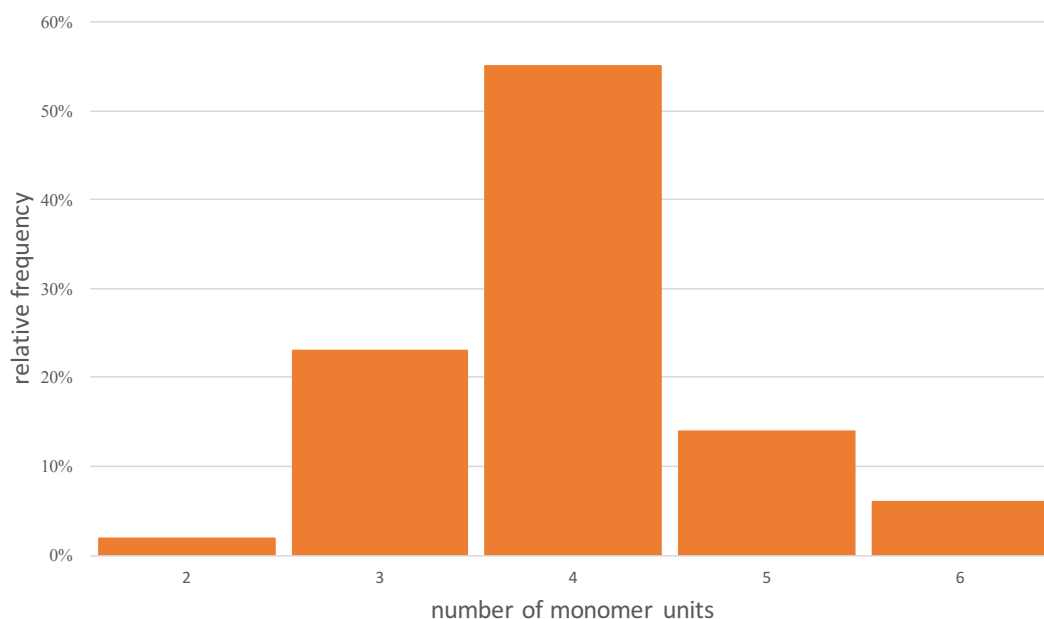
Figure 6.6 Histogram showing the distribution of oligomers lengths in the nominal (C₈C₆DPPT-P) tetramer sample expressed as a function of the number of monomer units.

This discrepancy between the nominal and actually measured chain length was not expected and had not been picked up by the traditional analytical methods available to our collaborators who synthesised the molecules. As such these results are a further demonstration of the unique analytical power of the ESD-STM technique.

The tetramer was synthesised by taking the dimer and adding further monomer units to it. As no chain length mistakes were observed in the dimer, it can be expected that the synthetic errors have occurred in the step from dimer to tetramer. This information will be useful in determining a more controlled synthetic strategy for making monodisperse tetramers (and hexamers, see next section), i.e. in precisely mastering the number of monomer units that can be added to existing oligomers. It has been shown that the length of the conjugated polymer has a dramatic effect on the band gap of the material and the device performance[178] and it is therefore very important to be able to achieve a full control over these factors.

6.2.4 Hexamer

The final oligomer studied in this chapter was the hexamer which was deposited on a Au(111) surface in a similar manner as for the dimer and the tetramer but for 15

minutes and at a current of 40 pA. Again, the sample was then then transferred to the *in-situ* STM and cooled to -153 °C, after which images were acquired in constant current mode.

The packing of the hexamer chains is similar to what was observed for the tetramer chains, with the formation of 2D ordered islands where the hexamer molecules are oriented with their long axes parallel to one another. The islands orient themselves in line with the herringbone reconstruction of the Au(111) surface (Figure 6.7A). This is in contrast to the dimer where molecule-molecule interactions appear to be of greater importance and no registry with the underlying surface was seen. The island size is smaller than what was seen for both the tetramer and dimer with an average extension of approximately 10 nm × 10 nm. A chain-chain spacing of 2.0 ± 0.1 nm is measured and is consistent with what was seen for the tetramer chains. This is not surprising as the separation between the chains is driven by the interdigitation of the alkyl side chains and these are identical for all of the oligomers studied in this chapter. Also the appearance of the alkyl chains, brighter than the polymer backbones, is analogous to the case of the tetramer, suggesting a similar raised position in order to facilitate greater packing.

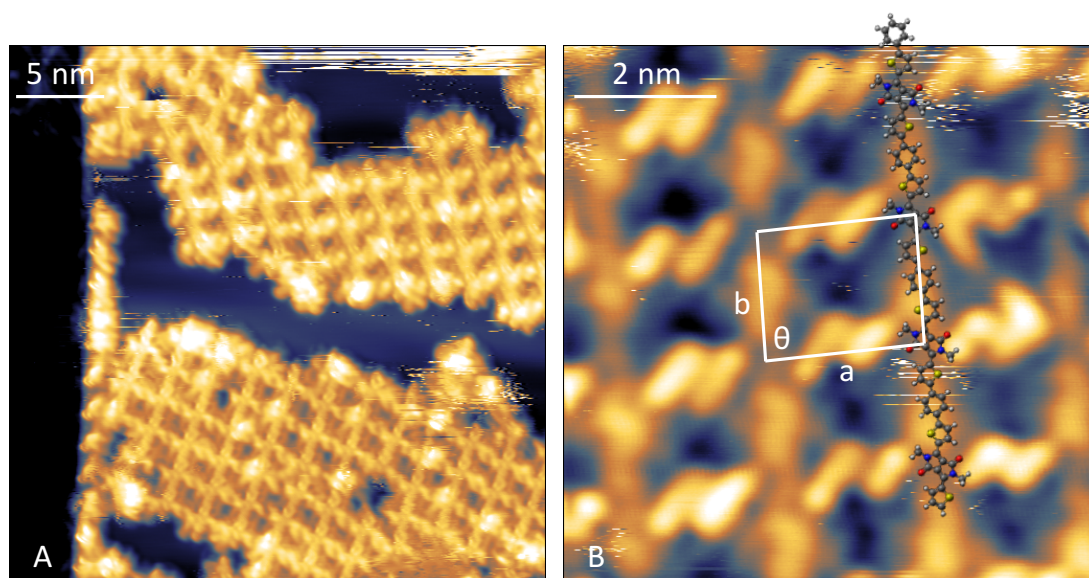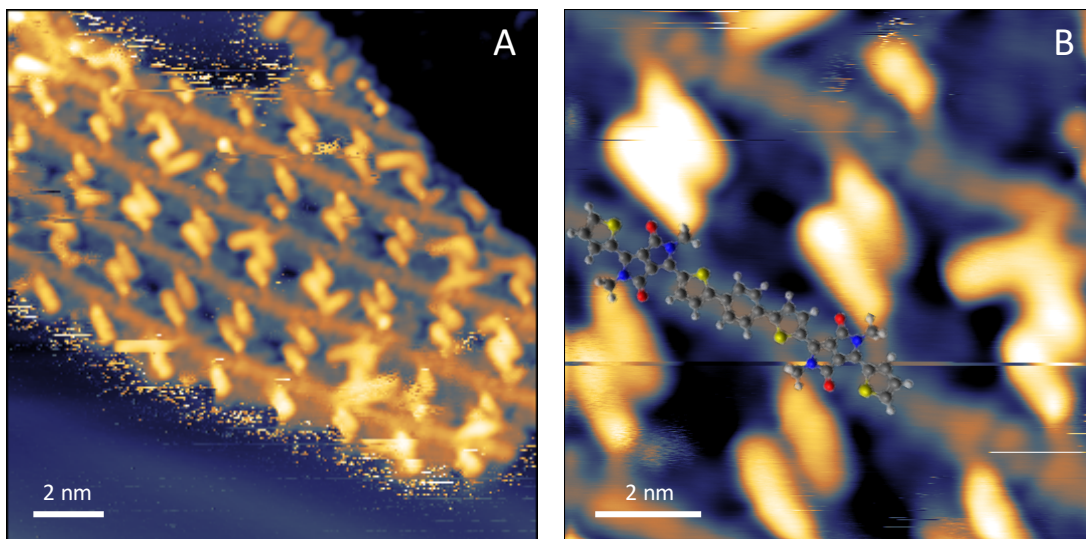*Figure 6.7 (A) STM image of hexamer molecule deposited on Au(111) showing the self-assembled island. (B) Higher magnification of hexamer assembly with a molecular model of a section of the hexamer. V = -1.5 V, I = 500 pA.*

The hexamer was synthesised by taking some remaining product of the tetramer synthesis and repeating the same steps that were carried out to make the tetramer from the dimer. It is therefore not surprising that the size distribution of the hexamer

molecules (Figure 6.8) is quite similar to that of the tetramers, if even not more disperse Only 52% of the final product is actually composed by 6 monomer units in length and 4% of the chains are twice the expected hexamer length at 12 monomer units. The presence of these longer chains and the fact we do not see chains with 9, 10 or 11 monomer units suggests that they could be the result of 2 hexamer chains coupling together. Apart from this specific observation, it is however not possible to tell whether the errors inherent in the batch of tetramer have just been translated into equivalent errors of the hexamer batch (thus implying that the second synthesis from tetramer to hexamer was error free) or if also the second synthesis suffered from further errors.
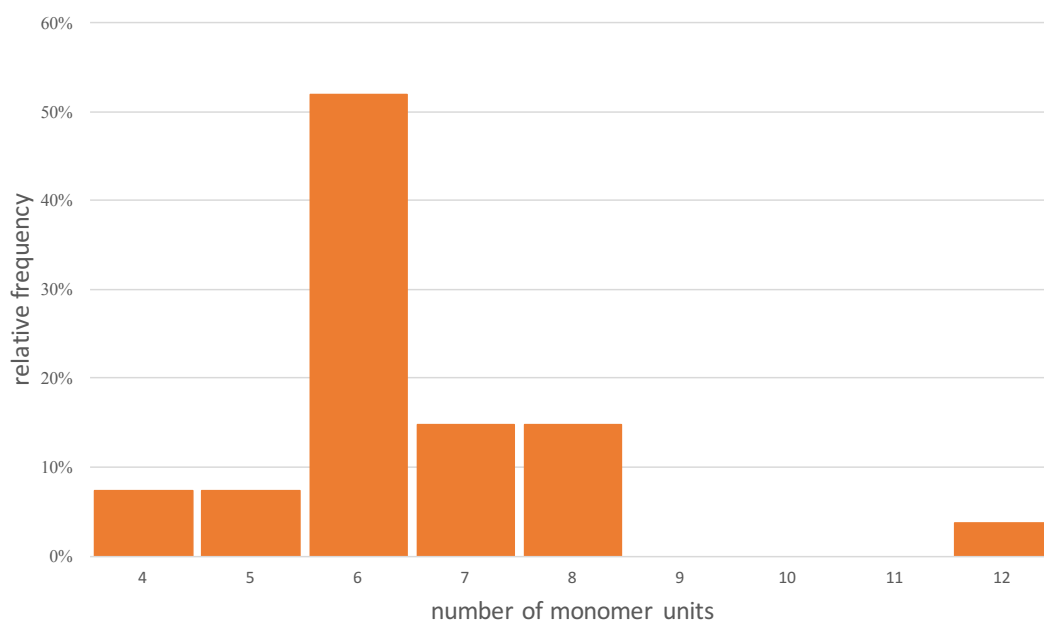
Figure 6.8 Histogram showing the distribution of hexamer chain lengths of (C_8C_6DPPT-P) expressed as a function of the number of monomer units.

Using higher resolution images, it is possible to overlay a scaled molecular model showing that, also for the hexamer molecules, the repeat unit matches the expected size (Figure 6.7), indicating any absence of defects in the oligomer sequence. This is further confirmed by the expected number of alkyl chains (2) being seen for each monomer unit and by the lack of any anomalous packing. These STM images are at high enough resolution that a sub-molecular contrast can be seen, displaying the same number and type of lobes associated with the DPP sub-units (as was seen in chapter 5). The DPP moieties lie parallel to one another, likely in order to maximise the interaction between the alkyl chains. In fact, the same argument made in chapter 5 can

be proposed here, in that parallel DPP units provide a more regular spacing of alkyl chains in order to better optimise their interdigitation. It appears from these results that the rational used in chapter 5 for linear alkyl side-chains may also be applicable to branched side-chains and that, also in this case, alkyl chain interdigitation is the driving force for polymer assembly and influences the polymer backbone conformation.

6.2.5   *Polymer*

The final molecule studied in this chapter was the (C_8C_6DPPT-P) polymer (structure displayed in Figure 6.1). It should be noted that the synthetic pathway employed for making the full polymer was different from the reaction scheme used to obtain each of the (C_8C_6DPPT-P) oligomer molecules (dimer, tetramer and hexamer), presented in the three previous sections. This is because when the oligomer reaction conditions were attempted an incomplete reaction occurred and the product was irretrievable. This made the ESD-STM analysis of the full polymer product and its comparison with the results obtained for the oligomer series, even more interesting.

The polymer was deposited on a Au(111) surface under the same conditions used for the oligomers, with a deposition time of 10 minutes and at a current of 50 pA. Also here, the sample was transferred without breaking vacuum to the STM which had been cooled to -153 °C.

Figure 6.9 shows a high coverage of the (C_8C_6DPPT-P) polymer molecule on the Au(111) substrate, the polymer can be identified by both the backbone and alkyl side chains. Besides more regular regions, where the polymer backbones are linear and parallel to one another, other regions exist where the polymers are significantly bent.
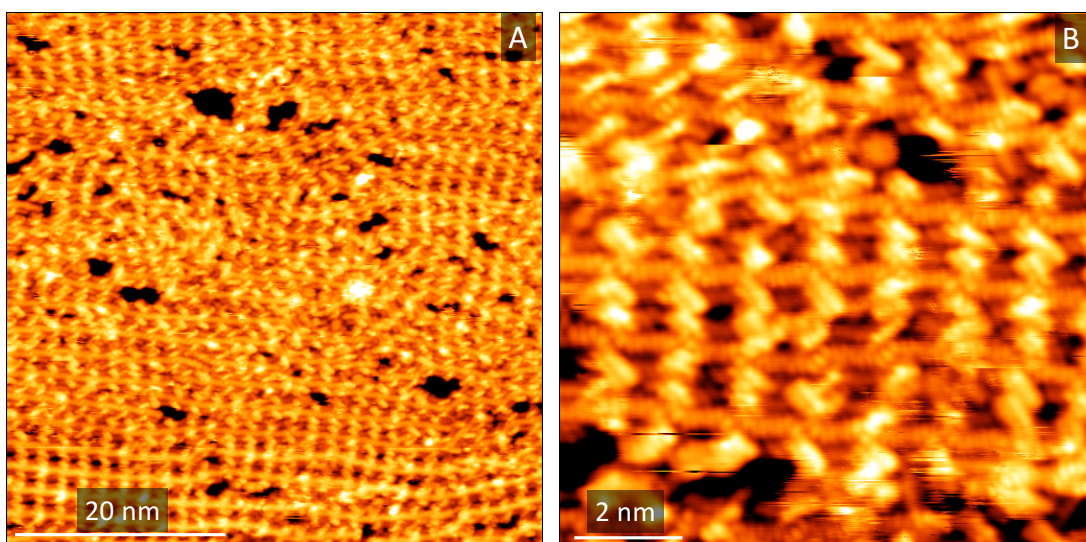
Figure 6.9 (A) STM image of a high coverage deposition of the(C_8C_6DPPT-P) polymer on Au(111) and (B) high resolution STM image of the same surface. V = -1.8 V, I = 500 pA.

These different packing regimes can be recognised in Figure 6.9 with the main difference being the degree to which the alkyl chains appear to interdigitate. There are sections that are fully interdigitated with the minimum chain-chain distance of 1.8 ± 0.1 nm and others where the backbones are the furthest apart at 2.4 ± 0.1 nm. In the lower left hand corner of Figure 6.9A, a regular packing of chains can be seen with a spacing between backbones of 2.0 ± 0.1 nm, which is analogous to the packing seen for the tetramer and hexamer molecules (Figure 6.4 and Figure 6.7).

At lower coverages chains assemble into high aspect ratio 2D islands consisting of 2-4 strands which appear much more regular than those at higher coverages (Figure 6.10) and are characterised by a chain-chain separation of 1.9 ± 0.1 nm. The islands follow the herringbone reconstruction of the Au(111) substrate and extend across different substrate terraces. The step edges are also decorated with polymer chains which have aligned themselves along them. Apart from where the chains follow the herringbone elbow sites, polymers appear completely linear at these lower coverages. This leads us to the conclusion that the irregularity of the assembly seen for higher coverage is indeed a consequence of the higher coverage and of the polymer chains not having sufficient space to re-organise into a lower energy conformation.
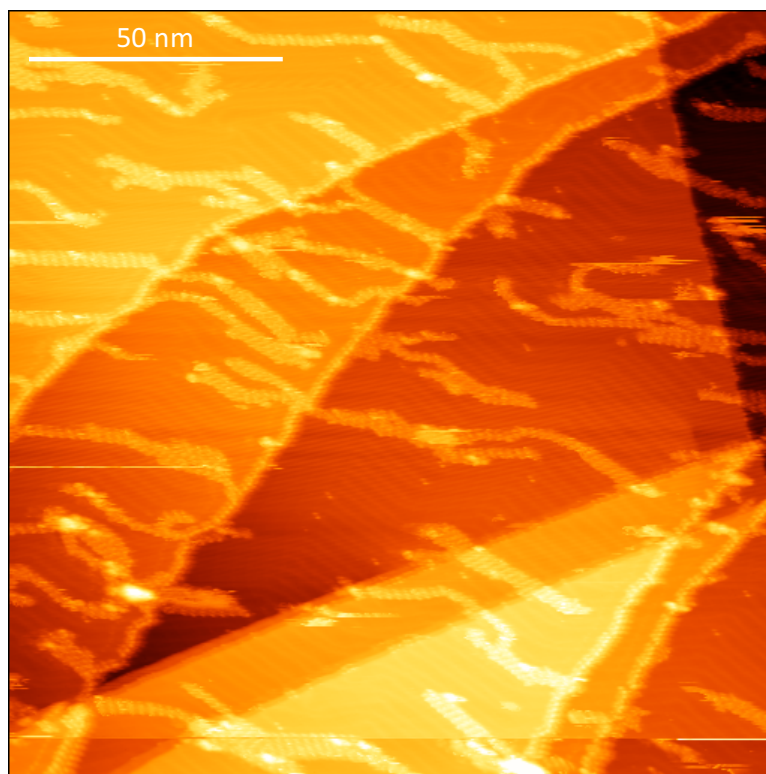
Figure 6.10 STM of the polymer molecule on Au(111) at a low coverage. V = -1.8 V, I = 500 pA.

Acquiring high resolution images at low coverages becomes significantly more difficult, because of a much higher surface mobility of the polymers, as can be seen in the centre of Figure 6.10 (a polymer has moved under the influence of the tip while being scanned). As such, the higher resolution images showing sub-monomeric contrast were exclusively acquired on the high coverage preparation.

The protrusions in Figure 6.11A can be associated with the sub-units within the repeat unit, thereby allowing to test the validity of a molecular model in much the same way as has been done previously in this thesis. However, any attempt to associate a molecular model of the polymer structure in Figure 6.1 to high-resolution STM images produces a poor fit (eg. see Figure 6.12C). Numerically, the repeat unit of the AD unit is 1.6 nm, the measured periodicity of the polymer is 2.0 ± 0.1 nm. This difference is significant and indicative of a defect in the repeat unit of the polymer. This is not an isolated instance of a defect appearing infrequently along the polymer chain but represents a fundamental difference in the chemical composition of the repeat unit.
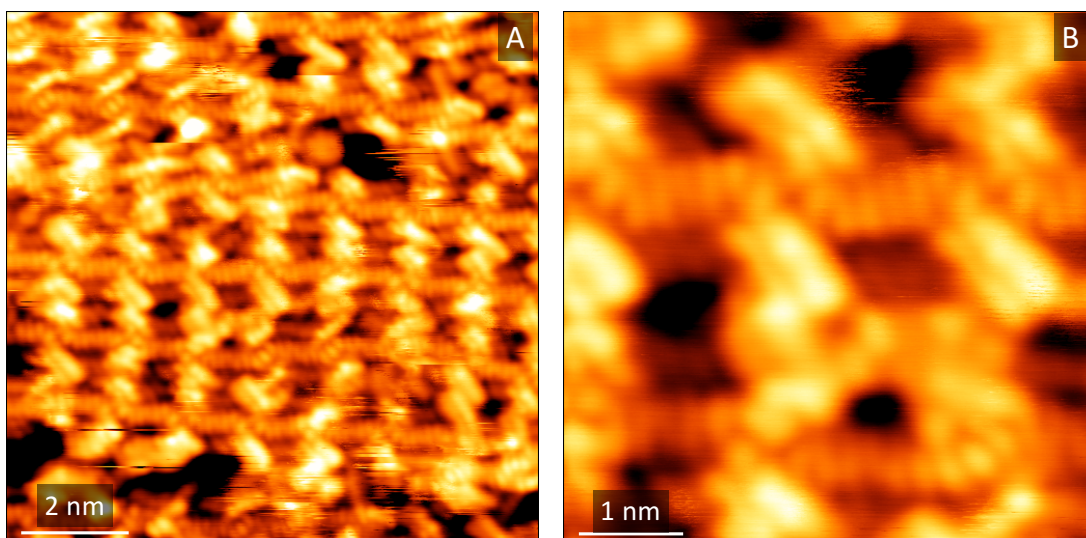
Figure 6.11 (A) STM image of high coverage polymer on Au(111) and (B) zoom in of same area shown in (A). V = -1.8 V, I = 500 pA.

We can attempt to identify the actual repeat unit by using a combination of molecular models and some 'chemical intuition'. As a starting point, we can think of two main defects that may occur in the reaction mechanism: while the ideal polymer should result from a series of heterocoupling steps, where an A monomer reacts with a D unit (or a D monomer reacts with an A unit) at the end of the growing chain, homocoupling reactions leading to AA or DD sequences might also occur, though they should be highly unlikely. While the coupling of two acceptor units would produce a shortening of the distance between alkyl chains, which is not the case, the inclusion of an additional donor unit (the same type of defect that was seen in chapter 5, ABBA defect of poly (C_{14}DPPF-F)) would result in a lengthening of the distance between subsequent alkyl side chains from 1.6 nm to 1.9 nm, which matches well with the value for this sample, 2.0 ± 0.1 nm.
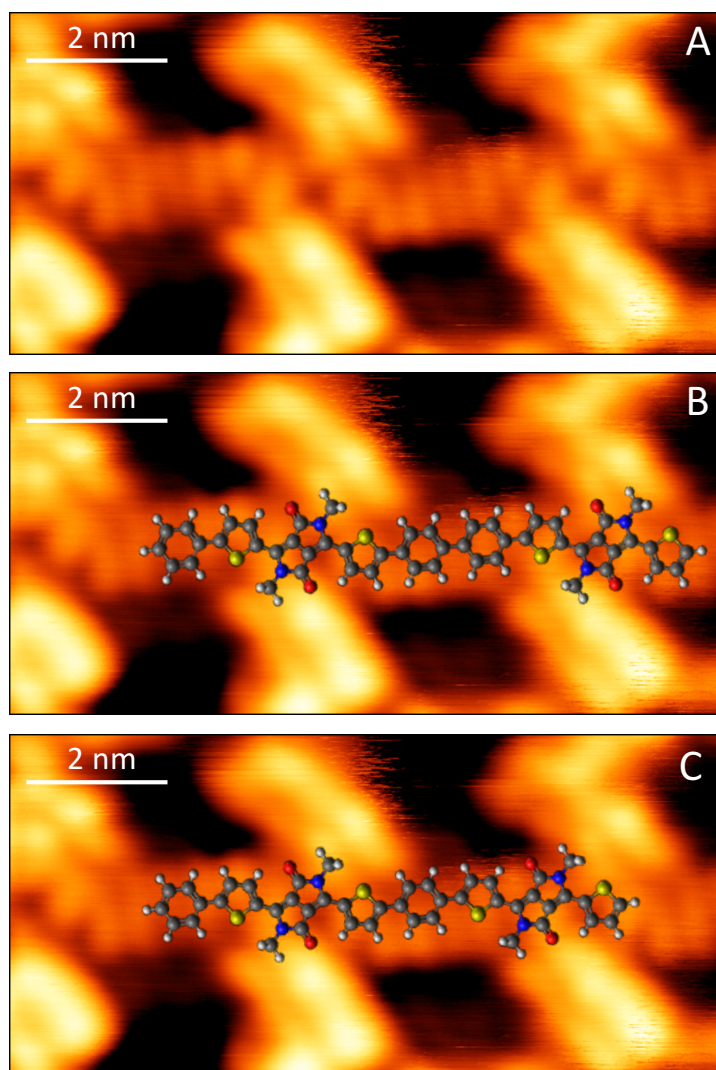
Figure 6.12 (A) High resolution STM image of the polymer with sub-molecular contrast, (B) with molecular overlay of DADDA defect sequence and (C) with expected DADA sequence. V = -1.8 V, I = 500 pA.

An overlay of a molecular model of this type of defect can be seen in Figure 6.12B and fits well with the size of the repeat unit seen in the image (the alkyl chains appear in the correct position). We therefore conclude that the actual sequence of the polymer seen in these STM images is $(ADD)_n$ and not $(AD)_n$. This is expected to have significant implications for the performance of this polymer in devices and shows again the need for high-resolution single molecule techniques for the analysis of conjugated polymers. However, it should be stated that what we image on the surface may not be representative of the initial synthesised population (as was discussed in chapter 5). For example, the defective polymer we see here may be far more soluble in our chosen electrospray solvent and therefore be incredibly over represented in the STM images we obtain.

6.3 Summary

In conclusion, we have demonstrated that synthetic procedures and existing analytical methodology are severely lacking when it comes to the analysis of conjugated polymer macromolecules. Not only have we shown that we can easily identify the chain length of oligomers and polymers but we can even identify defective chemical structures with less than perfect tip resolution. The system studied here, with branched side chains, demonstrates a more 'realistic' conjugated polymer than was used in our previous study (chapter 5) but we are still able to maintain the same degree of analytical power as was seen previously.

We believe the insights produced by these results will prove invaluable when combined with further synthetic studies in improving the design, growth and use of conjugated polymers in organic electronic and photovoltaic devices.

7 Conjugated polymer microstructure determined by alkyl side-chain interdigitation

7.1 Investigating the effects of monomer composition on the local packing of conjugated polymers

The molecules provided in this section of the thesis have been synthesised by Dr Anastasia Leventis, Professor Hugo Bronstein, and Professor Iain McCulloch.

The structure of conjugated polymer thin films has been extensively studied as it is one of the most important factors controlling the performance of devices fabricated from these materials. Alkyl side-chains, originally introduced to improve the processability of otherwise insoluble molecules, have been shown to play an essential role in controlling the interaction between individual polymer chains and in determining the three-dimensional (3D) ordering, and the electronic properties of conjugated polymer thin films. In particular, it has been proposed that maximisation of side-chain interdigitation is the key driving force controlling the microstructure of many crystalline conjugated polymers. By combining electrospray deposition and scanning tunnelling microscopy, we show that two-dimensional (2D) polymer monolayers deposited on inert metallic surfaces reproduce well the 3D packing of π-stacked lamellar thin films and can thus be used as model systems for studying their solid state microstructure. On this basis, we investigate the 2D assembly of a series of conjugated polymers with varying backbone chemical compositions to explore the range of applicability of a simple model for linear alkyl side-chain interdigitation based on the maximisation of van der Waals interactions.

Conjugated polymer side-chains are known to significantly interact with one another and to significantly influence the microstructure of polymer thin films[123,179–182]. In particular, it has been shown that the solid state phase of a number of conjugated polymer molecules is characterised by the interdigitation of their side-chains (both for linear and branched side-chain structures). The level of interdigitation typically correlates with the degree of crystallinity, the long range order and the extent of π-stacking in the thin film, thereby dictating its optoelectronic properties. For this reason there is a great deal of interest in the field of side-chain engineering[183–185], essentially trying to direct the structure of a polymer thin film through the selective choice of side-chain substituents. This can range from the most simple interdigitation through to more complex hydrogen bonding motifs. Even though a significant amount of research has been invested in looking at the effects of different side-chain

morphologies and chemistries, a molecular scale understanding capable of predicting how side-chains influence the polymer assembly is largely missing even for the simplest interdigitation of alkyl chains.

It is well-known that the interaction of the alkyl side-chains has a significant impact on the polymer conformation and that, together with π-stacking, it controls the growth of (locally) crystalline thin films for conjugated polymer samples. Several studies have also demonstrated that this high degree of order is accompanied by high charge transport properties[135,186], making it the basis for the design of polymer materials with increasing charge carrier mobilities. However, very few studies exist where the precise chemical structure of a monomer unit is linked to polymer crystallisation and almost nothing is known about how defects might affect the assembly of films of conjugated polymers. One such available investigation is the 2007 work by R.J. Kline et al.[186] who showed that the degree of interdigitation in the thin films formed by three selected polythiophenes (poly(3-hexylthiophene), P3HT; poly[5,5′-bis(3-alkyl-2-thienyl)-2,2′-bithiophene], pQT; and poly(2,5-bis(3-quaterdecylthiophene-2-yl)-thieno[3,2-b]thiophene, pBTTT), is determined by the attachment density of their linear alkyl side-chains. Whether interdigitation occurs (and to what extent) could be explained through a simple geometric model and verified by means of X-ray diffraction (XRD), infrared spectroscopy (IR), and atomic force microscopy (AFM) measurements. Essentially, there is an enthalpic gain from the van der Waals interaction of the alkane chains, and this is maximised when the chains pack together at a close packed density corresponding to the density of the analogous aliphatic linear hydrocarbons in their crystal structure. Additionally, it was demonstrated that in thin films of the three examined polythiophenes, this optimal density is adopted by the alkyl chains through changes in their tilt angle with respect to the polymer backbone and through interdigitation.

In the present work, we perform a combined electrospray deposition (ESD) and scanning tunnelling microscopy (STM) study to investigate the assembly of a number of polythiophenes and diketopyrrolopyrrole (DPP) polymer monolayers at the molecular scale. By directly visualising the interdigitation and the alkyl chain tilt angle of monolayers of pBTTT and comparing them with the results reported by R.J. Kline et al.[186], we first show that two-dimensional (2D) monolayers of conjugated polymers can be an ideal model systems for studying the three-dimensional (3D) packing of

their thin films. We then analyse three further DPP-based polymers, revealing the interactions between individual polymer strands and the arrangements of their alkyl chains. Our results overcome the indirectness and inherent averaging of previously used analytical techniques, and unambiguously demonstrate the wide applicability but also the limits of a model of alkyl chain interdigitation based on the minimisation of van der Waals contact potential.

7.2 Results

Figure 7.1B shows a representative STM image of a monolayer of pBTTT-C_{14} deposited on a Ag(111) substrate by ESD. This technique has been used to prepare all of the polymer samples in this work and has been described in details elsewhere[123]. Briefly, it allows the fabrication of (sub-)monolayer coverages of complex polymer molecules on atomically clean and flat substrates under vacuum conditions; these samples can then be analysed *in-situ* by high resolution surface science methods[17,144]. Both the backbone and alkane side-chains of individual pBTTT-C_{14} polymer strands are clearly visible and it is immediately obvious that interdigitation between parallel strands is occurring. The repeat units appear as a straight segments in a sort of staircase structure and are connected to each other at an angle of about 120° (Figure 7.1C), in accordance with the molecular structure of pBTTT (Figure 7.1A). Their separation along the polymer backbone is measured to be 1.36 ± 0.06 nm, showing an excellent agreement with the value of 1.36 nm expected from a force field optimised molecular model. Each repeat unit is connected to two straight segments – representing the alkyl side-chains – that adopt a well-defined angle of 44 ± 2° with respect to the axis of the polymer backbone; this is consistent all over the monolayer except for very small regions where a different, less dense packing is seen. Accordingly, for the vast majority of the sample the separation between adjacent polymer backbones is equal to 2.1 ± 0.1 nm, when measured perpendicular to the backbone themselves.
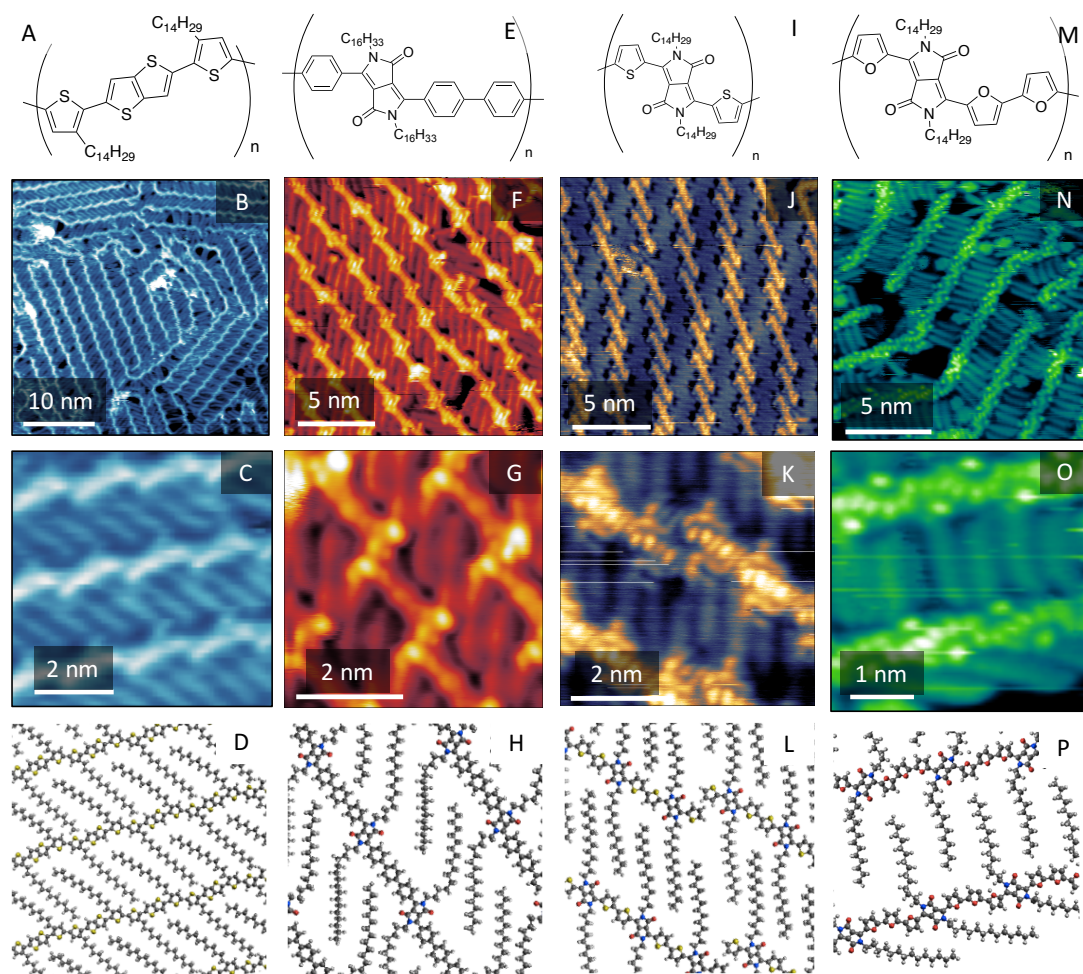
Figure 7.1 Chemical structures, STM images and molecular models of pBTTT, poly (C$_{16}$DPPP-P), poly (C$_{14}$DPP-T), poly (C$_{14}$DPPF-F). (A), (E), (I) and (M) show the chemical structures of pBTTT, poly (C$_{16}$DPPP-P), poly (C$_{14}$DPP-T) and poly (C$_{14}$DPPF-F) respectively. (B) and (C) show STM images of pBTTT on Ag(111) (V = -1.5V, I = 200 pA). (F) and (G) show STM images of poly (C$_{16}$DPPP-P) on Au(111) (V = -1.0V, I = 100 pA). (J) and (K) show STM images of poly (C$_{14}$DPP-T) on Au(111) (V = -2.0V, I = 200 pA). (N) and (O) show STM images of poly (C$_{14}$DPPF-F) on Au(111) (V = -1.5V, I = 300 pA). (D), (H), (L) and (P) demonstrate the expected packing of polymer chains for monolayer coverages of pBTTT, poly (C$_{16}$DPPP-P), poly (C$_{14}$DPPT-T) and poly (C$_{14}$DPPF-F) respectively.

These results are in excellent agreement with the structural parameters reported by R.J. Kline et al. for highly ordered thin films of the same polymer[186]. By combining XRD and AFM measurements, these authors determined that the crystalline regions of pBTTT-C$_{14}$ are characterised by a high degree of side-chain interdigitation, with and a tilt angle of 44° and a lamellar spacing (3D analogous to the backbone-backbone separation, see below) of 2.15 nm[187,188].

While these strong similarities could, at first sight, appear surprising, a precise analysis of the 3D crystalline structure of conjugated polymers allows to rationalise the relation

between the morphological characteristics of 2D monolayers and 3D thin films of these materials. Crystalline domains of conjugated polymers are characterised by π-stacking of their aromatic backbones. The π-stacking distance of well-packed polymers is typically around 0.38 nm, a value that is essentially independent of the specific material[186]. This causes a largely planar conformation of the individual polymeric strands and drives their organisation into extended lamellae (Figure 7.2A). In particular for linear alkyl side-chains, these lamellae further assemble in the perpendicular direction through the (complete or partial) interdigitation of their side-chains, determined by whether there is sufficient free volume between side chains (Figure 7.2B). As such, the 3D crystalline regions of conjugated polymers can be seen as a layered material constituted of sheets of planar interdigitated polymer strands (Figure 7.2C) that are kept together by π-stacking.
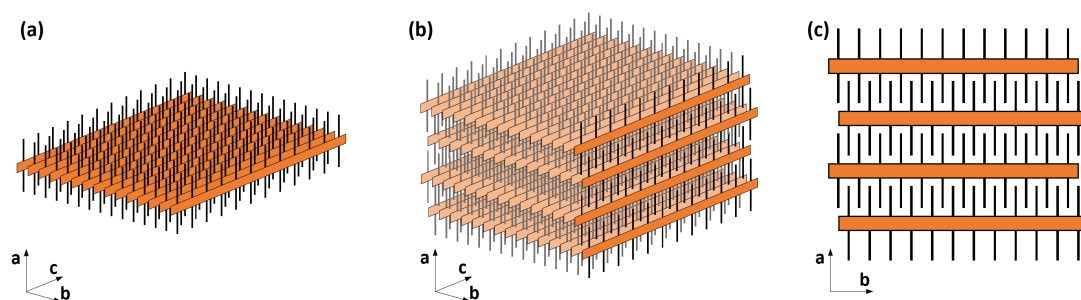
Figure 7.2 Schematic representation of the packing of crystalline films of conjugated polymers. (a) Lamella stabilised by π-stacking of the aromatic backbones. (b) Assembly of lamellae into 3D film through interdigitation of the solubilising alkyl chains. This structure can also be seen as the π-stacking of planes of interdigitated polymers (highlighted). (c) Individual 2D plane of interdigitated polymer strands.

When deposited by ESD on an atomically clean and flat metallic surface under vacuum conditions, conjugated polymers adopt a face-on geometry in order to maximise their interaction with the substrate. For relatively inert substrates such as Au(111) or Ag(111), this interaction is however not particularly strong and is probably comparable to the π-π stacking interaction in the 3D thin films. The inherently 2D monolayers of ESD-deposited polymers are thus analogous to the planes of interdigitated polymer strands that constitute the 3D films (Figure 7.2C); it is therefore not surprising that their assembly is characterised by similar features. In particular, the case of pBTTT-C_{14} discussed above, demonstrates a qualitative – the interdigitation between alkyl chains – and quantitative – tilt angle and backbone-backbone separation/lamellar spacing – analogy between these 2D and 3D structures. As such,

2D monolayers of conjugated polymers deposited by ESD on inert metallic surfaces can be used as model systems for studying the 3D crystalline packing of these materials and thus represent a valuable tool to determine their solid state microstructure.

Based on this, we studied the 2D assembly of three further polymers to demonstrate the general validity of the simple geometric model introduced by R.J. Kline et al.[186], capable of predicting the crystalline packing of conjugated polymers with linear alkyl side-chain. For planar polymer strands with a fixed π-stacking distance of 0.38 nm[186], the optimal alkyl chain areal density, ρ_{opt} = 5.4×10^{14} cm^{-2}, (i.e. that of crystalline polyethylene) corresponds to an optimal distance between the alkyl chains, d_{opt} = 0.49 nm. For a polymer with a spacing c of side-chains along the backbone, this optimal distance can be achieved by either tilting of the alkyl chains at an angle θ_{NI} (Figure 7.3A) or by interdigitation and tilting of the alkyl chains at an angle θ_I (Figure 7.3A). This can be expressed in the following equations:

$$\theta_{NI} = cos^{-1}\left(\frac{d_{opt}}{c}\right)$$

Equation 7.1

$$\theta_I = cos^{-1}\left(\frac{2d_{opt}}{c}\right)$$

Equation 7.2

For example, in the case of pBTTT, the spacing of side-chains along the backbone is c = 1.36 nm which, in the case of interdigitation, results in an expected tilt angle $\theta_{I,\text{pBTTT}}$ = 44° which is in perfect agreement with the values measured by STM in the 2D monolayers and by XRD in the 3D thin films.
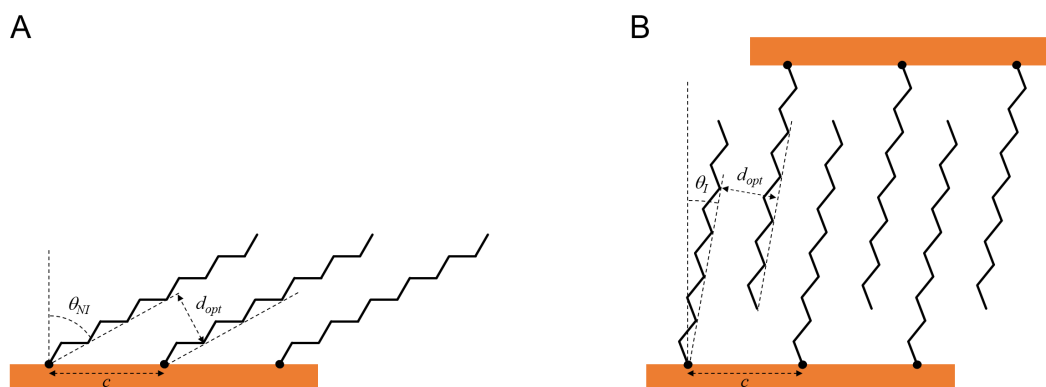
Figure 7.3 Schematic representation of the tilt angle adopted by the alkyl side-chains of conjugated polymers in order to maximise van der Waals interactions. (A) non-interdigitated and (B) interdigitated case.

The other three conjugated polymers studied in this work are DPP donor-acceptor polymers with different aryl substituents. Poly $(C_{16}DPPP-P)$[189] (Figure 7.1E) consists of an acceptor unit – containing a central DPP ring which is flanked by two phenyl rings – and a donor unit which is a phenyl ring. Figure 7.1F shows an STM image of a monolayer of the poly $(C_{16}DPPP-P)$ molecule deposited by ESD on a Au(111) substrate. Both the backbone of the polymer and the alkyl side-chains can be clearly seen and it is evident that they are highly interdigitated. In higher magnification images (Figure 7.1G), the DPP moieties appear as four protrusions (two brighter external and two dimmer internal), while the three phenyl rings form a straight segment oriented about 120° to the main axis of the DPP unit. Similarly to the case of pBTTT, this gives the poly $(C_{16}DPPP-P)$ backbone a staircase-like appearance with a measured repeat unit distance of 1.82 ± 0.03 nm, which fits extremely well with the predicted value of 1.8 nm obtained from a force field optimised molecular model of a pentamer of $C_{16}DPPP-P$. High resolution STM images as that shown in Figure 7.1G also allow an accurate measurement of the alkyl chain tilt angle, which results in 57 ± 1°. This is in excellent agreement with the value predicted by the model of R.J. Kline et al.[186], $\theta_{I,\text{poly(C16DPPP-P)}} = 58°$.

Poly $(C_{14}DPP-T)$ is a further example of a DPP based polymer, where each acceptor DPP unit is flanked by one thiophene ring on each side (Figure 7.1I). Figure 7.1J shows an STM image of the polymer deposited by ESD on a Au(111) substrate. Again, both the backbone and the alkane side chains are easily recognisable and an

interdigitated assembly is clearly seen. At variance with both pBTTT and poly (C_{16}DPPP-P), the poly (C_{14}DPP-T) sample is comprised almost exclusively of short chain oligomers, with a maximum of four repeat units in any given strand. These orient in a head-to-tail fashion with a slight overlap between the end of one chain and the start of the next. Despite the reduced length of the polymer strands, interdigitation is clearly still the driving force of assembly, resulting in individual chains being oriented parallel to each other. Figure 7.1K displays a higher resolution STM image of poly (C_{14}DPP-T), with the DPP units showing a similar contrast to what observed in poly (C_{16}DPPP-P), while the thiophene rings appear as single bright protrusions. Using these higher resolution images, it is possible to measure a repeat unit distance of 1.27 $\pm$ 0.02 nm – matching well with the value of 1.2 nm obtained from force field optimised oligomer models – and an alkyl chain tilt angle of 32 $\pm$ 1°, which is very close to the predicted angle $\theta_{I,\text{poly(C14DPPT)}} = 34°$.

The last polymer analysed was poly (C_{14}DPPF-F), which has a repeat unit composed of DPP and three furan rings (Figure 7.1M) and which was extensively studied in our earlier work[123]. Similarly to the previous cases, STM images of poly (C_{14}DPPF-F) deposited on Au(111) show highly interdigitated polymer strands with clearly recognisable backbones and linear side-chains (Figure 7.1N). Due to the lower overall surface coverage, it was possible to image also the edges of the molecular islands, revealing a significant difference between the orientation of interdigitated and non-interdigitated alkyl side-chains (Figure 7.1O). A statistical analysis shows that the angle formed with the polymer backbone is 67 $\pm$ 2° for non-interdigitated chains and 4 $\pm$ 2° for interdigitated ones. While the former value agrees well with the predicted angle $\theta_{NI,\text{poly(C14DPPF-F)}} = 70°$, the latter is very different from what obtained from the model, $\theta_{I,\text{poly(C14DPPF-F)}} = 46°$.

The comparison between the structural parameters obtained by STM for ESD-deposited polymer monolayers and those predicted by the assembly model of Kline et al.[186] is summarised in Table 7.1, showing that all of the predicted and measured angles are within a few degrees of one another, except for the interdigitated poly (C_{14}DPPF-F). The precise reason why only this last polymer does not follow the simple model for the maximisation of van der Waals interactions is not known but a few possibilities are considered. Firstly, as we have previously reported[123], poly (C_{14}DPPF-F) contains homocoupling defects in the monomer sequence and we demonstrated that they

disrupt the orientation of individual repeat units within the backbone, generating gaps in the interdigitation of the side-chains. We speculate that these gaps could alter the energetics of interaction between polymer chains and consequently modify the preferred tilt angle of the alkyl chains.

Table 7.1 Values showing the match between measured and predicted alkyl chain angles for the polymers studied here.

Polymer	Repeat unit length / nm	Predicted angle / degrees	Measured angle / degrees	I or NI
pBTTT	1.36	44	44 ± 2	I
poly (C_{14}DPP-T)	1.17	34	32 ± 1	I
poly (C_{16}DPPP-P)	1.82	58	57 ± 1	I
poly (C_{14}DPPF-F)	1.40	46	4 ± 2	I
poly (C_{14}DPPF-F)	1.40	70	67 ± 2	NI

Another possible cause might be found in the monomer composition of poly (C_{14}DPPF-F). The schematic representation of the polymer chain shown in Figure 7.3, assumes that the backbones are colinear. This is probably a good approximation for pBTTT and poly (C_{14}DPP-T) because their repeat units have an even number of thiophene rings (Figure 7.1A and I), which allows their trans orientation and an overall linear configuration for the backbone. The same approximation is probably still valid for poly (C_{16}DPPP-P) because, even if successive DPP units are separated by an odd number of aryls, these are phenyl rings connected to each other in the para position, resulting, again, in an overall linear backbone (Figure 7.1E). On the contrary, each repeat unit of poly (C_{14}DPPF-F) has an odd number of furan rings, implying that a straight backbone can only be achieved if each furan ring is trans with respect to its neighbour. While this is indeed the lowest energy configuration of an individual poly (C_{14}DPPF-F) strand, it is also highly disadvantageous for intermolecular interactions because it implies an alternating orientation of the DPP moieties and thus alternating large and small separations between the alkyl chains. As a consequence, when interacting with one another through their side-chains, polymer strands of poly (C_{14}DPPF-F) adopt a conformation where, in each repeat unit, two successive furans are cis to each other, and two are trans (Figure 7.1P). If isolated, individual polymer strands would be curved in this conformation but, within molecular islands, they become colinear because the energetic cost of straightening is compensated by the better alkyl-alkyl chain interactions[123]. This analysis shows that evaluating the energetic balance in the assembly of poly(C_{14}DPPF-F) is more complex than just

maximising the van der Waals interaction between its alkyl side-chains. As a consequence, it is not surprising that the simple representation shown in Figure 7.3 might not hold for this polymer and that a more detailed description, probably a fully atomistic model, is needed to properly rationalise the assembly of this polymer. We expect this to be true for a much wider family of DPP-based polymers that include an odd number of planar five-membered ring in their repeat units.

Finally, it should be noted that the non-interdigitated sections of poly (C_{14}DPPF-F) have an alkyl chain tilt angle which is quite close to the predicted one. This suggests that if the energetics is only dictated by the interaction between successive alkyl chains on the same side of a polymer strand (i.e. if interdigitation is not involved), maximisation of the van der Waals contact is the only relevant driving force.

7.3 Summary

In conclusion, we have shown that besides being a unique technique for determining the exact monomer sequence of conjugated polymers[123], ESD-STM is also extremely useful for probing their local microstructure. In particular, we compared our ESD-STM data with previous XRD measurements of pBTTT – a prototypical molecular component of organic electronic and photovoltaic applications – demonstrating a close qualitative and quantitative correspondence between the structural properties of 2D monolayers and those of the crystalline regions of 3D thin films. The fact that 2D monolayers are a good model system for studying the 3D microstructure of conjugated polymers, was then used to extend the investigation to a family of acceptor-donor polymers based on the DPP electron acceptor moiety. By analysing at the individual molecular scale the separation between polymer strands and the arrangement and interdigitation of alkyl chains, we demonstrated the wide applicability of a simple model of polymer assembly based on the optimisation of van der Waals interactions between solubilising alkyl side-chains. However, we also recognised its limitations, identifying the monomer compositions that require a higher-level theoretical description.

This work represents the first example of a new way of studying the solid state microstructure of conjugated polymers. We expect that, by overcoming the indirectness and inherent averaging of previously used analytical techniques, this new approach might be able to significantly contribute to establish new structure-function

relationships and, in particular, to determine how the monomer chemical composition and sequence affects the polymer assembly.

8 Conclusions and outlook

8.1 Summary of results

8.1.1 SEISMIC

In this work we have shown the development, construction and characterisation of a high flux electrospray ion beam deposition source which has been coupled to a variable temperature STM. SEISMIC represents an evolution of current ESIBD equipment[14–16], demonstrating a greater ion flux and additional deposition stages which introduce enhanced capabilities for surface science of thermally labile or otherwise fragile molecules. Specifically, we have shown a new hexapole design which can transmit ions across a number of pressure regimes with minimal losses, a compact and modular system which can be upgraded with new equipment or trialled with improved designs. Several new avenues have been opened through the construction of SEISMIC. For example, the chemical modification of boron doped diamond, where one could controllably modify the surface of a boron doped diamond electrode through reactive landing of a precursor molecule. Another area of study is through covalent organic frameworks. Many current synthetic strategies involve depositing the two precursor molecules on a surface and annealing them, however this often results in disordered or small domain sizes. Using SEISMIC it would be possible to seed the growth of these frameworks in the solution phase where mistakes in bonding are more easily reversed and then to deposit large sheets of covalent organic frameworks, which may aid in seeding the growth of higher ordered domains. We believe these represent just a few of the many experiments which are now possible using SEISMIC.

8.1.2 Conjugated polymer studies

We have also demonstrated the capabilities of the ESD-STM technique to probe the sequence, chain length and local packing of a range of conjugated polymer molecules. Conjugated polymers represent one of the most useful and studied subsections of macromolecules and in this thesis we have shown the use of ESD-STM as a tool to probe the key characteristics of these molecules which affect their performance in devices. In chapter 5, we showed that by depositing a polymer onto an atomically clean substrate in HV we are able to obtain images that allow for the direct sequencing of a conjugated polymer backbone. Not only this, but we were able to identify the nature, frequency and type of defect that was present within the molecules. Further, in chapter 6 we have demonstrated the molecular identification of a number of

146

conjugated oligomers and polymers. The results showed that the control over the length of the polymer chains during the synthetic procedure was far from ideal and that the repeat unit present in the polymer molecule was different of that seen in the oligomer molecules. Finally, in chapter 7 we have investigated the local packing of polymer chains directed by the alkane side chains and shown that the 2D monolayers we have studied can be directly compared to 3D thin films which have been studied by complementary techniques. These three chapters which have investigated the monomer sequence, chain length, growth mechanism and local packing of conjugated polymers demonstrates that ESD-STM is a versatile technique which can be used to investigate a wide variety of aspects of conjugated polymers and their assembly. The areas we have chosen to investigate in this work represent some of the most important in terms of device performance. We believe the results we have found here will go some way towards helping organic chemists in iterating on their synthetic methodology and creating more well defined polymer structures with the ultimate aim of achievement higher device efficiencies. Indeed, in some areas the results presented here are already helping our collaborators in improving their synthetic design strategies. Further, the aspects we have investigated here are just the beginning. We believe future experiments involving imaging of polymers with ncAFM, conductance measurements through single polymer chains and scanning tunnelling spectroscopy measurements could all add to the ongoing research efforts directed towards creating polymers with greater device performance.

Appendicies

Appendix A – List of publications

The following is a list of artiles resulting from work performed entirtely or partly within this thesis that has been or will be published:

D. A. Warr, L. M. A. Perdigão, H. Pinfold, J. Blohm, D. Stringer, A. Leventis, H. Bronstein, A. Troisi, G. Costantini, Sequencing conjugated polymers by eye. *Sci. Adv.,* **4,** eaas9543 (2018).

D. A. Warr, T. Moriarty, L. M. A. Perdigão, A. Leventis, D. Stringer, C. Jellet, I. McCulloch, H. Bronstein, G. Costantini, Predicting and visulaising the alkane interdigitation angle of conjugated polymers, *in preparation.*

A. Leventis, D. A. Warr, J. Tully, L. M. A. Perdigão, G. Costantini, J. Nelson, H. Bronstein, Title to be determined, *in preparation.*

D. A. Warr, L. M. A. Perdigão, J. Blohm, H. Pinfold, A. W. Colburn, M. Barrow, G. Costantini, A high flux ion deposition instrument for nanoscale imaging studies of thermally labile molecules, *in preparation.*

P.J. Blowey, L.A. Rochford, D.A. Duncan, D.A. Warr, T.-L. Lee, D.P. Woodruff, G. Costantini, Probing the interplay between geometric and electronic structure in a two-dimensional K-TCNQ charge transfer network, *Faraday Discussions*, **204**, (2017), 97-110.

A. D. Pia, S. Lisi, O. D. Luca, D. A. Warr, J. Lawrence, M. Otrokov, Z. Aliev, E. Chulkov, R. Agostino, A. Arnau, M. Papagno, G. Costantini, TCNQ Physisorption on the Bi_2Se_3 Topological Insulator, *ChemPhysChem,* 10.1002/cphc.201800259, (2018).

P. J. Blowey, S. Velari, L. A. Rochford, D. A. Duncan, D. A. Warr, T-L. Lee, A. De Vita, G. Costantini, D. P. Woodruff, Re-evaluating how charge transfer modifies the conformation of adsorbed molecules, *Nanoscale,* **10**, (2018), 14984-14992.

P.J. Blowey, R.J. Maurer, L.A. Rochford, D.A. Duncan, D.A. Warr, J. Lawrence, T.-L. Lee, P.K. Thakur, G. Costantini, D.P. Woodruff, Conformational adsorption changes of electron acceptor molecules on metal surfaces, *in preparation.*

P. J. Blowey, R. J. Maurer, L. A. Rochford, D. A. Duncan, D. A. Warr, P. T. P. Ryan, T.-L. Lee, P. K. Thakur, G. Costantini, D. P. Woodruff, The structure of TCNQ/alkali metal charge-transfer networks on metal surfaces, *in preparation.*

P. J. Blowey, R. J. Maurer, L. A. Rochford, D. A. Duncan, J.-H. Kang, D. A. Warr, A. J. Ramadan, T.-L. Lee, P. K. Thakur, G. Costantini, K. Reuter and D. P. Woodruff, The structure of VOPc on Cu(111): does V=O point up, down, or both?*, in preparation.*

Appendix B – Additional polymer molecules deposited via ESD-STM

Figure B. 1 contains an assortment of additional polymer molecules which have been deposited using the Molecular Spray system and a procedure which was outlined in section 3.2.4.
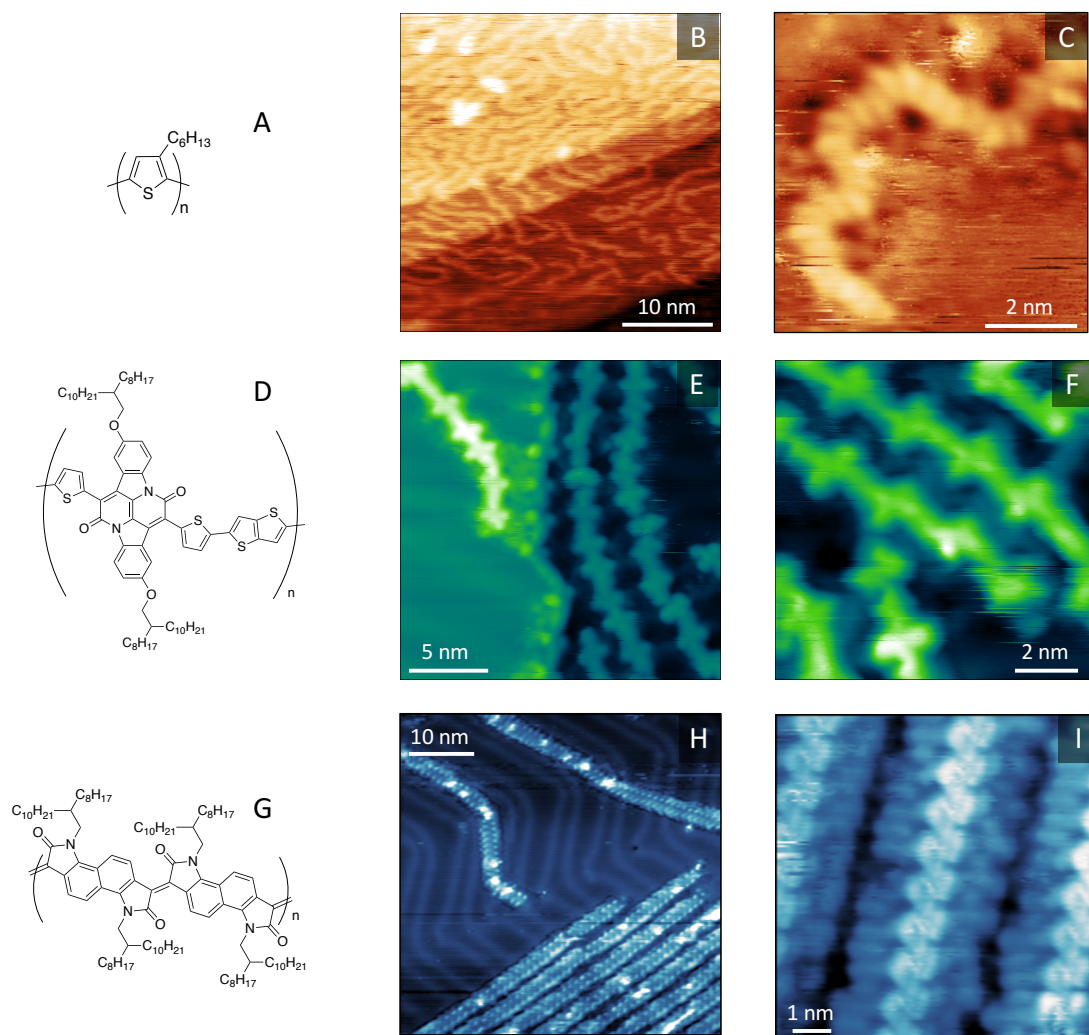
Figure B. 1 Chemical structures and STM images of a series of polymers deposited on Au(111) by ESD-STM. V = -1.5V, I = 200 pA.

These polymers represent a range of molecules which were trialled during this work and our currently being studied further within our group. At the time of writing this thesis insufficient analysis and data had been collected in order to draw any significant conclusions form this work. However, this data is included as it shows that the ESD-STM technique can be used on a number of different conjugated polymers and not only on those already shown in this thesis.

Bibliography

1. Dimitrakopoulos, C. D., Brown, A. R. & Pomp, A. Molecular beam deposited thin films of pentacene for organic field effect transistor applications. *J. Appl. Phys.* **80**, 2501–2508 (1996).

2. Schreiber, F. Organic molecular beam deposition: Growth studies beyond the first monolayer. *Phys. Status Solidi A* **201**, 1037–1054 (2004).

3. Bell, A. T. The Impact of Nanoscience on Heterogeneous Catalysis. *Science* **299**, 1688–1691 (2003).

4. Kippelen, B. & Brédas, J.-L. Organic photovoltaics. *Energy Environ. Sci.* **2**, 251–261 (2009).

5. Guo, X., Baumgarten, M. & Müllen, K. Designing π-conjugated polymers for organic electronics. *Prog. Polym. Sci.* **38**, 1832–1908 (2013).

6. Grill, L. Large molecules on surfaces: deposition and intramolecular STM manipulation by directional forces. *J. Phys. Condens. Matter* **22**, 084023 (2010).

7. Rapenne, G. *et al.* Launching and landing single molecular wheelbarrows on a Cu(1 0 0) surface. *Chem. Phys. Lett.* **431**, 219–222 (2006).

8. Vitali, L. *et al.* Electronic Structure of Surface-supported Bis(phthalocyaninato) terbium(III) Single Molecular Magnets. *Nano Lett.* **8**, 3364–3368 (2008).

9. Mishra, A. & Bäuerle, P. Small Molecule Organic Semiconductors on the Move: Promises for Future Solar Energy Technology. *Angew. Chem. Int. Ed.* **51**, 2020–2067 (2012).

10. Schueppel, R. *et al.* Optimizing organic photovoltaics using tailored heterojunctions: A photoinduced absorption study of oligothiophenes with low band gaps. *Phys. Rev. B* **77**, 085311 (2008).

11. Kudernac, T. *et al.* Electrically driven directional motion of a four-wheeled molecule on a metal surface. *Nature* **479**, 208–211 (2011).

12. Yamashita, M. & Fenn, J. B. Electrospray ion source. Another variation on the free-jet theme. *J. Phys. Chem.* **88**, 4451–4459 (1984).

13. Satterley, C. J. *et al.* Electrospray deposition of fullerenes in ultra-high vacuum: in situ scanning tunneling microscopy and photoemission spectroscopy. *Nanotechnology* **18**, 455304 (2007).

14. Rauschenbach, S. *et al.* Electrospray Ion Beam Deposition of Clusters and Biomolecules. *Small* **2**, 540–547 (2006).

15. Hadjar, O. *et al.* Design and Performance of an Instrument for Soft Landing of Biomolecular Ions on Surfaces. *Anal. Chem.* **79**, 6566–6574 (2007).

16. Hamann, C. *et al.* Ultrahigh vacuum deposition of organic molecules by electrospray ionization. *Rev. Sci. Instrum.* **82**, 033903 (2011).

17. Kondratuk, D. V. *et al.* Vernier-Templated Synthesis, Crystal Structure, and Supramolecular Chemistry of a 12-Porphyrin Nanoring. *Chem. – Eur. J.* **20**, 12826–12834 (2014).

18. Rauschenbach, S. *et al.* Electrospray Ion Beam Deposition: Soft-Landing and Fragmentation of Functional Molecules at Solid Surfaces. *ACS Nano* **3**, 2901–2910 (2009).

19. Gunaratne, K. D. D. *et al.* Design and performance of a high-flux electrospray ionization source for ion soft landing. *Analyst* **140**, 2957–2963 (2015).

20. Hauptmann, N., Hamann, C., Tang, H. & Berndt, R. Soft-Landing Electrospray Deposition of the Ruthenium Dye N3 on Au(111). *J. Phys. Chem. C* **117**, 9734–9738 (2013).

21. Keeler, J. *Understanding NMR Spectroscopy.* (John Wiley & Sons, 2011).

22. Hoffmann, E. de & Stroobant, V. *Mass Spectrometry: Principles and Applications*. (John Wiley & Sons, 2013).

23. Jennings, W., Mittlefehldt, E. & Stremple, P. *Analytical Gas Chromatography*. (Academic Press, 1997).

24. Stuart, B. H. *Infrared Spectroscopy: Fundamentals and Applications*. (John Wiley & Sons, 2004).

25. Ladd, M. & Palmer, R. *Structure Determination by X-ray Crystallography: Analysis by X-rays and Neutrons*. (Springer Science & Business Media, 2014).

26. Hendriks, K. H. *et al.* Homocoupling Defects in Diketopyrrolopyrrole-Based Copolymers and Their Effect on Photovoltaic Performance. *J. Am. Chem. Soc.* **136**, 11128–11133 (2014).

27. Feynman, R. P. There's plenty of room at the bottom. *Eng Sci* **23**, 22–36 (1960).

28. The Nobel Prize in Physics 2017 - Scientific Background: The development of cryo-electron microscopy. *NobelPrize.org* Available at: https://www.nobelprize.org/prizes/chemistry/2017/advanced-information/. (Accessed: 4th September 2018)

29. Oteyza, D. G. de *et al.* Direct Imaging of Covalent Bond Structure in Single-Molecule Chemical Reactions. *Science* 1238187 (2013). doi:10.1126/science.1238187

30. Gross, L., Mohn, F., Moll, N., Liljeroth, P. & Meyer, G. The Chemical Structure of a Molecule Resolved by Atomic Force Microscopy. *Science* **325**, 1110–1114 (2009).

31. Gross, L. *et al.* Bond-Order Discrimination by Atomic Force Microscopy. *Science* **337**, 1326–1329 (2012).

32. Fatayer, S. *et al.* Atomic Force Microscopy Identifying Fuel Pyrolysis Products and Directing the Synthesis of Analytical Standards. *J. Am. Chem. Soc.* **140**, 8156–8161 (2018).

33. Schulz, F. *et al.* Insights into incipient soot formation by atomic force microscopy. *Proc. Combust. Inst.* (2018). doi:10.1016/j.proci.2018.06.100

34. Tsai, H.-Z. *et al.* Molecular Self-Assembly in a Poorly Screened Environment: F$_4$TCNQ on Graphene/BN. *ACS Nano* **9**, 12168–12173 (2015).

35. Riss, A. *et al.* Local Electronic and Chemical Structure of Oligo-acetylene Derivatives Formed Through Radical Cyclizations at a Surface. *Nano Lett.* **14**, 2251–2255 (2014).

36. Riss, A. *et al.* Imaging single-molecule reaction intermediates stabilized by surface dissipation and entropy. *Nat. Chem.* **8**, 678–683 (2016).

37. Rizzo, D. J. *et al.* Topological band engineering of graphene nanoribbons. *Nature* **560**, 204–208 (2018).

38. Jarvis, S. P. *et al.* Simulated structure and imaging of NTCDI on Si(1 1 1)-7 × 7 : a combined STM, NC-AFM and DFT study. *J. Phys. Condens. Matter* **27**, 054004 (2015).

39. Tanaka, H. & Kawai, T. Partial sequencing of a single DNA molecule with a scanning tunnelling microscope. *Nat. Nanotechnol.* **4**, 518–522 (2009).

40. Baker, A. A., Helbert, W., Sugiyama, J. & Miles, M. J. New Insight into Cellulose Structure by Atomic Force Microscopy Shows the Iα Crystal Phase at Near-Atomic Resolution. *Biophys. J.* **79**, 1139–1145 (2000).

41. Scheuring, S., Reiss-Husson, F., Engel, A., Rigaud, J.-L. & Ranck, J.-L. High-resolution AFM topographs of Rubrivivax gelatinosus light-harvesting complex LH2. *EMBO J.* **20**, 3029–3035 (2001).

42. Yang, X. *et al.* On the decoupling of molecules at metal surfaces. *Chem. Commun.* **54**, 9039–9042 (2018).

43. Kowarik, S., Gerlach, A. & Schreiber, F. Organic molecular beam deposition: fundamentals, growth dynamics, and *in situ* studies. *J. Phys. Condens. Matter* **20**, 184005 (2008).

44. Beuhler, R. J., Flanigan, E., Greene, L. J. & Friedman, L. Proton transfer mass spectrometry of peptides. Rapid heating technique for underivatized peptides containing arginine. *J. Am. Chem. Soc.* **96**, 3990–3999 (1974).

45. Zambelli, T. *et al.* Deformation of a 3.7-nm long molecular wire at a metallic step edge. *Phys. Rev. B* **66**, 075410 (2002).

46. Kanno, T., Tanaka, H., Nakamura, T., Tabata, H. & Kawai, T. Real Space Observation of Double-Helix DNA Structure Using a Low Temperature Scanning Tunneling Microscopy. *Jpn. J. Appl. Phys.* **38**, L606 (1999).

47. Kasai, H. *et al.* STM Observation of Single Molecular Chains of π-Conjugated Polymers. *Chem. Lett.* **31**, 696–697 (2002).

48. Terada, Y., Choi, B.-K., Heike, S., Fujimori, M. & Hashizume, T. Placing Conducting Polymers onto a H-Terminated Si(100) Surface via a Pulse Valve. *Nano Lett.* **3**, 527–531 (2003).

49. Swarbrick, J. C., Taylor, J. B. & O'Shea, J. N. Electrospray deposition in vacuum. *Appl. Surf. Sci.* **252**, 5622–5626 (2006).

50. Saywell, A. *et al.* Self-assembled aggregates formed by single-molecule magnets on a gold surface. *Nat. Commun.* **1**, 1–8 (2010).

51. Deng, Z. *et al.* A Close Look at Proteins: Submolecular Resolution of Two- and Three-Dimensionally Folded Cytochrome c at Surfaces. *Nano Lett.* **12**, 2452–2458 (2012).

52. Abb, S., Harnau, L., Gutzler, R., Rauschenbach, S. & Kern, K. Two-dimensional honeycomb network through sequence-controlled self-assembly of oligopeptides. *Nat. Commun.* **7**, 10335 (2016).

53. Rauschenbach, S., Ternes, M., Harnau, L. & Kern, K. Mass Spectrometry as a Preparative Tool for the Surface Science of Large Molecules. *Annu. Rev. Anal. Chem.* **9**, 473–498

54. Karan, S. *et al.* Remotely Triggered Geometrical Isomerization of a Binuclear Complex. *J. Am. Chem. Soc.* **136**, 6163–6166 (2014).

55. Grill, V., Shen, J., Evans, C. & Cooks, R. G. Collisions of ions with surfaces at chemically relevant energies: Instrumentation and phenomena. *Rev. Sci. Instrum.* **72**, 3149 (2001).

56. Dubey, G. *et al.* Chemical Modification of Graphene via Hyperthermal Molecular Reaction. *J. Am. Chem. Soc.* **136**, 13482–13485 (2014).

57. Rayleigh, Lord. On the equilibrium of liquid conducting masses charged with electricity. *Lond. Edinb. Dublin Philos. Mag. J. Sci.* **14**, 184–186 (1882).

58. Zeleny, J. The Electrical Discharge from Liquid Points, and a Hydrostatic Method of Measuring the Electric Intensity at Their Surfaces. *Phys. Rev.* **3**, 69–91 (1914).

59. Zeleny, J. Instability of Electrified Liquid Surfaces. *Phys. Rev.* **10**, 1–6 (1917).

60. Dole, M. *et al.* Molecular Beams of Macroions. *J. Chem. Phys.* **49**, 2240–2249 (1968).

61. Yamashita, M. & Fenn, J. B. Electrospray ion source. Another variation on the free-jet theme. *J. Phys. Chem.* **88**, 4451–4459 (1984).

62. Fenn, J. B., Mann, M., Meng, C. K., Wong, S. F. & Whitehouse, C. M. Electrospray ionization for mass spectrometry of large biomolecules. *Science* **246**, 64–71 (1989).

63. The Nobel Prize in Chemistry 2002. *NobelPrize.org* Available at: https://www.nobelprize.org/prizes/chemistry/2002/summary/. (Accessed: 22nd August 2018)

64. Taylor, G. Disintegration of Water Drops in an Electric Field. *Proc. R. Soc. Math. Phys. Eng. Sci.* **280**, 383–397 (1964).

65. Smith, J. N., Flagan, R. C. & Beauchamp, J. L. Droplet Evaporation and Discharge Dynamics in Electrospray Ionization. *J. Phys. Chem. A* **106**, 9957–9967 (2002).

66. Schmelzeisen-Redeker, G., Bütfering, L. & Röllgen, F. W. Desolvation of ions and molecules in thermospray mass spectrometry. *Int. J. Mass Spectrom. Ion Process.* **90**, 139–150 (1989).

67. Wong, S. S., Giessmann, U., Karas, M. & Röllgen, F. W. Field desorption of sucrose studied by combined optical microscopy and mass spectrometry. *Int. J. Mass Spectrom. Ion Process.* **56**, 139–150 (1984).

68. Iribarne, J. V. On the evaporation of small ions from charged droplets. *J. Chem. Phys.* **64**, 2287 (1976).

69. Thomson, B. A. & Iribarne, J. V. Field induced ion evaporation from liquid surfaces at atmospheric pressure. *J. Chem. Phys.* **71**, 4451–4463 (1979).

70. Fernandez de la Mora, J. Electrospray ionization of large multiply charged species proceeds via Dole's charged residue mechanism. *Anal. Chim. Acta* **406**, 93–104 (2000).

71. Gamero-Castaño, M. & Fernández de la Mora, J. Direct measurement of ion evaporation kinetics from electrified liquid surfaces. *J. Chem. Phys.* **113**, 815–832 (2000).

72. Nguyen, S. & Fenn, J. B. Gas-phase ions of solute species from charged droplets of solutions. *Proc. Natl. Acad. Sci.* **104**, 1111–1117 (2007).

73. Burgoyne, T. W. & Hieftje, G. M. An introduction to ion optics for the mass spectrograph. *Mass Spectrom. Rev.* **15**, 241–259 (1996).

74. Drummond, I. The ion optics of low-energy ion beams. *Vacuum* **34**, 51–61 (1984).

75. Adams, A. & Read, F. H. Electrostatic cylinder lenses II: Three element einzel lenses. *J. Phys. [E]* **5**, 150–155 (1972).

76. Heddle, D. W. O. *Electrostatic Lens Systems, 2nd edition*. (CRC Press, 2000).

77. Gerlich, D. Inhomogeneous RF Fields: A Versatile Tool for the Study of Processes with Slow Ions. in *Advances in Chemical Physics* (eds. Ng, C.-Y., Baer, M., Prigogine, I. & Rice, S. A.) **82**, 1–176 (John Wiley & Sons, Inc., 1992).

78. Dahl, D. A. simion for the personal computer in reflection. *Int. J. Mass Spectrom.* **200**, 3–25 (2000).

79. Dawson, P. H. *Quadrupole Mass Spectrometry and Its Applications*. (Elsevier, 2013).

80. El-Aneed, A., Cohen, A. & Banoub, J. Mass Spectrometry, Review of the Basics: Electrospray, MALDI, and Commonly Used Mass Analyzers. *Appl. Spectrosc. Rev.* **44**, 210–230 (2009).

81. March, R. E. An Introduction to Quadrupole Ion Trap Mass Spectrometry. *J. Mass Spectrom.* **32**, 351–369 (1997).

82. Binnig, G., Rohrer, H., Gerber, C. & Weibel, E. Surface Studies by Scanning Tunneling Microscopy. *Phys. Rev. Lett.* **49**, 57–61 (1982).

83. Binnig, G., Rohrer, H., Gerber, C. & Weibel, E. Tunneling through a controllable vacuum gap. *Appl. Phys. Lett.* **40**, 178–180 (1982).

84. Bonnell, D. *Scanning Probe Microscopy and Spectroscopy: Theory, Techniques, and Applications*. (Wiley, 2000).

85. Bai, C. *Scanning Tunneling Microscopy and Its Application*. (Springer Science & Business Media, 2000).

86. Tersoff, J. & Hamann, D. R. Theory and Application for the Scanning Tunneling Microscope. *Phys. Rev. Lett.* **50**, 1998–2001 (1983).

87. Magonov, S. N. Surface Characterization of Materials at Ambient Conditions by Scanning Tunneling Microscopy (STM) and Atomic Force Microscopy (AFM). *Appl. Spectrosc. Rev.* **28**, 1–121 (1993).

88. Mozetič, M. *et al.* Recent advances in vacuum sciences and applications. *J. Phys. Appl. Phys.* **47**, 153001 (2014).

89. Chambers, A. *Modern Vacuum Physics*. (Taylor & Francis, 2004).

90. O'Hanlon, J. F. *A User's Guide to Vacuum Technology*. (John Wiley & Sons, 2005).

91. Cheng, Y.-J., Yang, S.-H. & Hsu, C.-S. Synthesis of Conjugated Polymers for Organic Solar Cell Applications. *Chem. Rev.* **109**, 5868–5923 (2009).

92. Burroughes, J. H. *et al.* Light-emitting diodes based on conjugated polymers. *Nature* **347**, 539–541 (1990).

93. Greczmiel, M. *et al.* Polymer light emitting diodes. *Macromol. Symp.* **102**, 371–380 (1996).

94. Horowitz, G. Organic Field-Effect Transistors. *Adv. Mater.* **10**, 365–377 (1998).

95. Stutzmann, N., Friend, R. H. & Sirringhaus, H. Self-Aligned, Vertical-Channel, Polymer Field-Effect Transistors. *Science* **299**, 1881–1884 (2003).

96. Gregg, B. A. & Hanna, M. C. Comparing organic to inorganic photovoltaic cells: Theory, experiment, and simulation. *J. Appl. Phys.* **93**, 3605–3614 (2003).

97. McCullough, R. D., Lowe, R. D., Jayaraman, M. & Anderson, D. L. Design, synthesis, and control of conducting polymer architectures: structurally homogeneous poly(3-alkylthiophenes). *J. Org. Chem.* **58**, 904–912 (1993).

98. Bao, Z., Chan, W. & Yu, L. Synthesis of conjugated polymer by the Stille Coupling Reaction. *Chem. Mater.* **5**, 2–3 (1993).

99. Bao, Z., Chan, W. K. & Yu, L. Exploration of the Stille Coupling Reaction for the Synthesis of Functional Polymers. *J. Am. Chem. Soc.* **117**, 12426–12435 (1995).

100. Nielsen, C. B., Turbiez, M. & McCulloch, I. Recent Advances in the Development of Semiconducting DPP-Containing Polymers for Transistor Applications. *Adv. Mater.* **25**, 1859–1880 (2013).

101. Zhang, S. *et al.* Enhanced Photovoltaic Performance of Diketopyrrolopyrrole (DPP)-Based Polymers with Extended π Conjugation. *J. Phys. Chem. C* **117**, 9550–9557 (2013).

102. Stille, J. K. The Palladium-Catalyzed Cross-Coupling Reactions of Organotin Reagents with Organic Electrophiles[New Synthetic Methods(58)]. *Angew. Chem. Int. Ed. Engl.* **25**, 508–524 (1986).

103. Miyaura, N. & Suzuki, A. Palladium-Catalyzed Cross-Coupling Reactions of Organoboron Compounds. *Chem. Rev.* **95**, 2457–2483 (1995).

104. Sonogashira, K. Development of Pd–Cu catalyzed cross-coupling of terminal acetylenes with sp2-carbon halides. *J. Organomet. Chem.* **653**, 46–49 (2002).

105. Li, W., Hendriks, K. H., Wienk, M. M. & Janssen, R. A. J. Diketopyrrolopyrrole Polymers for Organic Solar Cells. *Acc. Chem. Res.* **49**, 78–85 (2016).

106. Sirringhaus, H. *et al.* Two-dimensional charge transport in self-organized, high-mobility conjugated polymers. *Nature* **401**, 685–688 (1999).

107. Kiess, H. *Conjugated Conducting Polymers*. (Springer Science & Business Media, 2012).

108. Kreyenschmidt, M., Uckert, F. & Muellen, K. A new soluble poly (p-phenylene) with tetrahydropyrene repeating units. *Macromolecules* **28**, 4577–4582 (1995).

109. Bauer, N. *et al.* Comparing non-fullerene acceptors with fullerene in polymer solar cells: a case study with FTAZ and PyCNTAZ. *J. Mater. Chem. A* **5**, 4886–4893 (2017).

110. Gebeyehu, D., Maennig, B., Drechsel, J., Leo, K. & Pfeiffer, M. Bulk-heterojunction photovoltaic devices based on donor–acceptor organic small molecule blends. *Sol. Energy Mater. Sol. Cells* **79**, 81–92 (2003).

111. Müllen, K. & Pisula, W. Donor–Acceptor Polymers. *J. Am. Chem. Soc.* **137**, 9503–9505 (2015).

112. Haq, S. *et al.* Racemic versus Enantiopure Alanine on Cu(110): An Experimental Study. *Langmuir* **23**, 10694–10700 (2007).

113. Lingenfelder, M. *et al.* Tracking the Chiral Recognition of Adsorbed Dipeptides at the Single-Molecule Level. *Angew. Chem. Int. Ed.* **46**, 4492–4495 (2007).

114. Pittman, J. L. & O'Connor, P. B. A minimum thickness gate valve with integrated ion optics for mass spectrometry. *J. Am. Soc. Mass Spectrom.* **16**, 441–445 (2005).

115. Pauly, M. *et al.* A hydrodynamically optimized nano-electrospray ionization source and vacuum interface. *Analyst* **139**, 1856–1867 (2014).

116. Bernier, L., Pinfold, H., Pauly, M., Rauschenbach, S. & Reiss, J. Gas Flow and Ion Transfer in Heated ESI Capillary Interfaces. *J. Am. Soc. Mass Spectrom.* **29**, 761–773 (2018).

117. Kelly, R. T., Tolmachev, A. V., Page, J. S., Tang, K. & Smith, R. D. The ion funnel: Theory, implementations, and applications. *Mass Spectrom. Rev.* **29**, 294–312 (2010).

118. Kelly, R. T., Tolmachev, A. V., Page, J. S., Tang, K. & Smith, R. D. The ion funnel: Theory, implementations, and applications. *Mass Spectrom. Rev.* **29**, 294–312

119. Badu-Tawiah, A. K., Wu, C. & Cooks, R. G. Ambient Ion Soft Landing. *Anal. Chem.* **83**, 2648–2654 (2011).

120. Satterley, C. J. *et al.* Electrospray deposition of fullerenes in ultra-high vacuum: *in situ* scanning tunneling microscopy and photoemission spectroscopy. *Nanotechnology* **18**, 455304 (2007).

121. Gibson, A. J. *et al.* Charge transfer from an adsorbed ruthenium-based photosensitizer through an ultra-thin aluminium oxide layer and into a metallic substrate. *J. Chem. Phys.* **140**, 234708 (2014).

122. Saywell, A. *et al.* Electrospray Deposition of C $_{60}$ on a Hydrogen-Bonded Supramolecular Network. *J. Phys. Chem. C* **112**, 7706–7709 (2008).

123. Warr, D. A. *et al.* Sequencing conjugated polymers by eye. *Sci. Adv.* **4**, eaas9543 (2018).

124. Temperton, R. H. Complex molecules on surfaces: In-situ electrospray deposition and photoelectron spectroscopy. (University of Nottingham, 2017).

125. Temperton, R. H., O'Shea, J. N. & Scurr, D. J. On the suitability of high vacuum electrospray deposition for the fabrication of molecular electronic devices. *Chem. Phys. Lett.* **682**, 15–19 (2017).

126. Scudiero, L., Barlow, D. E. & Hipps, K. W. Scanning Tunneling Microscopy, Orbital-Mediated Tunneling Spectroscopy, and Ultraviolet Photoelectron

Spectroscopy of Nickel(II) Octaethylporphyrin Deposited from Vapor. *J. Phys. Chem. B* **106**, 996–1003 (2002).

127. Ogunrinde, A., Hipps, K. W. & Scudiero, L. A Scanning Tunneling Microscopy Study of Self-Assembled Nickel(II) Octaethylporphyrin Deposited from Solutions on HOPG. *Langmuir* **22**, 5697–5701 (2006).

128. Nandi, G., Chilukuri, B., Hipps, K. W. & Mazur, U. Surface directed reversible imidazole ligation to nickel(II) octaethylporphyrin at the solution/solid interface: a single molecule level study. *Phys. Chem. Chem. Phys.* **18**, 20819–20829 (2016).

129. Rauschenbach, S. *et al.* Electrospray ion beam deposition: Soft-landing and fragmentation of functional molecules at solid surfaces. *ACS Nano* **3**, 2901–2910 (2009).

130. Volný, M., Elam, W. T., Branca, A., Ratner, B. D. & Tureček, F. Preparative Soft and Reactive Landing of Multiply Charged Protein Ions on a Plasma-Treated Metal Surface. *Anal. Chem.* **77**, 4890–4896 (2005).

131. Zhang, X. *et al.* Molecular origin of high field-effect mobility in an indacenodithiophene–benzothiadiazole copolymer. *Nat. Commun.* **4**, 2238 (2013).

132. Venkateshvaran, D. *et al.* Approaching disorder-free transport in high-mobility conjugated polymers. *Nature* **515**, 384–388 (2014).

133. Vezie, M. S. *et al.* Exploring the origin of high optical absorption in conjugated polymers. *Nat. Mater.* **15**, 746–753 (2016).

134. McCulloch, I. *et al.* Liquid-crystalline semiconducting polymers with high charge-carrier mobility. *Nat Mater* **5**, 328–333 (2006).

135. Noriega, R. *et al.* A general relationship between disorder, aggregation and charge transport in conjugated polymers. *Nat. Mater.* **12**, 1038–1044 (2013).

136. Kim, Y. *et al.* A strong regioregularity effect in self-organizing conjugated polymer films and high-efficiency polythiophene: Fullerene solar cells. *Nat Mater* **5**, 197–203 (2006).

137. Ying, L., Huang, F. & Bazan, G. C. Regioregular narrow-bandgap-conjugated polymers for plastic electronics. *Nat Commun* **8**, (2017).

138. Hu, D. *et al.* Collapse of stiff conjugated polymers with chemical defects into ordered, cylindrical conformations. *Nature* **405**, 1030–1033 (2000).

139. Hong, W. *et al.* Is a polymer semiconductor having a "perfect" regular structure desirable for organic thin film transistors? *Chem Sci* **6**, 3225–3235 (2015).

140. Xu, L., Yang, L. & Lei, S. Self-assembly of conjugated oligomers and polymers at the interface: structure and properties. *Nanoscale* **4**, 4399 (2012).

141. Gesquière, A. *et al.* Direct observation of chiral oligo(p-phenylenevinylene)s with scanning tunneling microscopy. *J. Mater. Chem.* **13**, 2164–2167 (2003).

142. Räder, H. J. *et al.* Processing of giant graphene molecules by soft-landing mass spectrometry. *Nat. Mater.* **5**, 276–280 (2006).

143. O'Sullivan, M. C. *et al.* Vernier templating and synthesis of a 12-porphyrin nano-ring. *Nature* **469**, 72–75 (2011).

144. Jethwa, S. J. *et al.* Revealing the structural detail of individual polymers using a combination of electrospray deposition and UHV-STM. *Chem Commun* **53**, 1168–1171 (2017).

145. Yokoyama, T., Kogure, Y., Kawasaki, M., Tanaka, S. & Aoshima, K. Scanning Tunneling Microscopy Imaging of Long Oligothiophene Wires Deposited on

Au(111) Using Electrospray Ionization. *J. Phys. Chem. C* **117**, 18484–18487 (2013).

146. Förster, S. & Widdra, W. Structure of single polythiophene molecules on Au(001) prepared by in situ UHV electrospray deposition. *J. Chem. Phys.* **141**, 054713 (2014).

147. Qu, S. & Tian, H. Diketopyrrolopyrrole (DPP)-based materials for organic photovoltaics. *Chem. Commun.* **48**, 3039–3051 (2012).

148. Fu, C., Bélanger-Gariépy, F. & Perepichka, D. F. Supramolecular ordering of difuryldiketopyrrolopyrrole: The effect of alkyl chains and inter-ring twisting. *CrstEngComm* **18**, 4285–4289 (2016).

149. Hayashi, S., Yamamoto, S. –. & Koizumi, T. Effects of molecular weight on the optical and electrochemical properties of EDOT-based p-conjugated polymers. *Sci Rep 7* **1078**, (2017).

150. Bijleveld, J. C. *et al.* Efficient solar cells based on an easily accessible diketopyrrolopyrrole polymer. *Adv Mater* **22**, 242–246 (2010).

151. Mohamed, S. & Charles, L. Selectivity of electrospray response in small polymer analysis by mass spectrometry. *Rapid Commun. Mass Spectrom.* **20**, 3188–3192 (2006).

152. Ouahabi, A. A., Amalian, J.-A., Charles, L. & Lutz, J.-F. Mass spectrometry sequencing of long digital polymers facilitated by programmed inter-byte fragmentation. *Nat. Commun.* **8**, 967 (2017).

153. Roy, R. K. *et al.* Design and synthesis of digitally encoded polymers that can be decoded and erased. *Nat. Commun.* **6**, 7237 (2015).

154. Goursot, A., Mineva, T., Kevorkyants, R. & Talbi, D. Interaction between *n* - Alkane Chains: Applicability of the Empirically Corrected Density Functional

Theory for Van der Waals Complexes [†]. *J. Chem. Theory Comput.* **3**, 755–763 (2007).

155. Baniya, S., Khanal, D., Lafalce, E., You, W. & Vardeny, Z. V. Optical studies of native defects in p-conjugated donor–acceptor copolymers. *J Appl Phys* **123**, 161571 (2018).

156. Zhang, W., Milner, S. T. & Gomez, E. D. Nematic order imposes molecular weight effect on charge transport in conjugated polymers. *ACS Cent Sci* **4**, 413–421 (2018).

157. Lee, J., Kalin, A. J., Yuan, T., Al-Hashimi, M. & Fang, L. Fully conjugated ladder polymers. *Chem Sci* **8**, 2503–2521 (2017).

158. Nicolai, H. T. *et al.* Unification of trap-limited electron transport in semiconducting polymers. *Nat. Mater.* **11**, 882–887 (2012).

159. Bura, T., Blaskovits, J. T. & Leclerc, M. Direct (hetero)arylation polymerization: Trends and perspectives. *J Am Chem Soc* **138**, 10056–10071 (2016).

160. Direct heteroarylation polymerization: Guidelines for defect-free conjugated polymers. *Chem Sci* **8**, 3913–3925 (2017).

161. Hinaut, A., Pawlak, R., Meyer, E. & Glatzel, T. Electrospray deposition of organic molecules on bulk insulator surfaces. *Beilstein J. Nanotechnol.* **6**, 1927–1934 (2015).

162. Hinaut, A. *et al.* Electrospray deposition of structurally complex molecules revealed by atomic force microscopy. *Nanoscale* **10**, 1337–1344 (2018).

163. Robitaille, A., Jenekhe, S. A. & Leclerc, M. Poly(naphthalene diimide-alt-bithiophene) Prepared by Direct (Hetero)arylation Polymerization for Efficient All-Polymer Solar Cells. *Chem. Mater.* (2018). doi:10.1021/acs.chemmater.8b02160

164. Mehmood, U., Al-Ahmed, A. & Hussein, I. A. Review on recent advances in polythiophene based photovoltaic devices. *Renew. Sustain. Energy Rev.* **57**, 550–561 (2016).

165. McCullough, R. D. & Lowe, R. D. Enhanced electrical conductivity in regioselectively synthesized poly(3-alkylthiophenes). *J. Chem. Soc. Chem. Commun.* 70 (1992). doi:10.1039/c39920000070

166. Kaloni, T. P., Giesbrecht, P. K., Schreckenbach, G. & Freund, M. S. Polythiophene: From Fundamental Perspectives to Applications. *Chem. Mater.* **29**, 10248–10283 (2017).

167. Fallon, K. J. *et al.* A Nature-Inspired Conjugated Polymer for High Performance Transistors and Solar Cells. *Macromolecules* **48**, 5148–5154 (2015).

168. Scharber, M. C. *et al.* Design Rules for Donors in Bulk-Heterojunction Solar Cells—Towards 10 % Energy-Conversion Efficiency. *Adv. Mater.* **18**, 789–794

169. Yu, G. & Heeger, A. J. Charge separation and photovoltaic conversion in polymer composites with internal donor/acceptor heterojunctions. *J. Appl. Phys.* **78**, 4510–4515 (1995).

170. Yu, G., Gao, J., Hummelen, J. C., Wudl, F. & Heeger, A. J. Polymer Photovoltaic Cells: Enhanced Efficiencies via a Network of Internal Donor-Acceptor Heterojunctions. *Science* **270**, 1789–1791 (1995).

171. Fineman, M. & Ross, S. D. Linear method for determining monomer reactivity ratios in copolymerization. *J. Polym. Sci.* **5**, 259–262 (1950).

172. Chong,) Y. K., Le, T. P. T., Moad, G., Rizzardo, E. & Thang, S. H. A More Versatile Route to Block Copolymers and Other Polymers of Complex Architecture by Living Radical Polymerization: The RAFT Process. *Macromolecules* **32**, 2071–2074 (1999).

173. Faraggi, M. N. *et al.* Bonding and Charge Transfer in Metal–Organic Coordination Networks on Au(111) with Strong Acceptor Molecules. *J. Phys. Chem. C* **116**, 24558–24565 (2012).

174. Kutsenko, V. Y. *et al.* Alkylthiol self-assembled monolayers on Au(111) with tailored tail groups for attaching gold nanoparticles. *Nanotechnology* **28**, 235603 (2017).

175. Tahara, K. *et al.* Two-Dimensional Porous Molecular Networks of Dehydrobenzo[12]annulene Derivatives via Alkyl Chain Interdigitation. *J. Am. Chem. Soc.* **128**, 16613–16625 (2006).

176. Tahara, K., Lei, S., Adisoejoso, J., Feyter, S. D. & Tobe, Y. Supramolecular surface-confined architectures created by self-assembly of triangular phenylene–ethynylene macrocycles via van der Waals interaction. *Chem. Commun.* **46**, 8507–8525 (2010).

177. Tahara, K. *et al.* Control and induction of surface-confined homochiral porous molecular networks. *Nat. Chem.* **3**, 714–719 (2011).

178. Zhou, C. *et al.* Chain Length Dependence of the Photovoltaic Properties of Monodisperse Donor–Acceptor Oligomers as Model Compounds of Polydisperse Low Band Gap Polymers. *Adv. Funct. Mater.* **24**, 7538–7547

179. Yiu, A. T. *et al.* Side-chain tunability of furan-containing low-band-gap polymers provides control of structural order in efficient solar cells. *J Am Chem Soc* **134**, 2180–2185 (2012).

180. Zhang, X. *et al.* Molecular Packing of High-Mobility Diketo Pyrrolo-Pyrrole Polymer Semiconductors with Branched Alkyl Side Chains. *J. Am. Chem. Soc.* **133**, 15073–15084 (2011).

181. Do, K., Huang, D. M., Faller, R. & Moulé, A. J. A comparative MD study of the local structure of polymer semiconductors P3HT and PBTTT. *Phys. Chem. Chem. Phys.* **12**, 14735–14739 (2010).

182. Chabinyc, M. L., Toney, M. F., Kline, R. J., McCulloch, I. & Heeney, M. X-ray Scattering Study of Thin Films of Poly(2,5-bis(3-alkylthiophen-2-yl)thieno[3,2-b]thiophene). *J. Am. Chem. Soc.* **129**, 3226–3237 (2007).

183. Mei, J. & Bao, Z. Side Chain Engineering in Solution-Processable Conjugated Polymers. *Chem. Mater.* **26**, 604–615 (2014).

184. Kang, I., Yun, H.-J., Chung, D. S., Kwon, S.-K. & Kim, Y.-H. Record High Hole Mobility in Polymer Semiconductors via Side-Chain Engineering. *J. Am. Chem. Soc.* **135**, 14896–14899 (2013).

185. Lee, J. *et al.* Boosting the Ambipolar Performance of Solution-Processable Polymer Semiconductors via Hybrid Side-Chain Engineering. *J. Am. Chem. Soc.* **135**, 9540–9547 (2013).

186. Kline, R. J. *et al.* Critical Role of Side-Chain Attachment Density on the Order and Device Performance of Polythiophenes. *Macromolecules* **40**, 7960–7965 (2007).

187. Kline, R. J. *et al.* Critical Role of Side-Chain Attachment Density on the Order and Device Performance of Polythiophenes. *Macromolecules* **40**, 7960–7965 (2007).

188. Miller, N. C. *et al.* Use of X-Ray Diffraction, Molecular Simulations, and Spectroscopy to Determine the Molecular Packing in a Polymer-Fullerene Bimolecular Crystal. *Adv. Mater.* **24**, 6071–6079 (2012).

189. Leventis, A. *et al.* Highly Luminescent Encapsulated Narrow Bandgap Polymers Based on Diketopyrrolopyrrole. *J. Am. Chem. Soc.* **140**, 1622–1626 (2018).